

Applied Millimeter Wave Radar Vibrometry

by

Jessica Centers

Department of Electrical and Computer Engineering  
Duke University

Date: \_\_\_\_\_  
Approved:

---

Jeffrey Krolik, Supervisor

---

Loren Nolte

---

Robert Calderbank

---

Stacy Tantum

---

Donald Bliss

Dissertation submitted in partial fulfillment of  
the requirements for the degree of Doctor of Philosophy in the Department of  
Electrical and Computer Engineering in the Graduate School  
of Duke University

2023

ABSTRACT

Applied Millimeter Wave Radar Vibrometry

by

Jessica Centers

Department of Electrical and Computer Engineering  
Duke University

Date: \_\_\_\_\_

Approved:

---

Jeffrey Krolik, Supervisor

---

Loren Nolte

---

Robert Calderbank

---

Stacy Tantum

---

Donald Bliss

An abstract of a dissertation submitted in partial  
fulfillment of the requirements for the degree  
of Doctor of Philosophy in the Department of  
Electrical and Computer Engineering in the Graduate School  
of Duke University

2023

Copyright © 2023 by Jessica Centers  
All rights reserved except the rights granted by the  
Creative Commons Attribution-Noncommercial License

# Abstract

In this dissertation, novel uses of millimeter-wave (mmW) radars are conceived of and analyzed. While automotive mmW radars have been ubiquitous in advanced driver assistance systems (ADAS), their ability to sense motions at sub-millimeter scale allows them to also find application in systems that require accurate measurements of surface vibrations. While laser Doppler vibrometers (LDVs) are routinely used to measure such vibrations, the lower size, weight, power, and cost (SWAPc) of mmW radars make vibrometry now viable for a variety of new applications. In this work, we consider two such applications: everything-to-vehicle (X2V) wireless communications and non-acoustic human speech analysis.

Within this dissertation, a wireless communication system that uses the radar as a vibrometer is introduced. This system, termed vibrational radar backscatter communications (VRBC), receives messages by observing phase modulations on the radar signal that are caused by vibrations on the surface of a transponder over time. It is shown that this form of wireless communication provides the ability to simultaneously detect, isolate, and decode messages from multiple sources thanks to the spatial resolution of the radar. Additionally, VRBC requires no RF emission on the end of the transponder. Since automotive radars and the conventional X2V solutions are often at odds for spectrum allocations, this characteristic of VRBC is incredibly valuable.

Using an off-the-shelf, resonant transponder, a real VRBC data collection is pre-

sented and used to demonstrate the signal processing techniques necessary to decode a VRBC message. This real data collection proves to achieve a data rate just under 100 bps at approximately 5 meters distance. Rates of this scale can provide warning messages or concise situational awareness information in applications such as X2V, but higher rates are naturally more desirable. For that reason, this dissertation includes discussion on how to design a more optimal VRBC system via transponder design, messaging scheme choice, and using any afforded flexibility in radar parameter choice.

Through the use of an analytical upper bound on VRBC rate and simulation results, we see that rates closer to 1 kbps should be achievable for a transponder approximately the size of a license plate at ranges under 200 meters. The added benefits of requiring no RF spectrum or network scheduling protocols uniquely positions VRBC as a desirable solution in spaces like X2V over commonly considered, potentially higher rate solutions such as direct short range communications (DSRC).

Upon implementing a VRBC system, a handful of complications were encountered. This document designates a full chapter to solving these cases. This includes properly modeling intersymbol interference caused by resonant surfaces and utilizing sequence detection methods rather than single symbol maximum likelihood methods to improve detection in these cases. Additionally, an analysis on what an ideal clutter filter should look like and how it can begin to be achieved is presented. Lastly, a method for mitigating platform vibrational noise at both the radar and the transponder are presented. Using these methods, message detection errors are better avoided, though more optimal system design fundamentally proves the most favorable method for achieving better rates.

Towards non-acoustic human speech analysis, it is shown in this dissertation that the vibrations of a person's throat during speech generation can be accurately captured using a mmW radar. These measurements prove to be similar to those

achieved by the more expensive vibrometry alternative of an LDV with less than 10 dB of SNR depreciation at the first two speech harmonics in the signal's spectrogram. Furthermore, we find that mmW radar vibrometry data resembles a low-pass filtered version of its corresponding acoustic data. We show that this type of data achieves 53% performance in a speaker identification system as opposed to 11% in a speech recognition system. This performance suggests potential for a mmW radar vibrometry in context-blind speaker identification if the performance of the speaker identification system can be further improved without causing the context of the speech to become more recognizable.

In this dissertation, mmW radar vibrational returns are modelled and signal processing chains are provided to allow for these vibrations to be estimated and used in application. In many cases, the work outlined could be used in other areas of mmW radar vibrometry even though it was originally motivated by potentially unrelated applications. It is the hope of this dissertation that the provided models, signal processing methods, visualizations, analytical bound, and results not only justify mmW radar in human speech analysis and backscatter communications, but that they also contribute to the community's understanding of how certain vibrational movements can be best observed, processed, and made useful more broadly.

# Dedication

This dissertation is dedicated to my best friend and husband, Aaron.

# Contents

<b>Abstract</b>	<b>iv</b>
<b>List of Tables</b>	<b>xi</b>
<b>List of Figures</b>	<b>xii</b>
<b>Acknowledgements</b>	<b>xv</b>
<b>1 Introduction</b>	<b>1</b>
1.1 Dissertation Impact . . . . .	4
1.2 Technical Contributions . . . . .	9
<b>2 Background</b>	<b>12</b>
2.1 Frequency Modulated Continuous Waves (FMCW) . . . . .	13
2.2 Properties of Millimeter Wave Backscatter . . . . .	19
<b>3 Millimeter Wave Vibrometry for Human Speech Applications</b>	<b>23</b>
3.1 Motivation of Vibrometry for Human Speech Applications . . . . .	23
3.2 Physiology of Human Speech Generation . . . . .	25
3.3 System Setup . . . . .	27
3.4 TIMIT Database . . . . .	28
3.5 Processing Chain for mmW Radar Vibrometry Speech Visualization .	29
3.6 Speaker Identification . . . . .	33
3.7 Speech Recognition . . . . .	36

<b>4 Vibrational Radar Backscatter Communication (VRBC) Systems</b>	<b>41</b>
4.1 Motivation for VRBC . . . . .	41
4.2 Description of VRBC Data Acquisition . . . . .	44
4.3 VRBC Signal Model . . . . .	47
4.4 VRBC Processing Chain Details . . . . .	50
4.4.1 Target Detection . . . . .	50
4.4.2 Target Isolation . . . . .	54
4.4.3 Clutter Filtering . . . . .	58
4.4.4 Synchronization . . . . .	61
4.4.5 Transponder Impulse Response Estimation . . . . .	67
4.4.6 Message Detection . . . . .	70
<b>5 A VRBC Bound and Discussion of System Design Choices</b>	<b>76</b>
5.1 An Upper Bound on VRBC Rate . . . . .	76
5.2 VRBC System Trade-offs and Considerations . . . . .	81
5.2.1 Radar Parameter Choices . . . . .	82
5.2.2 Transponder Design Choices . . . . .	84
5.2.3 Messaging Scheme Choices . . . . .	87
<b>6 Application-Motivated Methods for VRBC</b>	<b>91</b>
6.1 VRBC Using Resonant Transponding Surfaces . . . . .	91
6.1.1 Considering Varying Levels of Transponder Resonance . . . . .	102
6.1.2 Considering Various Communication Message Constraints . . . . .	104
6.2 Towards Ideal Clutter Filtering . . . . .	106
6.3 Vibrational Noise Mitigation . . . . .	114
6.3.1 Vehicle Vibrational Noise Characterization . . . . .	115
6.3.2 Mitigation of Radar Platform Vibrations . . . . .	118

6.3.3 Mitigation of Target Vibrational Noise . . . . .	120
<b>7 Conclusion</b>	<b>125</b>
7.1 Future Work . . . . .	126
<b>Bibliography</b>	<b>128</b>
<b>Biography</b>	<b>136</b>

# List of Tables

1	Summary Key Variables . . . . .	xvii
3.1	Speaker ID and ASR Performance Across Data Types . . . . .	39
4.1	Square Foot Aluminum Plate Resonant Frequencies . . . . .	46
4.2	Confusion Matrix for Single Symbol ML on the Real Data Collection	75
6.1	States for $M = 3$ and $\mathcal{N} = \{2, 1, 1\}$ . . . . .	97
6.2	Confusion Matrix for Viterbi Sequence Detection on the Real Data Collection . . . . .	101

# List of Figures

2.1	Plot of atmospheric attenuation vs operating frequency at sea level for multiple temperatures. . . . .	21
2.2	Plot of attenuation vs operating frequency due to rainfall at various rates. . . . .	22
3.1	Diagram of human speech generation anatomy. . . . .	26
3.2	Experimental setup with a human speech source. . . . .	27
3.3	Experimental setup with a loudspeaker speech source. . . . .	28
3.4	Statistical graphics and table of TIMIT database characteristics. . . .	29
3.5	Processing chain for generating mmW radar vibrometry spectrograms. . . . .	29
3.6	Plots of the 0 – 2 <sup>th</sup> order Bessel functions of the first kind. . . . .	31
3.7	Adaptive line enhancer noise suppression processing chain. . . . .	31
3.8	Comparison of microphone, LDV, and mmW radar vibrometry spectrograms for a female speaker. . . . .	33
3.9	Network architecture for the speaker identification CNN classifier. . . .	34
3.10	Speaker ID performance for various LPF Cutoff Frequencies for a 20 speaker set. . . . .	36
3.11	Low-pass filtered speaker ID and ASR performance for various LPF Cutoff Frequencies for a 20 speaker set. . . . .	37
3.12	High-pass filtered speaker ID and ASR performance for various HPF Cutoff Frequencies for a 20 speaker set. . . . .	38
4.1	An X2V scenario demonstrating the simultaneous multichannel signal reception of VRBC to the mmW radar-equipped left-most vehicle. . . .	43

4.2	VRBC setup looking from the mmW radar to the transponder. . . . .	45
4.3	Even mode vibrational depictions of a square plate . . . . .	46
4.4	LDV measured maximum displacements at the center and corner of the square foot aluminum transponder versus excitation frequency. . . . .	47
4.5	The processing chain used to get the message signal in a VRBC system. . . . .	51
4.6	The range angle intensity plot for a VRBC example for a time frame prior to VRBC transmission versus during. . . . .	53
4.7	The spectra of a simulated VRBC beam return with two transponders at separate ranges. . . . .	55
4.8	The spectra of VRBC return for a square foot aluminum transponder when transmitting a sequence of tonal symbols. . . . .	56
4.9	Probabilities of error when range-Doppler and direct de-chirped band-pass range processing are used. . . . .	57
4.10	Tonal vibrational power allocation versus the tone's displacement amplitude assuming a 77 GHz operating frequency. . . . .	60
4.11	Range-Doppler intensity plots throughout target isolation and clutter filtering. . . . .	62
4.12	Estimated phase signal for VRBC transmission. . . . .	64
4.13	Magnitude squared coherence over time with a known 1.5 second long chirp whose instantaneous frequency swept from 0 Hz to PRF/2. . . . .	65
4.14	Slices of the sliding window MSC plot at frequencies of interest. . . . .	66
4.15	Auto spectral density for a chirp preamble. . . . .	67
4.16	An STFT of the preamble phase signal. . . . .	68
4.17	Impulse response and frequency response estimate of the square foot aluminum plate transponder . . . . .	69
4.18	Comparison between the observed phase signal and estimated phase signal. . . . .	70
4.19	Symbol excitations and displacements for the real data collection. . . . .	72
5.1	Millimeter-wave spectrum allocation in the U.S. as dictated by the FCC. . . . .	82
5.2	Illustration of FMCW waveform and its parameters. . . . .	83

5.3	Simulated comparison of the symbol classification error for two different vibrational symbol sets. . . . .	89
6.1	The four single-symbol displacements and the multiple symbol interval displacements resulting from sequences of these symbols. . . . .	94
6.2	The detection results for the real data collection of the square foot aluminum transponder. . . . .	101
6.3	The displacements used to compare the detection methods between two levels of resonance. . . . .	102
6.4	Upper bound and simulated communication rates for the more resonant transponder (solid) and less resonant (dashed). . . . .	103
6.5	Upper bound and simulated communication rates for the less resonant transponder for different coding constraints. . . . .	105
6.6	Phasor diagrams in consideration for clutter filtering. . . . .	107
6.7	Vibrometry data of a 200 Hz vibrational displacement before and after adaptive clutter filtering. . . . .	109
6.8	Phase signal estimations for vibrometry data of a 200 Hz vibrational displacement before and after clutter filtering. . . . .	113
6.9	STFT and cross correlation plot describing the forward displacements observed in a vehicular vibration data collection of a hybrid Kia Sportage.	115
6.10	Time series and spectra plots describing the displacements observed in a vehicular vibration data collection of a hybrid Kia Sportage. . . .	116
6.11	Clutter ridge diagrams for the scenario of a moving platform around otherwise stationary clutter. . . . .	118
6.12	The full processing chain used to decode a VRBC message when both radar and transponder platforms have vibrational noise. . . . .	124

# Acknowledgements

I would like to begin by thanking my advisor, Dr. Jeffrey Krolik. You have helped me grow not only in my technical knowledge but in how I approach problems, communicate technical content, and view success. I would not be writing this dissertation if it were not for your patience when I was stubborn and advice when I was lost. Thank you for seeing my potential and mentoring me these past five years.

I would also like to thank Dr. Loren Nolte, Dr. Robert Calderbank, Dr. Stacy Tantum, and Dr. Donald Bliss for serving on my committee. Dr. Nolte, you provided me with my first TA'ing opportunities, and I am grateful for having always felt supported. Dr. Calderbank, you gave me the opportunity to contribute to a research area that I would have otherwise likely not have delved into during my graduate career. Thank you and Dr. Ahmed Hareedy for providing me with a wonderfully collaborative experience during that project. Dr. Tantum, you have been a role model to me in many ways. Your passion and dedication to teaching is truly inspiring, and I appreciate the times that you have advocated for me when professional development opportunities presented themselves. Dr. Bliss, though we did not interact often, your insight and expertise proved vital in the development of this work. Thank you all!

A special thanks is in order for all of the wonderful lab mates I have had the pleasure of working with. Dr. Michael Martinez, you served as a mentor during my first years of graduate school and have always been there to read through a paper for

me, work through a problem, or provide an opinion on anything I have considered pursuing. Dr. Anil Ganti, you and Michael are who I will think of when I look back on my graduate career. The countless hours in lab meetings or gathering data would not have been the same if it weren't for the random conversations we had about your haircuts, sewing projects, or random technical interests. I also would like to thank my former lab mate Dr. Andrew Young and recently acquired lab mates Shannon Pinnell and Elliot Mueller. You all have been great to share an office with and our conversations have left me a better researcher.

To my parents, I want to thank you for constantly believing in me even when I did not believe in myself. Though you may not always understand what I am working on exactly, I always feel your support. To all my friends both at Duke and in the greater Triangle community, thank you for making the last five years fun even if a global pandemic tried to get in the way.

I would be amiss if I did not quickly recognize the contribution of my little Microsoft Surface Pro that managed to host the majority of my simulation and data processing work. It has become a running joke that I should become a sponsor for the Surface Pro, and I do not disagree as basically all the work in this dissertation was made possible through it even if other devices would have been better suited.

On a more serious note, I would like to finally thank my husband, Aaron Centers. The love and support that you have shown me as I work towards this degree and look towards a future career goes unmatched. You have gone from the title of boyfriend to fiancé to husband in these last five years, and my relationship with you remains my greatest achievement. I look forward to our future and am thankful for our wonderful past and present.

Table 1: Summary Key Variables

Variable	Definition	Units
$\alpha_{\text{obj}}$	gain/attenuation	-
$\beta$	chirp slope	Hz/sec
$\eta(t)$	band-limited AWGN	-
$\theta$	angle	radians
$\lambda_0$	chirp starting wavelength	m
$\sigma_{\text{obj}}$	radar cross section (RCS)	$\text{m}^2$
$\tau$	time delay	ssec
$B$	waveform bandwidth	Hz
$c$	speed of light	m/sec
$d(t)$	displacement signal	-
$\mathbb{E}[\cdot]$	probabilistic expectation	-
$f_0$	chirp starting frequency	Hz
$n(t)$	AWGN	-
$\Pr(\cdot)$	probability	-
$r$	range	m
$s_{\text{RX}}(t)$	received waveform	-
$s_{\text{TX}}(t)$	transmitted waveform	-
$T$	active chirp duration	sec
$T_{\text{PRI}}$	waveform bandwidth	sec
$v$	velocity	m/sec
$x(t)$	excitation signal	-

# 1

## Introduction

Radar are well known for being able to provide range, velocity, and angular information of the objects in their field of view. This comes at no surprise since the term ‘radar’ originates from being an acronym for radio detection and ranging. Today, the acronym stands alone, while the system’s intended purposes nonetheless remain the same. What may be less obvious though is that radar ranging techniques can additionally allow vibrations, rotations, and other dynamic movements to be discerned. To do so, the instantaneous frequency, i.e. velocity or Doppler, of the signal that returns to the radar after reflecting off of an object must be observed over time. From one time interval to another, small changes in the object’s velocity due to smaller dynamic movements reveal themselves as sidebands, or offset frequencies, around a target’s bulk Doppler frequency when looking at a conventional range-Doppler map. In the literature, these features are sometimes referred to as micro-Doppler content.

Micro-Doppler techniques have been shown to increase the usefulness of radars in classification systems across multiple domains. As one can imagine, it is the time-varying movements of things that often reveal what the object is or what the object is doing. For example, being able to characterize a person’s arm swinging while

walking can aid in gait analysis systems [1]. Furthermore, a falling person can be identified in part by observing the person's arm movements [2]. Similarly, a micro-Doppler model of a drone's propellers during flight proves advantageous in airspace monitoring [3]. Without micro-Doppler signatures of the drone, it might otherwise be mistaken for a similarly-sized bird. Research spaces such as hand gesture analysis also use micro-Doppler features to better translate nonverbal cues [4].

Gesture analysis provides a prime example of how radar systems often make use of more than just one of the common categories of radar tasks - detecting, tracking, and classifying. More often than not, it is necessary to do all three. Per the example, a hand gesture analysis system must first detect the presence of someone's hand(s). Then, it must track the bulk movement of the hand so that it can be continuously monitored. The final, perhaps most interesting step, is then to classify the hand gesture to provide some amount of meaning. This can range from a hand flying up to indicate that something needs to stop, a hand cycling towards one's body to indicate something needs to come closer, or even perhaps gestures that mean something very discrete in sign language. It is the classification portion of this system that benefits most greatly from micro-Doppler techniques, as small wiggles in the subject's fingers could be the difference between the described stop motion and a friendly wave.

Of particular interest in this dissertation is how micro-Doppler methods can be used and further developed to capture information about an object's vibrations to improve a set of application-driven systems. Radar vibrometry techniques have been shown to successfully detect vibrations only a fraction of the radar's wavelength in amplitude [5]. With the recent advent of affordable millimeter wave (mmW) radar systems-on-a-chip, exploiting vibrations as small as tens of micrometers has become accessible. For context, human chest displacements due to their heart beating are around 200 to 500 micrometers [6]. Applications where this level of precision

are needed have previously been limited to comparatively large and expensive laser Doppler vibrometers (LDVs).

Operating at relatively higher frequencies in the visible band, LDVs have an even smaller wavelength than mmW radars which allows them to observe even smaller vibrations than that of human chest displacements. Even with the advances of modern technology though, this precision comes at a significant cost. Modern LDVs cost upwards of tens of thousands of dollars. For instance, the entry-level Polytec VibroGo, a portable single-point LDV made by a leading LDV producer, costs approximately \$30k [7]. Such a device surely could not be used by the average consumer due to its price. Certainly, LDVs are therefore unfavorable for use in networks where multiple vibrometry sensors must work together to complete a task. Unless of course you are the wealthy owner of a priceless jewel in a classic spy film. Additionally, even the portable VibroGo is sized comparably to a loaf of bread. This can make them difficult to equip to objects like a bike.

Despite their price tag and size, LDVs have historically been the primary non-contact solution for measuring vibrations in applications where attachable sensor alternatives are either not practical or ill-suited. Take for example when the object of interest is fragile, liquid, difficult to reach, or high temperature [8]. Since their development, LDVs have accordingly proved advantageous in research communities aiming to better understand the world around all of us through the analysis of these otherwise immeasurable movements. The first published application for laser vibrometry was on measuring turbine blade vibrations while in motion back in 1969 [9]. Turbine measurements clearly demonstrate an instance where an attachable transducer alternative poses challenges. Since that 1969 publication, LDVs have been used to make measurements on loudspeakers [10], automobiles [11], instruments [12], and hydroelectric dams [13] in addition to on less obvious entities like crabs [14] and plants [15]. Yes, you read that right. It turns out that LDVs allowed scientists in the

1980s to study precisely how the drumming of male fiddler crabs during courtship is sensed by their female counterparts.

As impactful as LDVs have been on the scientific community, many systems wishing to utilize vibrometry measurements in public settings require a more affordable and smaller option. In such cases, some amount of precision degradation is often allowed. The proliferation of mmW radars, which cost orders of magnitudes less than LDVs while also having a smaller size, weight, and power requirement, have fit these criteria and become the primary contender in this market. As one might therefore expect, mmW radars have already found use in technologies such as drowsiness detection systems where the movements of interest are of magnitudes perceptible by mmW, like heartbeat-correlated chest displacements [16]. Millimeter wave radar vibrometry has also proven useful for applications like nondestructive examination of dielectric materials [17], structural health monitoring [18], and aging in place monitoring systems [19].

## 1.1 Dissertation Impact

In this dissertation, solutions are presented that aim to demonstrate how mmW radars can be used as a vibrometer to do tasks previously only made possible through expensive laser Doppler vibrometers (LDVs). The work discussed is often put in the framework of an application of interest such as speaker identification or anything-to-vehicle (X2V) communications, but some of the techniques discussed expand the capabilities of mmW radar vibrometry more broadly. For example, Chapter 4 highlights how using the entirety of a mmW radar's return can provide improved classification of observed vibrations. Though it is discussed in the framework of wireless communications, this concept and much of the associated processing chain could serve useful in other areas of interest in vibrometry. For instance, vibrometry in material testing could find that using the full signal as we did could provide a signif-

ificant improvement in classifying types of structural fatigue as opposed to traditional mmW radar processing techniques.

The applications that are focused on in this dissertation include human speech analysis as well as wireless communications. Within human speech analysis, we consider mmW radar vibrometry for both speaker identification and speech recognition. As for wireless communication, we look develop a system geared towards noninvasively adding communications where mmW radar sensing is already used, such as on vehicles. These applications were chosen in part due to the trend in today's society for everything to be connected. We find that mmW vibrometry provides untapped potential in this space. As 'smart city' planning and implementation takes wind in many cities in first-world countries like Singapore, Dubai, and Boston, data-driven solutions for many tasks are being sought after. These data-driven systems require data acquisition and data sharing. Millimeter-wave radar vibrometry offers a way to do both.

Radar vibrometers at mmW are not only able to measure traditional vibrations like those that are the bi-product of gas engines, jet turbines, and crab drumming. They can also acquire information about sources of sound, whether that be a human or loudspeaker. Since sound is the result of displacing air, and displacing air is most often accomplished by displacing a surface exposed to the air, vibrometers need only to observe the corresponding surface's displacement. For loudspeakers, this surface is referred to as its diaphragm. The surface in human speech is a bit more complicated in that the source of air displacement comes from our lungs expanding and contracting, though our vocal chords and mouth play a key part in modifying the airflow to produce a desired sound. Using mmW vibrometry to observe the displacements associated with sound production in loudspeakers or humans opens up the possibility of an affordable stand-off speaker identification or speech recognition system that is unaffected by the presence of acoustic noise.

As will be seen within this dissertation, when vibrations associated with speech generation contain information primarily related to one of these tasks (speaker ID or speech recognition), methods of identification or password recognition can become more private. In a society where data is being used for an increasing number of applications, ensuring that the data collected is minimally unnecessary and private is vital. Acoustic data of speech has long been known to contain an ample amount of private information whether that be personally-identifiable information or information regarding a person's mindset, health, or beliefs as is often captured through their choice in words spoken. The goal of using data that contains less task-irrelevant information is a principle in the General Data Protection Regulation (GDPR) used in Europe to help minimize the harms that can come from building a data-driven society [20]. Even though the U.S. does not have any similar regulation, Americans have trended toward upholding values like respecting data source privacy when possible. Regardless, mmW radar vibrometry in human speech analysis is explored in this work and demonstrates an initial hope toward the development of a more private speaker identification system.

As mentioned, mmW radar vibrometry additionally provides a way to share data. By developing a system where vibrational displacements can be meaningfully created and then accurately sensed, a new form of backscatter communications can be conceived. Backscatter refers to the received signal once a waveform has been transmitted and reflected back toward the radar. Therefore, backscatter communication is defined as a method by which backscatter signals are modified to contain a desired message such that the receiver can then decode it and have the message. The most common form of backscatter communication is RFID. RFID at mmW, however, requires the use of complex and expensive antenna arrays. In this work, we use vibrations to modulate radar backscatter without needing costly arrays.

By sharing the data via backscatter communications, it can be seen that the

system does not require the data sharing source, which we often refer to as the transponder, to use any RF bandwidth. This implication serves as particularly useful since acquiring a band on the RF spectrum has become increasingly difficult and expensive. In this work, the application of anything-to-vehicle (X2V) communications is presented for our new vibrational radar backscatter communication system since mmW radars already exist in modern vehicles. There are also already a large number of advocates for having vehicles communicate to each other and their surroundings. It should be noted though, that the solutions these advocates currently push require some amount of RF spectrum. The two most popular connected vehicle solutions include direct short-range communications (DSRC) and cellular V2X (C-V2X) [21]. DSRC employs direct RF communications between a transmitter and receiver using an allocated band of the RF spectrum, traditionally at 5.85 – 5.925 GHz. C-V2X allows for DSRC-type communication while also taking advantage of the mobile operators spectrum band. In doing so, vehicles are able to receive information from the cloud regarding road and traffic conditions in the area.

After decades of extensive testing, collaboration, and a regulatory proposal by the National Highway Traffic Safety Administration (NHTSA) [22], connected vehicle protocols like DSRC and C-V2X have barely made their way into the automotive market. Much of the reason for that is because sensors for advanced driver-assistance systems (ADAS) like millimeter-wave radars have won over the portion of the RF spectrum that both systems wish to operate at. Stake holders across the board have recognized that the immediate benefits of increasing the sensing capabilities of a vehicle outweigh those of allowing for communication instead. This battle for the spectrum, however, does not change the fact that vehicles having the capability to share warning messages and situational awareness knowledge could both reduce the number of automotive accidents and injuries as well as help make transportation more efficient. Solutions that allow both sensing and communication in automo-

biles is therefore highly desirable, and vibrational radar backscatter communications (VRBC) as presented in this dissertation does exactly that.

An additional benefit of requiring no RF bandwidth by a transmitter is that it avoids interference from channel congestion. In DSRC, only seven channels of 10 MHz bandwidth are available within a geographical area. This requires users to potentially have to wait for other users to get off of a channel so that they could then broadcast a message. In backscatter communication systems like ours, users can avoid interference and scheduling latency due to other users because the mmW radar sensors can separate return based on the direction it comes from. The number of channels available is then only dependent on the spatial resolution of the sensor. This characteristic of VRBC only further strengthens the appeal of mmW vibrometry for high traffic communication scenarios like those that vehicles trying to communicate often find themselves in.

Incorporating some of the presented mmW vibrometry methods into practice could be easy, like acquiring one's own mmW radar and using the methods presented to observe the small vibrations of a loudspeaker's diaphragm for quality testing. Implementing full mmW vibrometry systems into applications like X2V, however, will require more effort. Implementing a new X2V system requires regulation and cooperation amongst different government and industry groups to truly reap the benefits that this work could provide. Millimeter wave VRBC requires adding vibrating transponders, perhaps license plates, to vehicles and other nodes of interest during driving in addition to processors that can perform the signal processing chain to detect, isolate, and decode vibrational messages. All of this requires cooperation amongst the parties developing the system, and though it is not difficult in theory, unification on systems like this could be more difficult to achieve in reality.

Despite all the foundational work presented with this document, mmW vibrometry in applications like communication systems is only in its infancy. In other words,

the impact of this work has only began to be truly realized. As this research area develops, vibrometry in communications, material testing, aerospace, health care, and more could find that mmW radars are the accessible and affordable solutions they have been looking for when it comes to observing and using small vibrational movements in their various systems. Who knows, maybe in the future more private human speech-based systems will become standard or our cars will talk to each other using their mmW radars and a vibrating license plate. Maybe such an X2V system is exactly what will keep you from wasting hours in traffic jams or finding yourself in dangerous traffic situations.

## 1.2 Technical Contributions

Throughout this dissertation, the intricacies of an object's vibrational effects on a radar's received signal are modelled and considered in application. Though mmW radar vibrometry itself can serve as useful in many systems, this work presents advances in mmW radar vibrometry techniques motivated by speech analysis and digital communications.

To begin, Chapter 2 shares background knowledge pertaining to mmW radars. Math introducing the assumed transmit signal is given, and properties of mmW signals are additionally discussed.

Chapter 3 explores how mmW radar vibrometry can be used in non-acoustic human speech analysis. The resolution provided by mmW radars permits the vibrations induced by vocal chord movements to become observable, thus allowing for a comparison between mmW vibrometry data on the area surrounding one's vocal chords and conventional acoustic data. The speech analysis systems of interest in this chapter are speaker identification and speech recognition. In this chapter, vibrometry visualizations lead to the conclusion that vibrometry data sets are substantially different from acoustic sets from the same instances. It is this observation

that leads to the exploration of privacy-minded versions of speech recognition and speaker identification. Specifically, we find that mmW vibrometry provides the potential for a content-blind speaker identification system, though further work with a more extensive data set is required to fully justify this claim.

Chapter 4 introduces our novel communication system that has been termed vibrational radar backscatter communication (VRBC). VRBC provides a communication method that avoids requiring a transmitter to emit RF energy, while also coexisting with traditional radar capabilities. By modulating the vibrations of a transponding object’s surface, an observing radar can detect the modulations and decode the message using radar vibrometry principles and methods. VRBC allows for multiple communication channels simultaneously through the mmW radar’s ability to separate return in accordance with its spatial resolution. In this chapter, the favorable application of X2V is further used as motivation, and the details for detecting, isolating, and decoding vibrational transponders in this application are provided. Initial rates around 50 bps are achieved using a cheap and resonant transponding surface placed approximately 5 meters away from the radar.

Then in Chapter 5, a theoretical bound for VRBC rate is provided. The ultimate goal in any communication scheme is to provide as large a rate as possible while remaining robust. Developing a useful upper bound for VRBC is therefore important. In this chapter, the trade-offs existing between different system parameters are provided. Furthermore, justification for certain recommended design choices are also given. This section shows that no matter how good a VRBC processing chain becomes, VRBC is inevitably limited in data rate by the system’s radar parameters and transponder design.

Chapter 6 transitions to methods useful for using VRBC in practice. Details and scenarios that require further clarification like using resonant transponding surfaces, designing a more ideal clutter filter, and minimizing errors due to vibrational noise

at the radar or target platforms are discussed. After accounting for resonant surface effects, we show that the same real data collection exemplified in Chapter 4 greatly improves in performance to achieve a rate of 80 bps.

In the conclusion, Chapter 7, there is a brief discussion on areas of future work related to this dissertation as well as a summary of the document.

# 2

## Background

Fundamentally, radar systems consist of a transmitted signal that reflects off of nearby objects and returns to a radar receiver. The word ‘nearby’ here is entirely relative, as over-the-horizon radar manages to sense objects thousands of kilometers away by transmitting their signal toward the ionosphere, having it reflect off of targets, and then observing the return that follows the same path back to a receiver. Alternatively, other radars find application in indoor systems where targets are expected to be within tens of meters.

To highlight a few key variations in radar systems, consider a textbook radar system. Most commonly, radars have the transmitter and receiver located at the same place. This is referred to as a monostatic systems. Another phrase used for this type of radar system is that the transmitter and receiver are co-located. A monostatic radar system also often infers that the same oscillator that generated the transmitted waveform is available to the receiver. If this is the case, the received signal’s amplitude and phase can accurately be referenced back to the transmitted signal’s amplitude and phase. The ability to reference the transmitted system accurately and precisely means that coherent processing can take place.

On the other hand, there are radar systems where the transmitter and receiver are not in the same place. These are known as bistatic systems. It can even be the case that the transmitted signal is entirely or partially unknown. In these types of systems, this is usually because opportunistic RF sources are expected to be available and a radar receiver is equipped to estimate sources that are present and use them for radar operation. Because these radar systems do not require any intentionally active transmitting components, these systems are referred to as passive radar systems. There exist pros and cons to the different types of systems. For instance, it can be advantageous to covertly perform radar tasks without broadcasting one's own signal. However, having the ability to coherently process a signal greatly improves performance and simultaneously avoids the need to perform waveform estimation.

Regardless, physics tells us that a given object's range relates to how long it takes the signal to follow the path from transmission to reflection to reception. We also know that the Doppler effect, or apparent change in a signal's frequency, provides us with velocity information on perceived objects. Though radar systems come in different forms, they all rely on being able to exploit at least one of these phenomena to gain insight on different objects in their field of view. In this dissertation, we assume a monostatic and coherent system.

## 2.1 Frequency Modulated Continuous Waves (FMCW)

To develop mmW vibrometry techniques for any application of interest, the radar waveform is first evaluated. The work described within this dissertation assumes the use of mmW frequency modulated continuous wave (FMCW) radars. FMCW is commonly used as it provides both range and velocity estimation capabilities, while also decoupling the pulse (or chirp) width from the waveform bandwidth. Modern mmW radars, such as the suite of automotive and industrial radars that Texas Instrument (TI) released in 2018, use FMCW for these very reasons.

Throughout this dissertation, real data is often presented. This data was captured using the TI IWR1443, one of TI's mmW FMCW radars that operates at 77 GHz. This specific radar boasts up to 4 GHz of continuous bandwidth [23]. We therefore limit the work in this dissertation to assume transmit waveforms that can be realized on this device. Furthermore, we assume linear frequency modulated (LFM) signals. The transmitted signal can be written as

$$s_{\text{TX}}(t) = \alpha_{\text{TX}} e^{j2\pi f_0 t} \sum_{g=0}^{G-1} u_p(t - gT_{\text{PRI}} - t_0), \quad (2.1)$$

where  $\alpha_{\text{TX}}$  is the gain/attenuation associated with the transmitter,  $f_0$  is the start frequency of the chirps,  $G$  is the number of chirps sent,  $T_{\text{PRI}}$  is the duration of a chirp which is also known as the pulse repetition interval (PRI),  $t_0$  is the start time of the waveform, and  $u_p(t)$  is the periodic chirp/LFM baseband waveform. The baseband chirp can be fully described as

$$u_p(t) = \begin{cases} e^{j\pi\beta t^2} & 0 \leq t < T \\ 0 & \text{otherwise} \end{cases}. \quad (2.2)$$

In Equation 2.2,  $T$  is the active duration of a chirp which must be less than or equal to  $T_{\text{PRI}}$ . The chirp slope is  $\beta = \frac{B}{T}$ , and  $B$  is the bandwidth of the chirp. The duty cycle of the continuous wave is then calculated via  $T/T_{\text{PRI}}$ .

The received signal consists of backscatter from objects with complex radar cross sections (RCS). For example, consider a car or a tree. The reflected radiation from these objects will depend on the radar waveform's frequency and incident angle, the objects physical size and shape, and material characteristics of the object. In reality, exact methods of RCS modeling for these scatterers are themselves intricate even for seemingly simple shapes. Efficient RCS measurement and modeling methods is a whole area of research for this reason [24]. Furthermore, exact modeling methods for use in a radar system require a fully known description of the backscatter from

each possible object. This is typically not feasible or easily interpretable in digital processing methods. This is why it is common for objects to be modeled as a sum of point scatterers [25, 26]. Though this is an approximate modeling method, it often results in minimal variations in SNR that are typically considered acceptable in most radar systems. How many points an object should be modeled with then depends on the radiation pattern of the object, its distance from the observing radar, and the range/angle resolution of the radar.

From this point forward, the start time,  $t_0$ , is assumed to be 0 without loss of generality. The return signal for a monostatic radar is therefore modelled a sum of many point scatters in additive white Gaussian noise (AWGN)

$$s_{\text{RX}}(t) = \sum_{k=1}^K \tilde{\alpha}_k e^{j2\pi f_0(t-\tau_k(t))} \sum_{g=0}^{G-1} u_p(t - \tau_k(t) - gT_{\text{PRI}}) + \tilde{n}(t), \quad (2.3)$$

where  $K$  is the number of point scatterers being modeled,  $\tilde{\alpha}_k$  is the point-specific amplitude after scaling due to signal propagation as a function of the target's range and RCS,  $\tau_k(t)$  is the return time delay from point  $k$ , and  $\tilde{n}(t)$  is the AWGN

The complex amplitudes,  $\tilde{\alpha}_k$ , are Gaussian random variables with a phase drawn from a uniform distribution and magnitude drawn from a Rayleigh distribution in accordance with the Swerling model. Furthermore, they are zero-mean with a variance calculable via the radar range equation,

$$\mathbb{E}[|\tilde{\alpha}_k|^2] = \underbrace{\left(\frac{G_{\text{TX}}}{4\pi r_k^2}\right)}_{\substack{\text{ratio of} \\ \text{TX power} \\ \text{incident upon} \\ \text{the object}}} \underbrace{\left(\frac{\sigma_k}{4\pi r_k^2}\right)}_{\substack{\text{ratio of} \\ \text{the power} \\ \text{reflected back} \\ \text{to the radar}}} \underbrace{\left(\frac{1}{L_s L_a(r_k)}\right)}_{\substack{\text{losses due to} \\ \text{the system and} \\ \text{atmosphere}}} \underbrace{A_{\text{eff}}}_{\substack{\text{effective} \\ \text{aperture} \\ \text{size of} \\ \text{antenna(s)}}}. \quad (2.4)$$

$G_{\text{TX}}$  is the transmission gain,  $\sigma_k$  is the radar cross section (RCS) of the object, and  $L_s$  is the loss in linear units due to the system. It should also be noted that through the gain term,  $G_{\text{TX}}$ , the transmit waveform amplitude,  $\alpha_{\text{TX}}$  is captured.  $L_a(r_k)$  is

the loss in linear units due to the atmosphere,

$$L_a(r_k) = 10^{\kappa r_k / 5000}, \quad (2.5)$$

where  $\kappa$  is the loss in decibels per kilometer due to the atmosphere.  $A_{\text{eff}}$  is the effective aperture size of the receiving antenna(s), which is a function of the gain from the receive antenna(s),  $G_{\text{RX}}$ , and the operating wavelength,  $\lambda_0 = c/f_0$ . The general relation for the effective aperture in terms of the receive antenna gain is given by

$$A_{\text{eff}} = \frac{\lambda_0^2}{4\pi} G_{\text{RX}}. \quad (2.6)$$

This Swerling model for the amplitude terms comes from assuming that a given scatterer contains multiple reflecting surfaces with smaller, individual radar cross sections. It is the Central Limit Theorem, that allows us to combine the separate effects from each sub-surface to approximate the scatterer's scaling term into an inclusive single Gaussian term with the statistical properties described. This holds true for an object within a single spatial resolution cell from the perspective of the radar. When an object expands beyond the radar's resolution, multiple points must be modeled to approximate the object's return.

The delay terms for each point scatterer can be written as

$$\tau_k(t) = \frac{2(r_k + v_k t)}{c}. \quad (2.7)$$

Here,  $c$  is the speed of light,  $r_k$  is the range of the  $k^{\text{th}}$  point from the radar, and  $v_k$  is an all encompassing radial velocity term for the  $k^{\text{th}}$  point from the perspective of the radar. This velocity can be broken down into key components such as the bulk velocity of the radar platform, bulk velocity of the point, and vibrations present at the platform and point, but for now it is left as a singular term.

Conventionally, received backscatter of the transmitted waveform is then de-chirped for each receive element. This consists of multiplying the normalized trans-

mitted signal by the complex conjugate of the received. If we ignore the minimal chirp edge effect, this provides

$$\begin{aligned} y(t) &= s_{\text{TX}}(t)s_{\text{RX}}^*(t) \\ &= \sum_{k=1}^K \tilde{\alpha}_k e^{j2\pi f_0 \tau_k(t)} \sum_{g=0}^{G-1} \text{rect}\left(\frac{t - gT_{\text{PRI}}}{T} - \frac{1}{2}\right) e^{j\pi\beta(2\tau_k(t)(t-gT_{\text{PRI}}) - \tau_k^2(t))} + \tilde{n}(t) \end{aligned} \quad (2.8)$$

where  $\text{rect}(\cdot)$  is the rectangle function which is 1 when its argument is between  $[-\frac{1}{2}, \frac{1}{2}]$  and 0 otherwise.

Following common radar signal processing terminology, the various dimensions of the raw, de-chirped radar IQ data include the element, fast-time, and slow-time dimensions. Samples along the element dimension consists of samples captured at the same time across the various received elements. Equation 2.8 models the return seen by a single element. Across elements, realizations of random variables will differ, but more importantly, delays differ slightly due to differences in element position. In the frequency domain, these delays across the antenna elements provide bearing.

The second dimension, fast-time, consists of samples within a chirp duration,  $T_{\text{PRI}}$ . The mathematical representation of the fast-time signal is

$$y(t, g) = \sum_{k=1}^K \tilde{\alpha}_k e^{j2\pi f_0 \tau_k(t)} e^{j\pi\beta(2\tau_k(t)(t-gT_{\text{PRI}}) - \tau_k^2(t))} + \tilde{n}(t) \quad (2.9)$$

for  $gT_{\text{PRI}} \leq t < gT_{\text{PRI}} + T$ , where  $g$  indicates which chirp the samples are from. The delays,  $\tau_k(t)$ , are often assumed approximately constant for this time interval. Specifically,

$$\tau_k(t) \approx \frac{2(r_k + v_k(gT_{\text{PRI}} + \frac{T}{2}))}{c}. \quad (2.10)$$

Traditionally, this time dimension relates to range in the frequency domain due to this approximation. This can be seen by plugging in Equation 2.10 into 2.9, and observing

that the first exponential in Equation 2.9 becomes a complex constant which can be grouped into the amplitude term, while the second exponential simplifies to a complex sinusoid,

$$y(t, g) = \sum_{k=1}^K \tilde{\alpha}_k e^{j2\pi\beta\tau_k(t)t} + \tilde{n}(t) = \sum_{k=1}^K \tilde{\alpha}_k e^{j2\pi\frac{2\beta}{c}(r_k + v_k(gT_{\text{PRI}} + \frac{T}{2}))t} + \tilde{n}(t). \quad (2.11)$$

Working with the signal in the fast-time dimension is useful in estimating the range as Equation 2.11 demonstrates how peak frequencies after a discrete Fourier Transform (DFT) directly relate to an object's range during a particular chirp,  $f_k = \frac{2\beta}{c}(r_k + v_k(gT_{\text{PRI}} + \frac{T}{2}))$ . At the  $g^{\text{th}}$  chirp, the range of the  $k^{\text{th}}$  object is naturally  $(r_k + v_k(gT_{\text{PRI}} + \frac{T}{2}))$ .

The third dimension mentioned is referred to as slow-time and consists of samples at the same moment within a chirp across multiple chirps. Usually slow-time signals are found by taking a DFT in fast-time first and then looking at the complex amplitudes across chirps for a particular range-related frequency. This is most easily understood by considering Equation 2.9 and observing that the first complex exponential is the time-dependent amplitude for the  $g^{\text{th}}$  chirp at peak frequency  $f_k$ . The slow-time signal at a particular peak frequency indexed now by  $m$  is

$$y(t, m) = \sum_{k=1}^{K_{r_m}(t)} \tilde{\alpha}_k e^{j2\pi f_0 \tau_k(t, m)} + \tilde{n}(t) = \sum_{k=1}^{K_{r_m}(t)} \tilde{\alpha}_k e^{j2\pi\frac{2f_0}{c}(r_m + v_k t)} + \tilde{n}(t). \quad (2.12)$$

Notice that the set of points  $K_{r_m}(t)$  is now dependent on both  $r_m$  and  $t$ . The  $r_m$  dependency is used because this slow-time signal is only representative of the scatterers at a particular range-related peak frequency which is much less than the total number of scatterers in the environment making up the full return. The time dependency is presented as a way to generalize the model such that when observing the slow-time signal of a particular range over time, scatterers that have velocities causing them to enter and exit the observed range during the observation time are

accounted for appropriately. As Equation 2.12 shows, slow-time provides Doppler information in the frequency domain as any object's observed peak frequency in this dimension is  $f_k = \frac{2f_0}{c}v_k$ .

These FMCW radar signal models are used throughout the work presented in this dissertation. Object vibrations throughout will appear as time varying displacements in the delays described by Equation 2.7. Because mmW frequencies are assumed, vibrations of magnitudes as small as hundredths of a millimeter (tens of micrometers), can be modeled and detected for use in interesting applications. Operating at mmW frequencies, however, does come with trade-offs that require being well understood.

## 2.2 Properties of Millimeter Wave Backscatter

The proliferation of mmW radars is in large part thanks to the autonomous vehicle industry. They have become a primary sensor in ADAS (Advanced Driving Assistant Systems) for detecting, classifying, and tracking surrounding objects like other vehicles, bicycles, and pedestrians. Relying on radars in such systems serves as advantageous over cameras and LiDAR due to their ability to operate well in inclement weather and moments of darkness as well as sense at sufficiently long ranges.

Naturally, mmW radars prove to be useful both in and out of the automotive industry, as previously mentioned in Chapter 1. Specifically operating at mmW provides a few benefits in such applications including the miniaturization of the required antenna arrays as well as improved resolution. Millimeter waves also provide the ability to sense at sufficiently long distances for many applications without experiencing too much attenuation. It is the improvements in power-efficient millimeter wave radar components that reduces the cost-benefit of lower frequency alternatives.

The angular resolution (Rayleigh resolution) of a radar's antenna array is calcu-

lable via

$$\Delta\theta = \frac{\lambda_0}{L} \quad (2.13)$$

where  $L$  is the length of the array in meters. For a particular resolution, 2.13 shows that the length of the array must scale inversely with the wavelength. To demonstrate this, consider a uniform linear array (ULA) required to have at least  $10^\circ$  angular resolution when the operating frequency is 77 GHz (W-band), the current operating frequency of most automotive radars. The resulting array must span a length of at least 22 millimeters. Even if operating at the legacy automotive radar frequency of 24 GHz (K-band), an antenna array with an equivalent resolution will scale up to 71 millimeters. If conversely a certain array size is given, angular resolution improves at millimeter-wave operating frequencies when compared to conventional, lower radar operating frequencies.

Generally, range resolution is also improved at higher frequencies due to the availability of larger bandwidths. Because lower frequencies are able to travel farther for the same amount of transmit power, many systems find these frequencies desirable making it more difficult to gain the rights to a larger bandwidth. Consequently, this is less true at higher frequencies. Automotive mmW radars at 77 GHz, for instance, have been allotted 4 GHz of bandwidth. Because the range resolution directly relates to the bandwidth of the signal,

$$\Delta r = \frac{c}{2B}, \quad (2.14)$$

operating at a frequency like 77 GHz allows the system to achieve better range resolution. In the automotive radar case, where 4 GHz of bandwidth is available,  $\Delta r = 37.5$  millimeters.

With resolution and device size improving at higher frequencies, it is important to acknowledge that the general trend at higher frequencies is that they do require

more power to travel the same distance. Fig. 2.1 shows how atmospheric attenuation at 20°C, for example, increases from approximately 0.09 dB/km to 0.04 dB/km for RF waves at 24 versus 77 GHz. Fig. 2.2 also shows the increase in attenuation at higher operating frequencies in the presence of rain. This same general phenomena carries over for attenuation through materials. Consequently, through-the-wall radar usually operates at only a few GHz [27]. At millimeter waves, very few materials are transparent to the electromagnetic wave. Attenuation in clothing materials like a cotton shirt or even a sweater do manage to remain lower than 0.5 dB, which is beneficial in the aforementioned application of gait analysis [28]. Furthermore, materials like Plexiglass and Teflon have sufficiently low dielectric constants and loss tangents allowing them to be used in radome design to hide and shield mmW radars without invoking consequential attenuation [29]. Most other objects, however, are not transparent and primarily reflect incident millimeter wave radiation, thus allowing for them to be well detected by the radar system.

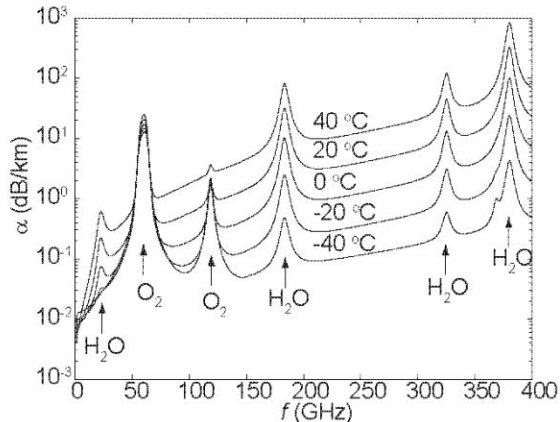


FIGURE 2.1: Obtained from [28].

Millimeter wave radar producers have made great improvements in making their radars higher power while still affordable, thus countering the drawback of increased propagation loss and allowing for mmW radars to see automotive targets at up to a few hundred meters. For example, Texas Instrument's IWR1443 mmW radar

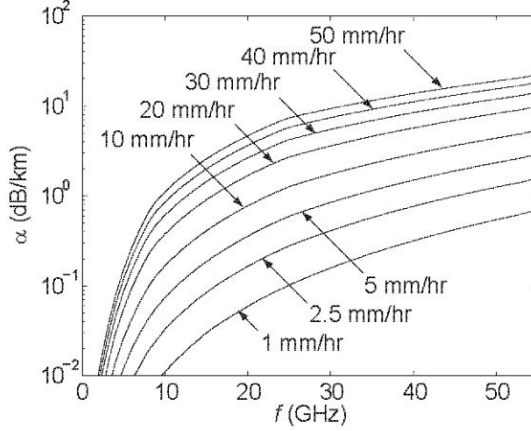


FIGURE 2.2: Obtained from [28].

evaluation module costs only a few hundred dollars (even less if only the radar chip is purchased to be integrated into a custom system). Even at this affordable price level, this specific radar still provides as much as 12 dBm of transmit power thanks to their advances in complementary metal-oxide semiconductor (CMOS) chip design. In following the trend to have smaller systems and improve resolution, it is quite likely that automotive radars will further increase their operating frequency as semi-conductor technology continues to advance [30]. For now though, most high resolution radars are at 77 GHz.

# 3

## Millimeter Wave Vibrometry for Human Speech Applications

### 3.1 Motivation of Vibrometry for Human Speech Applications

Vibrometry has historically allowed loudspeaker manufacturers to study and refine the diagram movements in their products. It is sensible to therefore consider how similar techniques could be used to study human acoustic production, as was seen in [31]. Analysis of speech generation using a mmW radar presented itself as a feasible area of research because LDVs have had some success in this space and because speech generation is closely related to vital signs monitoring. When released for public purchase and use in 2018, Texas Instrument's mmW radars were advertised alongside a handful of lab experiments to help demonstrate the radars' capabilities. One of these experiments was vital signs monitoring [32]. Since then, researchers have refined mmW radar vibrometry processing methods largely to improve vital signs monitoring techniques [33–35]. From there, the question arise whether full biometric identification (ID) or speech recognition can be achieved using the mmW radars.

Biometric identification has long been conducted using the audio of speech [36]. This is an intuitive approach since it mimics how humans distinguish who it is that is speaking to them when they are not in sight of the speaker. Like the machine learning processes used today for speaker identification, we as humans listen to various people speak over multiple instances in our lives and build an internal model to help us distinguish between certain people’s voices. For some people, we manage to build a very good model of what their speech sounds like. This is why when we call loved ones over the phone, we can tell whether the voice on the other end is them. For others, we have a less refined model of their speech because we simply have not interacted with them enough.

When possible, however, we often naturally turn to look at who is speaking to help conduct more accurate identifications. Similarly, biometric ID can look towards the source as well. For instance, some solutions look the same way we do by visually observing the speech source and conducting classification using techniques like facial recognition. In this work, a slightly different approach is considered where mmW radars are used to observe a speaker in a way that a human cannot - larynx vibration analysis. Because speech is the product of a person’s vocal folds modulating the air flowing up through their throat, we envisioned a speaker ID method that directly measures the source of speech by observing these glottal movements. In contrast to acoustic-based identification methods, glottal movement-based identification would be less susceptible to disguising attempts and much more robust in places of significant acoustic noise [37].

Speech recognition is an additional area of promising impact in society that traditionally relies on speech acoustic data as well. By processing the acoustic data to recognize the shapes, pitches, and volumes of vowels, constants, or full words, methods have been developed to identify words and phrases within a speech sample. In recent years, it has become a public concern that speech analysis systems, like

speaker identification and speech recognition, come at the cost of serious privacy risks. In other words, With improved identification capabilities comes more concerns of revealing unnecessary personal information tied to the content our speech. Alternatively, improved speech recognition also often reveals who it was that spoke the content. Appropriately, researchers have explored privacy-preserving speech recognition/transcription methods [38, 39]. Similarly, context-blind speaker identification pursues a biometric identification system that is unable to identify what was said by the speaker. The latter system would be useful for authentication systems where contextual privacy could be maintained while still allowing a user access to something. In this research, initial analysis in Section 3.5 led to the investigation of whether mmW vibrometry could provide privacy-preserving speech recognition or context-blind speaker identification. It turns out that mmW radar vibrometry holds potential in the space of context-blind speaker identification. This is expanded on in Sections 3.6 and 3.7.

### 3.2 Physiology of Human Speech Generation

The area of the throat responsible for both keeping unwanted things from entering our lungs and manipulating airflow to produce different sounds is the larynx as labelled in Fig. 3.1. The larynx spans from the beginning of the trachea up to where the esophagus meets the respiratory passage. The glottis is an encompassing term for the specific area of the larynx that contains our vocal folds. When we sing a note, we use the muscles in our larynx to position and keep tension in our vocal folds so that when air enters and exists this area of the throat, the folds will vibrate at the desired pitch and modulate the air accordingly. When we generate speech, we are quasi-periodically transforming an otherwise fairly steady airflow from our lungs up through our trachea out to our mouth using both our glottis and mouth [40]. The pitch at which we speak and some of the vowel phonemes, or sounds, we make relate

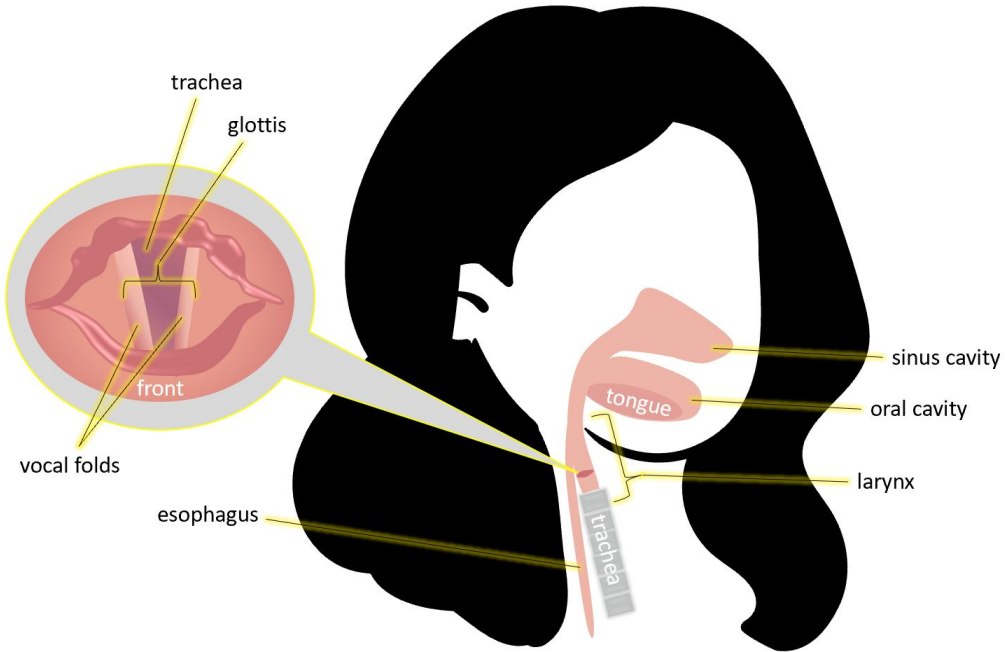


FIGURE 3.1: Diagram of human speech generation anatomy.

more directly to the way we use the muscles in our larynx to adjust our glottis. On the other hand, many consonant phonemes are primarily realized through how we modify our mouth during speech. If you try saying “pay” versus “lay”, you may notice that your tongue and lips are really what create their acoustic distinctions.

Regardless, mmW radar vibrometry in this context will measure the vibrations of a person’s skin surrounding their larynx as the radar waveform will not penetrate through the tissue to reach their actual vocal folds/glottis (see Section 2.2). Anatomically, not all points on the skin surrounding the larynx provide equally glottal-correlated vibrations. [41] showed that the largest magnitude of acceleration during speech generation on the throat tends to be in the immediate vicinity of larynx. In this chapter, we therefore assume that mmW radar vibrometry observations consists of backscatter from points on where the skin is directly surrounding the larynx. We also assum these measurements are in line-of-sight of the radar and not shadowed by other parts of the body. If the larynx is hidden by other body parts or

particularly thick clothing, greater mmW attenuation is expected and may result in too low of SNR for useful mmW radar vibrometry.

### 3.3 System Setup

In this work, larynx motions were captured with a Texas Instrument 77 GHz FMCW multiple-input-multiple-output (MIMO) radar with 3 transmit and 6 receive channels. Experiments were conducted at less than a meter away as to provide ideal levels of SNR. In addition to radar vibrometry, experiments included collecting microphone and laser Doppler vibrometer (LDV) data while word and phrase utterances were produced by both human subjects and a loudspeaker source. Short-time Fourier transform (STFT) spectrograms were used to compare these different sources and modalities.

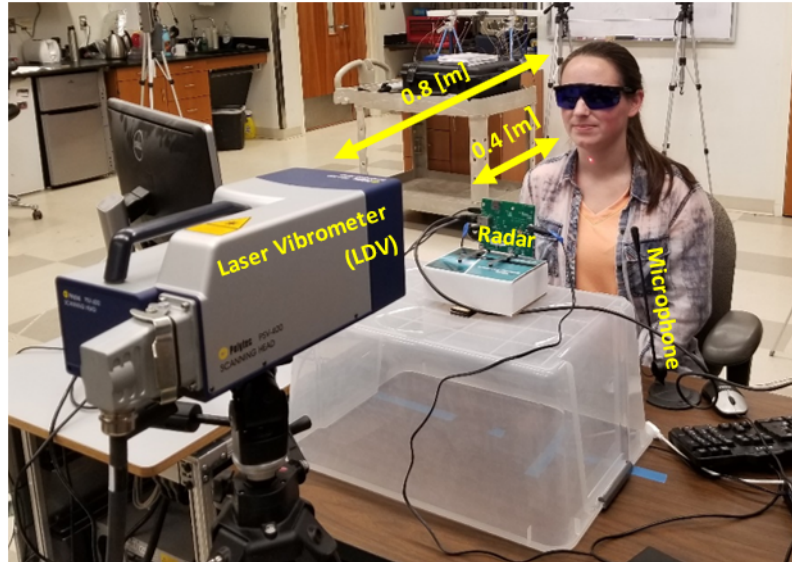


FIGURE 3.2: Experimental setup with a human speech source.

The Polytec PSV-400 LDV was used to produce a set of ground truth vibrometry data. The microphone was used so that a comparison of vibrometry data to acoustic data could be conducted to help inform its usefulness in pursuits such as speaker

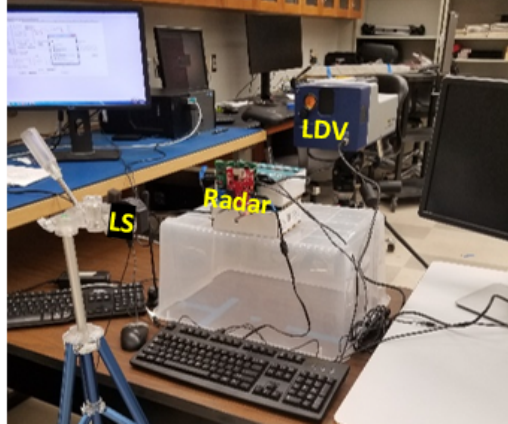


FIGURE 3.3: Experimental setup with a loudspeaker speech source.

identification or speech recognition. Due to the lack of available human subjects, the loudspeaker source was used to provide a larger best-case vibrometry data set when needed. Fig. 3.2 shows the setup for vibrometry and microphone collections from a human speaker, while Fig. 3.3 shows the setup for the loudspeaker collections. No microphone was used for the loudspeaker collection as the audio files played over the loudspeaker could themselves be used for the acoustic data.

### 3.4 TIMIT Database

In investigating mmW radar vibrometry's capabilities in human speech analysis, the TIMIT Acoustic-Phonetic Continuous Speech Corpus was used to source a loudspeaker on occasions where a large set of vibrometry data was needed. Authentic human vibrometry was less available, and so the TIMIT data played over a loudspeaker was able to provide a synthetic vibrometry data set (see setup in Fig. 3.3).

The TIMIT database was designed to provide speech data for acoustic-phonetic studies and for the development and evaluation of speech-driven systems. The speech data is sampled at a rate of 16 kHz, and the sentence lengths of both the training and testing data subsets can be seen in the histograms shown in Fig. 3.4.

The distribution of the set's 630 speakers by dialect and gender are also shown in

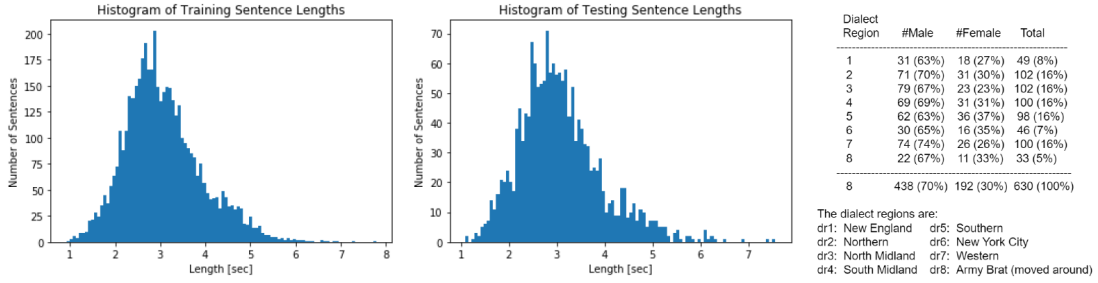


FIGURE 3.4: Statistical graphics and table of TIMIT database characteristics.

Fig. 3.4. The TIMIT database comes predivided into training and testing subsets, however this speech was combined and re-divided into different training and testing subsets for this project because the original divide has no human speakers with data in both the training and testing subsets, which serves as inadequate when training a speaker ID network. Since each speaker contributes 10 sentences to the database, 7 sentences per speaker were separated into training and 3 were left as testing sentences.

More details on the TIMIT dataset can be found at [42].

### 3.5 Processing Chain for mmW Radar Vibrometry Speech Visualization

The processing chain shown in Fig. 3.5 shows how the de-chirped IQ data is transformed into a spectrogram comparable to an audio spectrogram.

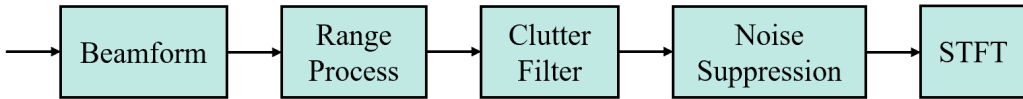


FIGURE 3.5: Processing chain for generating mmW radar vibrometry spectrograms.

Conventional beamforming on the data is done first, followed by range processing which consists of taking a DFT in fast time and selecting the range bin of interest. Next, clutter filtering is done with a notch filter at 0 Hz Doppler to eliminate return

from stationary objects. Starting from Equation 2.12, this gives

$$y(t) = \sum_{n=0}^N w_n \sum_{k=1}^K \tilde{\alpha}_k e^{j \frac{4\pi}{\lambda_0} d_k (t + nT_{\text{PRI}})} + \tilde{n}(t) \quad (3.1)$$

where  $d_k(t)$  is the larynx displacement at point  $k$  over time,  $N$  is the order of the clutter filter, and  $w_n$  is the filter coefficient for the  $n^{\text{th}}$  tap. If at a particular time interval, a sum of harmonic tones is assumed to be sourcing the larynx vibrations, as is common in speech, the displacement can be modeled as

$$d_k(t) = \sum_{g=1}^G \gamma_{g,k} \sin(2\pi g f_1 t) \quad (3.2)$$

where  $G$  is the number of harmonics being modeled,  $\gamma_g$  is the amplitude of in meters of the  $g^{\text{th}}$  harmonic's displacement, and  $f_1$  is the fundamental frequency.

When no clutter filter has been used ( $w_0 = 1$  and  $w_n = 0$  for  $n \neq 0$ ) and we approximate larynx displacements to their first harmonic ( $G = 1$ ), equation 3.1 results in a sum of Bessel function amplitudes at harmonic frequencies for each point return in the frequency domain,

$$Y(f) = \sum_{k=1}^K \sum_{l=0}^{\infty} \tilde{\alpha}_k J_l \left( \frac{4\pi \gamma_{1,k}}{\lambda_0} \right) \delta(f - l f_1) + \tilde{N}(f) \quad (3.3)$$

Here,  $J_l$  is the  $l^{\text{th}}$  order Bessel function of the first kind, and  $\delta(\cdot)$  is the dirac delta function. If more harmonics are modeled for the larynx displacement, the frequency domain result would be a convolution of a sum of Bessel function amplitudes at harmonic frequencies. If we do not assume that only the first harmonic is present ( $G \neq 1$ ), then  $Y(f)$  will be the convolution of multiple terms similar to Equation 3.3 since the sum of terms in an exponential results in the multiplication of exponentials with the separate phase terms. The Fourier transform of multiplication then provides convolution.

The DC content, or 0 Hz content, from 3.3 that would be removed by a good clutter filter is  $\sum_{k=1}^K \tilde{\alpha}_k J_0\left(\frac{4\pi\gamma_{1,k}}{\lambda_0}\right)$ . It can easily be seen in Fig. 3.6 that when  $\gamma_{g,k}$ 's are small, most of the power due to the vibrations are removed by the clutter filter.

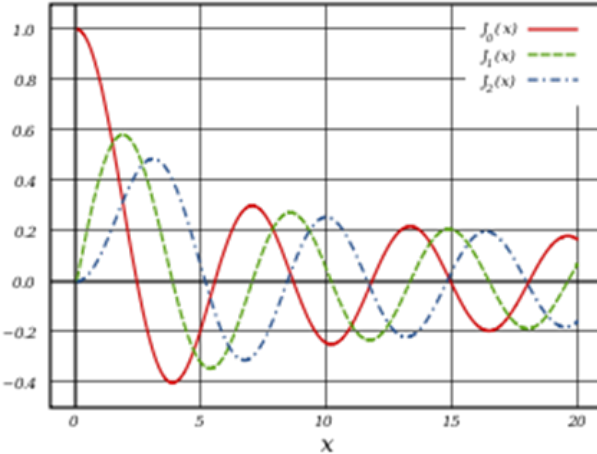


FIGURE 3.6: Plots of the  $0 - 2^{\text{th}}$  order Bessel functions of the first kind.

For a radar wavelength of 3.9 mm,  $\gamma \in \{0.75 \text{ mm}, 1.72 \text{ mm}, 2.69 \text{ mm}, 3.66 \text{ mm}, \dots\}$  proves to be preferable as they lead to the DC component of the vibrational return being zero. In practice, however, the amplitude of the human larynx vibrations cannot be controlled this precisely and thus a significant fraction of vibrational signal is likely lost due to clutter filtering.

For noise suppression as seen in Fig. 3.5, an adaptive line enhancer (ALE) using the recursive least squares (RLS) algorithm with 50 taps and a delay,  $\Delta$ , of 10 is used. Choice in the delay was chosen somewhat empirically, though it was purposely

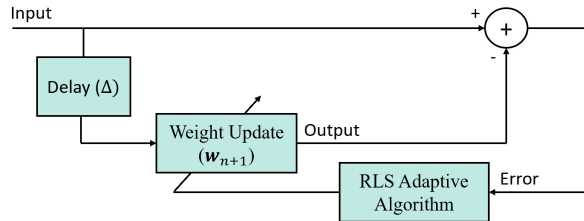


FIGURE 3.7: Adaptive line enhancer noise suppression processing chain.

kept shorter than expected phoneme duration. It is reasonable to estimate that phonemes have a duration on the order of tens of milliseconds. If we consider our own speech, this seems like a reasonable estimate as words can often be spoke in less than a second and words typically consists of at least a few phonemes. When the slow-time signal being processed is sampled at pulse repetition intervals (PRIs) between 2 kHz and 16 kHz, 10 samples, or 1 – 5 ms, presents itself as a reasonable delay for the ALE algorithm. The number of taps was also empirically chosen.

Following conventional speech processing spectrogram methods, a short-time Fourier transform (STFT) is used to generate the final visual. An STFT is simply the spectrum of a signal over time. This can be understood as using a sliding window to observe a portion of the signal, taking its Fourier Transform, indexing that spectrum by the current time, and then sliding the window to the next portion of the signal to repeat the process. The STFT parameters used are a Taylor window with a length of 20 ms and an overlap of 70%. The choices in window length and overlap stem from the expected variation in human speech. The 20 ms window is both short enough that any single frame will typically contain data from only one phoneme, yet it is also long enough that it will include at least two periods of voiced speech’s fundamental frequency, assuming that the lowest pitch is around 100 Hz.

To exemplify the spectrograms produced by this chain, see Fig. 3.8 for a sample of the data collected in the setup shown in Fig. 3.2 for a female speaker saying “She had your dark suit in greasy wash water all year.” This sentence is arbitrary yet phoneme-rich. It was chosen due to its use in the TIMIT data set that was used later on in this chapter.

Our results confirmed that microphone measurements of sound, which are acoustic pressure fluctuations, are similar yet more informative than the measurements of the surface vibrations that produce the sound. From both visual observation in Fig. 3.8 and audible observation, it is clear that the acoustic data contains stronger

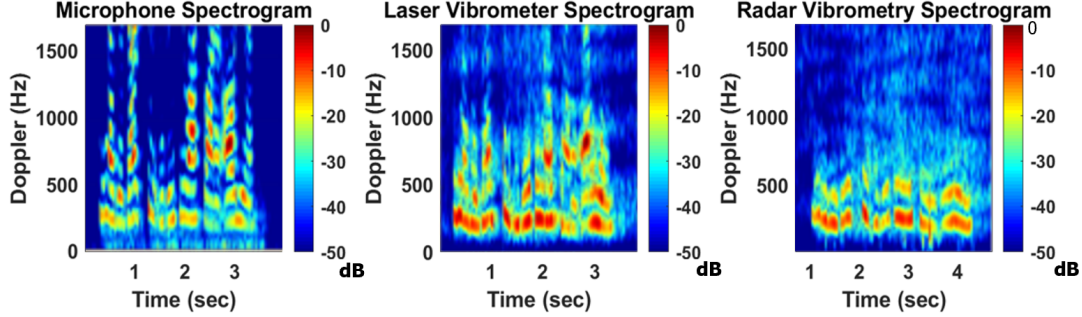


FIGURE 3.8: Radar parameters include PRF = 4 kHz,  $f_0 = 77$  GHz, and  $B = 4$  GHz.

higher harmonics from speech. It is evident that the spectrograms produced from mmW radar compare favorably with microphone data in capturing the first two harmonics of speech with frequency content below 1000 Hz. This likely relates to the fact that the higher frequency content is subject to more attenuation as the glottal vibrations propagate through the tissues in the human throat. Moreover, mmW radar and laser Doppler vibrometry were very comparable in frequency content with signal-to-noise ratios differences that were less than 10 dB. This is an encouraging finding since the cost of our low-power-aperture product mmW radar is approximately 100 times less than an LDV.

### 3.6 Speaker Identification

In this work, a speaker ID classifier inspired by [43], [44], and [45] was developed. Variations in parameters and network architecture choices were explored including the format of the input data (an acoustic time series vs Mel scale-based features vs spectrograms), the number of convolutional and linear layers, kernel sizes and step sizes, batch size, learning rate, activation functions, gradient and momentum algorithms used, length of input signals, and loss function.

The goal was not to develop the best speaker identification network. Rather, a sufficiently good speaker ID network was required to allow for the model to be

trained on whatever source variation of data was considered, such as acoustic data, LDV data, or mmW radar vibrometry data, thus allowing for a comparison between the different sets for speaker ID. The resulting network demonstrated performances up to 92% testing accuracy on a 20 speaker subset and 82% testing accuracy on a 100 speaker subset for acoustic data. This speaker identification network is described in Fig. 3.9.

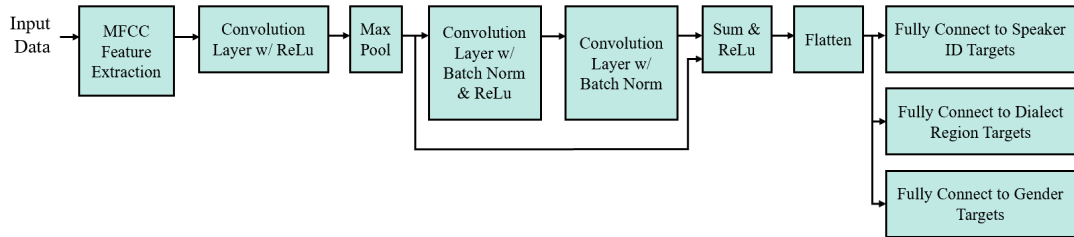


FIGURE 3.9: Network architecture for the speaker identification CNN classifier.

Mel scale-based features are commonly used in speech processing. They leverage the Mel scale which was originally derived to measure the subjective pitch of speech. The Mel scale is known to scale frequency bands proportionally to the perceived magnitude of the pitch according to the human ear’s hearing abilities. In this classifier, an STFT in the Mel scale is calculated in the first processing block of Fig. 3.9. The Python library known as Librosa is used to perform these transformations. Specified parameters of this method include a filterbank of length 64, a window length of 20 ms, and 95% overlap. The first convolutional layer then has a  $5 \times 5$  kernel size with a stride of 2. The max pool kernel size is  $2 \times 2$ . The second and third convolutional layers have a kernel size of  $3 \times 3$  and stride of 1. The batch size used in this classifier is 5, and the learning rate is set at 0.005. Stochastic gradient descent with Nesterov momentum was also used. Nesterov momentum involves calculating the decaying moving average of the gradients of projected positions in the search space. This allows the gradient descent process to avoid missing or overshooting minima by quantifying the acceleration of the descent and using it to better inform

when descent needs to maintain larger step sizes versus slowing them down to avoid overshooting. The data used in this network was clipped in time to all be 1 second in length.

The final blocks in Fig. 3.9 demonstrate how multi-task learning is completed in this network. The full model’s loss function is

$$\text{loss}_{\text{full}} = 0.8\text{loss}_{\text{Speaker ID}} + 0.1\text{loss}_{\text{Dialect Region}} + 0.1\text{loss}_{\text{Gender}}. \quad (3.4)$$

Multi-task learning, or the act of using multiple classification targets to train a model for one task, has been demonstrated both theoretically and empirically to greatly improve classification performance on the tasks over learning each task independently when there exists relations between the tasks [46]. This is especially relevant when data is limited, which is the case in the TIMIT dataset for speaker identification, as only ten sentence utterances per speaker are available. This is even more relevant for radar vibrometry data due to the scarcity of people available to sit down and offer vibrometry data for multiple observations. Because the TIMIT database provides related targets of speaker gender and dialect region in addition to speaker identity, multi-task learning proved to be particularly useful in training our speaker identification network.

Since initial analysis demonstrated that vibrometry data appeared as a low-pass version of its acoustic counterpart, low-pass filtered acoustic data from the TIMIT data set was tested in our speaker identification classifier, see Fig. 3.10. In reference to Fig. 3.8, where the cutoff of frequency for LDV vibrometry data is approximately 1 kHz, performance drops from the previously achieved 92% to about 58%. For an even lower cutoff frequency with mmW radar vibrometry, a performance drop to 50% seems likely.

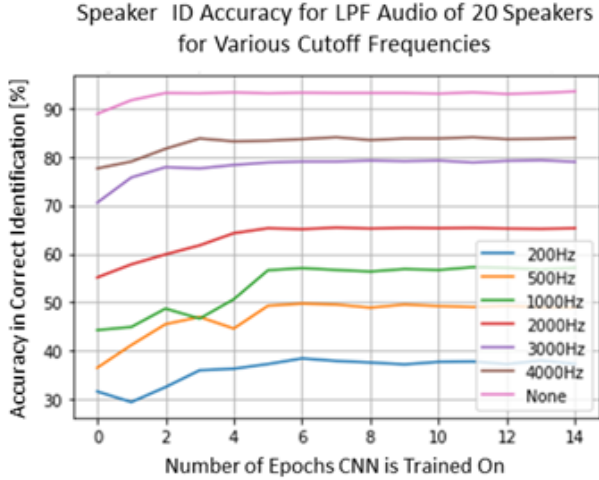


FIGURE 3.10: Speaker ID performance for various LPF Cutoff Frequencies for a 20 speaker set.

### 3.7 Speech Recognition

In this work, Google Speech Recognition [47] was used as an automatic speech recognition (ASR) system. A new ASR model was not developed and trained like was done for speaker identification because ASR training requires having a sufficiently large set of utterances of the same words for training, and the TIMIT database simply does not satisfy this requirement.

Using an already trained model like Google Speech Recognition inherently has benefits as well as downfalls. The benefits include that it performs very well on the type of data it expects - acoustic data. Additionally, pre-trained models are fairly easy and quick to implement. The downfalls, in this case at least, are that the model cannot be retrained. This means the model itself cannot be trained on vibrometry data for example. Furthermore, even when the pre-trained model has been trained on the type of data being used like acoustic data, if the data has been filtered, results will only provide an idea of how traditional ASRs will perform with that data. It is not necessarily true that an ASR trained on filtered acoustic data would perform equivalently. Assuming an acoustically trained model, speech recognition

performance on filtered acoustic data should instead be considered a lower bound as an ASR trained on filtered acoustic data instead should only be able to perform better.

The limited frequency content of mmW radar larynx vibrometry (10 to 1000 Hz) motivated the investigation of what bands of frequency contribute most to both speaker identification and ASR. Fig. 3.11 shows the performance of speaker ID and ASR as the audio begins from including minimal low frequency content and increases to include higher frequency content when looking from left to right. Fig. 3.12, however, shows the performance of speaker ID and ASR as the audio begins from including all frequency content and filters more low frequency content when looking from left to right.

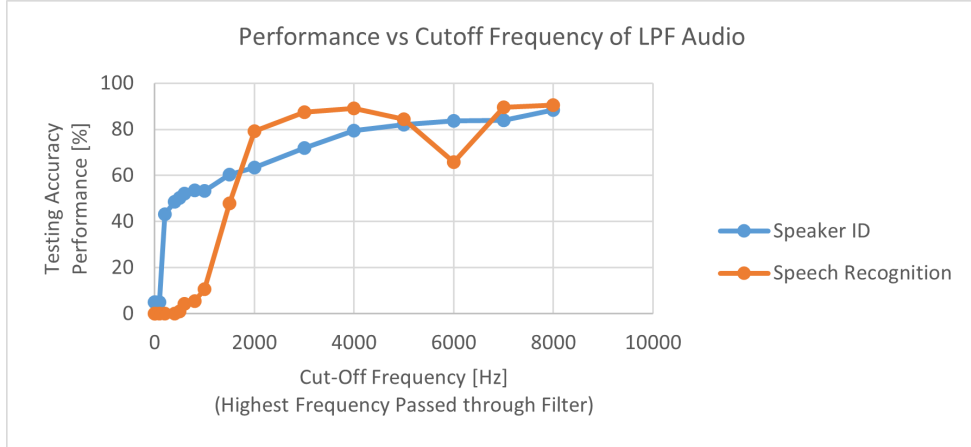


FIGURE 3.11: Low-pass filtered speaker ID and ASR performance for various LPF Cutoff Frequencies for a 20 speaker set.

The low-pass filtered (LPF) audio results suggest that a minimum low-pass cutoff frequency of 2 kHz is vital for speech recognition. In contrast, speaker identification can be performed using cut-off frequencies well below 2 kHz with greater accuracy as more bandwidth is available. Between both figures, it appears as though the information in the first harmonic contributes greatly to speaker identification but may not be entirely unique information. This is understood by considering the

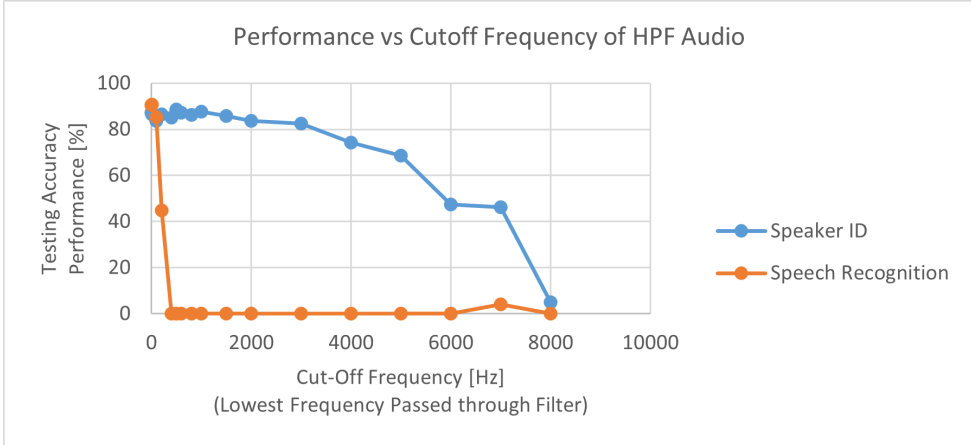


FIGURE 3.12: High-pass filtered speaker ID and ASR performance for various HPF Cutoff Frequencies for a 20 speaker set.

HPF results. When the first harmonic is filtered out, speaker identification still manages to perform fairly well. ASR performance, on the other hand, appears to truly suffer when this is the case. Likely, this phenomena corresponds to Google’s ASR containing a voice activity detection block at the forefront of its processing to enable efficient detection. Voice activity detection is often completed by detecting the presence of the first harmonic of speech, which typically falls between 100 and 400 Hz. If the ASR does not detect the first harmonic, like when a HPF is used to only filter out content below 500 Hz, then speech recognition may not even be attempted. In reality however, a person can make out speech when this first harmonic is filtered out, suggesting that an ASR system could be developed for high-pass filtered speech. This supports the previous argument that ASR results in this project should be considered a lower bound for speech recognition capabilities.

In relation to observed vibrometry data, better speaker identification could be expected versus speech recognition since vibrometry data appears to be a low-pass filtered variant of acoustic data. This favors the application of content-blind speaker identification for vibrometry data. Unfortunately, collecting radar vibrometry from a large number of individuals was beyond the scope of this project, so the vibrometry

from the loudspeaker playing clips of the TIMIT database were used instead. For these experiments, the audio was played at a volume similar to normal human speech, and the same 20 speaker TIMIT subset that has been used throughout this chapter was used for this loudspeaker vibrometry data collection. Performance results for audio, low-pass filtered (LPF) audio, and loudspeaker (LS) vibrometry can be seen in Table 3.1.

Table 3.1: Speaker ID and ASR Performance Across Data Types

Data Type	Speaker ID	Speech Recognition
Audio Data	88%	90%
LPF Audio Data	53%	11%
mmW Radar Loudspeaker Vibrometry	40%	N/A

The low-pass filtered audio's cutoff frequency of 1 kHz was chosen to match the observed cutoff frequency seen in vibrometry data. It stands to reason that since human mmW radar vibrometry has a similar cutoff frequency, that it can represent anticipated performance for human larynx vibration speaker ID and ASR. Due to the program's data restrictions, the vibrometry data was required to be kept on a private network that was unable to run Google Speech Recognition, so ASR on the vibrometry data was left untested.

Though results thus far supported the theory that content-blind speaker identification may be possible with larynx vibrometry data, the full analysis was left incomplete. To truly justify mmW radar vibrometry on human larynx during speech generation for content-blind speaker identification,

1. a full mmW radar vibrometry data set of larynx movement for multiple speakers saying multiple word utterances multiple times needs to be collected and
2. an ASR architecture needs be found or developed that can then be trained on the type of data for which it will be evaluated on.

This project, however, sparked a curiosity into how feasible a system could be that makes use of an artificial vibration for the purpose of wireless communication.

# 4

## Vibrational Radar Backscatter Communication (VRBC) Systems

### 4.1 Motivation for VRBC

Traditionally, backscatter communication is exemplified in RF identification (RFID), which operates at UHF frequencies. Thanks to advances in the autonomous vehicle industry, mmW radars have become inexpensive and more widely available leading researchers to consider backscatter communication at mmW for tagging and internet-of-things (IoT) applications [48, 49]. To achieve adequate signal returns, backscatter communication solutions at mmW frequencies tend to require complex and expensive retro-directive antenna arrays (antenna arrays that are able to direct reflected energy back towards the direction it came from) [50, 51].

To achieve the benefits of quasi-passive backscatter communications [52] without the complexity of a mmW transponder antenna array, we introduce a system that uses a mmW radar as a vibrometer. In contrast to traditional backscatter communication systems, VRBC uses the radar to observe small vibrational displacements on the surface of a transponder, thus avoiding the challenge of requiring a matched

antenna that also has a radar cross section (RCS) that provides adequate backscatter strength. Additionally, instead of the backscatter modulation appearing as a change in amplitude due to a change in transponder impedance, VRBC modulation comes in the form of phase modulation caused by changes in a vibrating surface's displacement. The vibrational transponder itself can be as simple as a loudspeaker, whose diaphragm is the vibrating surface, or a more optimally designed active transponder with a controllable surface displacement. Regardless, the modulation appears primarily in the backscatter's slow-time phase when the radar's waveform is that of a traditional frequency modulated continuous wave (FMCW) radar.

Vibrometry at mmW has been used in other applications such as structural analysis [53], acoustic signal reconstruction [54], wireless communication across medium boundaries [55], and search and rescue operation [56]. With the installation of mmW radar technology in modern vehicles becoming commonplace, anything-to-vehicle communication naturally fits as an additional application space for mmW vibrometry as it offers a way to increase vehicle situational awareness while requiring minimal additional infrastructure.

Communication to and from vehicles has historically required either sharing resources with radar systems or optimizing waveforms that can be used for both sensing and communications. The former method, often described as the cohabitation of radar and communication systems, typically requires cooperative sensing techniques to reactively mitigate mutual interference [57–59]. A novel radar estimation information rate was described in [60] to help quantify how to balance power between the two operations. Alternatively, joint radar and communication co-design waveforms allow a single active RF emission to act as the radar waveform while also containing modulation for a communication signal [61, 62]. Solutions of this nature tend to include waveform designs that inherit primary characteristics from one of the two systems' traditional waveforms. Of particular interest in applications

such as connected vehicles are radar waveform-based designs where communication functions are integrated into an existing radar system by modifying the waveform to include digitally modulated data symbols [63, 64]. Both cohabitation and co-design solutions demonstrate some amount of tradeoff between sensing and communication performance capabilities. Because VRBC allows messages to exist within the phase of backscatter, it provides a way in which sensing and communications can be done simultaneously with no modification to the standard radar waveform being used.

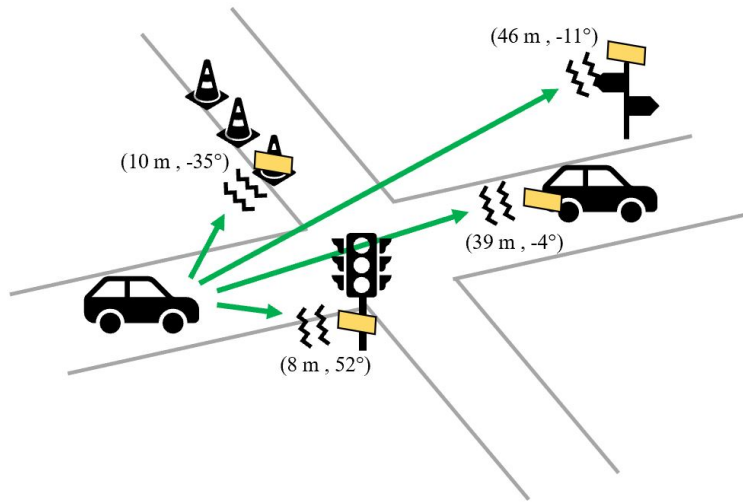


FIGURE 4.1: An X2V scenario demonstrating the simultaneous multichannel signal reception of VRBC to the mmW radar-equipped left-most vehicle.

VRBC provides the additional benefit of offering numerous communication channels. Traditional anything-to-vehicle communication methods have a limited number of channels constrained by the system's total bandwidth. In VRBC, the number of communication channels available to a particular vehicle scales with the range and bearing resolution of the automotive radar, as illustrated in Fig. 4.1. In the illustration, the green arrows indicate paths along which the radar signal travels and reflects from targets back to the on-vehicle radar. Vibrational transponding surfaces are in yellow and characteristic to particular, yet arbitrary bearing angles and ranges in re-

lation to the receiving vehicle. Accordingly, VRBC could serve as a beneficial add-on particularly in high traffic scenarios to alleviate network congestion for line-of-sight anything-to-vehicle communication [65].

## 4.2 Description of VRBC Data Acquisition

In Chapter 5, desirable characteristics of a messaging scheme and transponding surface for VRBC will be described. In this chapter, real VRBC data is used to demonstrate system capabilities alongside simulation results when larger amounts of VRBC data are desired. The associated transponder, radar parameters, and messaging choices used in the real data collection, however, are arbitrary though not entirely naive to favorable system characteristics. Real system optimization has not yet been attempted as the initial VRBC acquisition setup consisted of convenient components. The VRBC setup used includes the aforementioned TI IWR1443 mmW radar and a transponder made of an aluminum sheet (12 in.  $\times$  12 in.  $\times$  0.04 in. thick) whose vibrational displacements are sourced by an attachable Dayton Audio DAEX25 Audio Exciter. The exciter is fixed in the center of the plate, and the plate is left free from other boundary conditions as the whole transponder is held up via the exciter. Fig. 4.2 shows the setup in which the transponder is approximately 5 meters away and radar-facing.

Because the transponder surface is a thin square plate excited from the center, an approximate analytical expression for calculating the surface's natural resonant frequencies can be obtained using the work from [66]. For those familiar with Chladni plate demonstrations, the freely vibrating square plate may feel familiar as it is a commonly used surface for “visualizing” sound. In Chladni plate demonstrations, however, the plate is usually oriented horizontally with sand on top, thus allowing the vibrations of the plate to push the sand into a pattern revealing resonant frequency modes' nodes and anti-nodes.



FIGURE 4.2: VRBC setup looking from the mmW radar to the transponder.

The equation

$$f_{m,n} = \frac{2\pi h}{a^2\sqrt{12}} \left( \frac{Eu_{m,n}}{\rho(1-r^2)} \right)^{\frac{1}{2}} \quad (4.1)$$

describes the natural resonant frequency for a thin square free plate with  $m$  and  $n$  describing the vibration modes. Mode variable  $m$  denotes the number of modes running parallel to the long axis and  $n$  the number in the perpendicular direction. For a square plate, these are interchangeable. In Equation 4.1,  $h$  is the thickness of the plate in inches,  $a$  is half the length of the square plate in inches, and  $E$  is Young's modulus describing the material's ability to stretch and deform. Young's modulus for aluminum is about  $10 \times 10^6 \frac{\text{lb}}{\text{in}^2}$ . The variable  $r$  in this equation is Poisson's ratio, which is approximately 0.334 for aluminum. Additionally,  $\rho$  is the density of the surface material, which is  $2.588 \times 10^{-4} \frac{\text{lb sec}^2}{\text{in}^4}$ . The final term in Equation 4.1,  $u_{m,n}$ , is mathematically provided in [66] and relates to the strain energy of the vibrating plate which requires solving the scenario's boundary conditions. For reference, Table 4.2 provides the calculated resonant frequencies for all even mode combinations of the

aluminum plate for  $m$  and  $n < 5$ .

Table 4.1: Square Foot Aluminum Plate Resonant Frequencies

Mode Parameter 1 (m)	Mode Parameter 2 (n)	Frequency [Hz]
0	2	59.5
2	2	175.8
0	4	321.8
2	4	447.3
4	4	763.5

Due to the location of the exciter being centered on the square surface, only even modes are considered as they are the only ones that provide symmetric displacements. Higher  $m$  and  $n$  values are also not considered because higher modes lead to smaller displacements of the plate's anti-nodes which results in lower SNR for use in mmW vibrometry applications. Fig. 4.3 shows a few of the modes of interest for visual reference. Anti-nodes are defined as the locations of maximum displacement and can be seen in purple and orange. Alternatively, nodes are locations on the plate where the displacement remains stationary as the plate vibrates. Nodes are located where the light blue color meets the green.

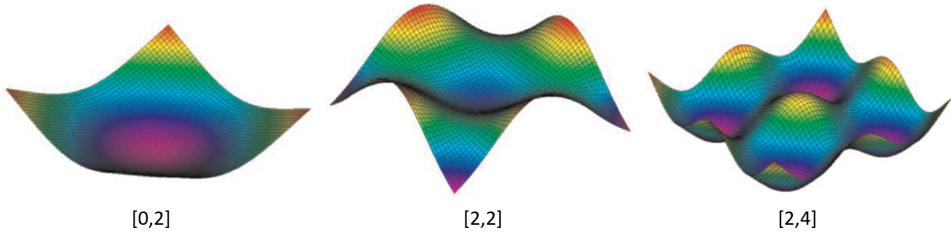


FIGURE 4.3: Obtained from [66].

For verification, a laser Doppler vibrometer (LDV) was used to measure the maximum displacements at the center of the plate and corner over a range of frequencies from 50 Hz to 1 kHz. Fig. 4.4 shows the results and includes vertical lines at the expected resonant frequencies in accordance with Table 4.2. Despite the analytical

expression assuming ideal conditions, such as a perfectly centered source, perfectly flat and accurate plate specifications, and negligible effects due to gravity, the calculated frequencies still match very closely with measured resonant frequencies.

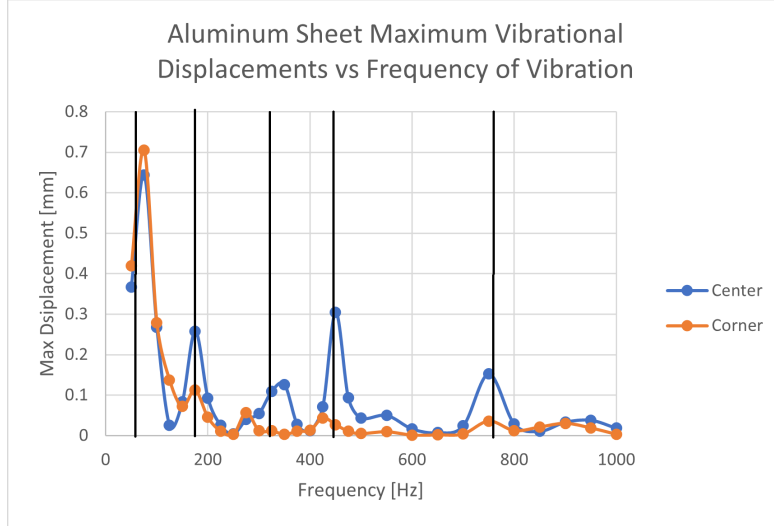


FIGURE 4.4: LDV measured maximum displacements at the center and corner of the square foot aluminum transponder versus excitation frequency.

### 4.3 VRBC Signal Model

To detail a successful VRBC system, we begin formally defining VRBC signals by assuming an FMCW radar transmit signal, as presented in Equation 2.1. Since only the return containing the target is desired for the purposes of VRBC, we continue under the assumption that the full return is only from the beam in the direction of the target. When a beam output contains only a single vibrating target transponder, the received signal consists of the backscatter of the transmitted signal from the vibrating transponder,  $s_{\text{RX}_{\text{tar}}}(t)$ ; clutter,  $s_{\text{RX}_{\text{clt}}}(t)$ ; and additive white Gaussian noise (AWGN),  $\tilde{n}(t)$ :

$$s_{\text{RX}}(t) = s_{\text{RX}_{\text{tar}}}(t) + s_{\text{RX}_{\text{clt}}}(t) + \tilde{n}(t). \quad (4.2)$$

The return from the target is modeled as a flat fading surface

$$s_{\text{RX}_{\text{tar}}}(t) = \tilde{\alpha}_{\text{tar}} e^{j2\pi f_0(t-\tau_{\text{tar}}(t))} \sum_{g=0}^{G-1} u_p(t - \tau_{\text{tar}}(t) - gT_{\text{PRI}}), \quad (4.3)$$

where  $\tau_{\text{tar}}(t)$  is the round trip delay observed due to the range from the radar to the target. This models the cases of surface backscatter where the surface roughness is much less than the range resolution of the radar as well as the case of retro-directive reflectors. In the anything-to-vehicle communication scenario, the former case is exemplified when the transponder is a traffic sign or license plate at ranges greater than a few meters.

If we assume the radar and target move at some bulk velocity such as when the radar is on a moving vehicle or the vibrational surface is mounted on another moving vehicle, we can write the delay as

$$\tau_{\text{tar}}(t) = \frac{2}{c}(r_{\text{tar}} + v_{\text{tar}}t - v_{\text{radar}}t + d(t)). \quad (4.4)$$

The term  $r_{\text{tar}}$  is the initial range between the transponder target and VRBC radar,  $v_{\text{tar}}$  is the radial velocity of the target,  $v_{\text{radar}}$  is the radial velocity of the radar, and  $d(t)$  is the transponder's radial surface displacement. Here, we assume radar-facing surfaces so that that object's radial displacement remains significant. A more retro-directive transponder is desirable and poses an interesting area of future research. This model, however, does not require a specific transponder design and only assumes a system in which adequate radial surface displacement is present. Equation 4.4 has also been written assuming that positive radial velocities are in the direction forward from the perspective of the radar.

In Equation 4.3,  $\tilde{\alpha}_{\text{tar}}$  is the amplitude after scaling due to signal propagation as a function of the target's range and radar cross section (RCS). The tilde indicates that this term is complex. Specifically, all  $\tilde{\alpha}$  terms going forward are complex Gaus-

sian random variables following the Swerling model [67]. Details of the statistical characteristics of these terms can be found in Chapter 2.

The target-directed clutter return within a beam can be modeled as a sum of  $K$  point scatterers

$$s_{\text{RX}_{clt}}(t) = \sum_{k=1}^K \tilde{\alpha}_k e^{j2\pi f_0(t-\tau_k(t))} \sum_{g=0}^{G-1} u_p(t - \tau_k(t) - gT_{\text{PRI}}). \quad (4.5)$$

Each clutter point indexed by  $k$  has delay

$$\tau_k(t) = \frac{2}{c}(r_k - v_{\text{radar},k}t), \quad (4.6)$$

where  $r_k$  is the range of the  $k^{\text{th}}$  clutter point, while  $v_{\text{radar},k}$  is the radial velocity of the radar with respect to the  $k^{\text{th}}$  clutter point. The radial velocity relates to the absolute velocity and azimuthal angle  $\theta_k$  measured from the direct of motion of the point via  $v_{\text{radar},k} = v_{\text{radar},k}^{(\text{abs})} \cos \theta_k$ . Because this return contains clutter points from the full beam, there exists multiple clutter points for which their ranges are equal but their complex amplitudes and radial velocities for the radar differ. This subset of points represents the clutter along the arc that spans the beamwidth of the radar at a particular range. The Doppler spread due to the radar's absolute motion can then be calculated using

$$\Delta f_D = \frac{2}{\lambda_0} v_{\text{radar}}^{(\text{abs})} \Delta \cos \theta_k, \quad (4.7)$$

where  $\Delta \cos \theta_k$  denotes the difference in  $\cos \theta$  due to the edge points of the beamwidth of the radar.

Following conventional FMCW processing methods, the entire beam return in Equation 4.2 is first de-chirped by multiplying the received signal by the complex

conjugate of the transmitted,

$$s_{\text{TX}}(t)s_{\text{RX}}^*(t) = \tilde{\alpha}_{\text{tar}} e^{j2\pi f_0 \tau_{\text{tar}}(t)} \sum_{g=0}^{G-1} z_{\text{tar}}(t - gT_{\text{PRI}}) + \sum_{k=1}^K \tilde{\alpha}_k e^{j2\pi f_0 \tau_k(t)} \sum_{g=0}^{G-1} z_k(t - gT_{\text{PRI}}) + \tilde{n}(t) \quad (4.8)$$

where

$$z_{\text{obj}}(t) = \begin{cases} e^{j\pi\beta(2\tau_{\text{obj}}(t)t - \tau_{\text{obj}}^2(t))} & \tau_{\text{obj}}(t) \leq t < T \\ 0 & \text{otherwise} \end{cases} \quad (4.9)$$

In conventional radar processing,  $\tau_{\text{obj}}(t)$  is usually considered constant within a chirp, ie. not a function of time within  $z_{\text{obj}}(t)$ . In such cases, this simplifies  $z_{\text{obj}}(t)$  to a complex sinusoid with a frequency proportional to range. This is an assumption that VRBC cannot always make however, due to the frequencies of vibration being similar to the radar's PRF. For that reason, we continue with the generalized representation. In reference to the full processing chain shown in Fig. 4.5, Equation 4.8 is the output of the beamforming block in the target isolation sequence for an arbitrary transponder.

## 4.4 VRBC Processing Chain Details

### 4.4.1 Target Detection

To reach Equation 4.8, target detection must first be completed. Target detection typically consists of using conventional detection methods such as constant false alarm rate (CFAR) detection to find VRBC transponders in range-bearing space. This method naturally detects traditional radar targets in the scene that are not being used for VRBC in addition to VRBC transponders. To ensure that only vibrating transponders are processed through the remainder of the VRBC processing chain, the range-bearing intensity plot considered in VRBC transponder detection is

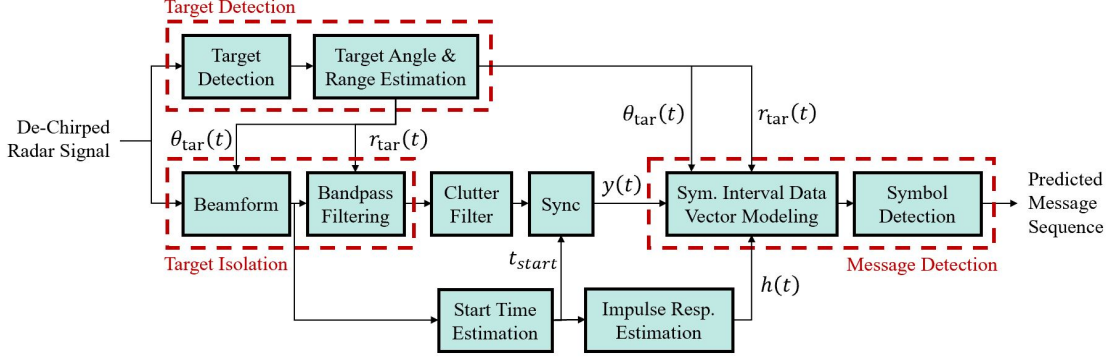


FIGURE 4.5: The processing chain used to get the message signal in a VRBC system.

constrained to exhibit the power related only to the Doppler frequencies of expected VRBC vibrations.

Consider the slow-time approximation from Equation 2.12 for the case of VRBC. Recall that the index  $m$  represents a range bin as this slow-time signal results from taking a DFT of the fast-time signals and looking across a single frequency bin from chirp to chirp. Recall also that the index  $m$  relates directly to a range via  $f_m = \frac{2\beta r_m}{c}$ , which is why we can refer to  $m$  as a range bin index. Using conventional delay-and-sum beamforming, the slow-time signal at a given range bin and look direction can be written as

$$y(t, m, \theta) \approx \tilde{\alpha}_{\text{tar}} e^{j2\pi f_0 \tau_{\text{tar}}(t, m)} + \sum_{k=1}^{K_{r_m, \theta}(t)} \tilde{\alpha}_k e^{j2\pi f_0 \tau_k(t, m)} + \tilde{n}(t). \quad (4.10)$$

The set of clutter points,  $K_{r_m, \theta}(t)$ , is therefore dependent on the location bin associated with range,  $r_m$ , and look direction,  $\theta$ . Because the DFT in fast-time provides a peak at frequencies related to the range of the targets/points in the field of view,  $\tilde{\alpha}_{\text{tar}} \approx 0$  when no target is present at a given location bin. For generating a range-bearing plot, the observed power of the slow-time signal is often used for the location bin's intensity, thus demonstrating how when targets are present the range-bearing intensity plot presents as a peak at the location bin.

To constrain detection to VRBC transponding targets, a DFT of Equation 4.10

can be taken. As shown in Chapter 2, if the vibrational displacement signal contributing to the target's delay is a pure tone, the result is a series of peaks at non-negative integer multiples of the vibration's frequency. Consider a transponder with displacement

$$d(t) = \gamma_{\text{tar}} \sin(2\pi f_{\text{tar}} t). \quad (4.11)$$

Recall that clutter and target delays still contain information about bulk velocity movement as well

$$y(t, m, \theta) = \tilde{\alpha}_{\text{tar}} e^{j \frac{4\pi}{\lambda_0} (r_m + v_{\text{tar}} t - v_{\text{radar}} t)} e^{j \frac{4\pi}{\lambda_0} d(t)} + \sum_{k=1}^{K_{rm,\theta}(t)} \tilde{\alpha}_k e^{j \frac{4\pi}{\lambda_0} (r_m - v_{\text{radar}} t)} + \tilde{n}(t). \quad (4.12)$$

The double-sided DFT of 4.12 results in

$$\begin{aligned} Y(f, m, \theta) &= \tilde{\alpha}_{\text{tar}} e^{j \frac{4\pi r_m}{\lambda_0}} \sum_{l=0}^{\infty} J_l \left( \frac{4\pi \gamma_{\text{tar}}}{\lambda_0} \right) \delta(f \pm (f_{v_{\text{tar}}} - f_{v_{\text{radar}}}) \pm l f_{\text{tar}}) \\ &\quad + \sum_{k=1}^{K_{rm,\theta}(t)} \tilde{\alpha}_k e^{j \frac{4\pi r_m}{\lambda_0}} \delta(f \pm f_{v_{\text{radar}}}) + \tilde{N}(f) \end{aligned} \quad (4.13)$$

where  $f_{v_{\text{tar}}} = \frac{2v_{\text{tar}}}{\lambda_0}$  and  $f_{v_{\text{radar}}} = \frac{2v_{\text{radar}}}{\lambda_0}$ . For small vibrational amplitudes, ie. on the scale of fractions of a wavelength, the majority of the energy induced by the vibrational displacement exists within the first few Bessel function terms,  $J_l \left( \frac{4\pi \gamma_{\text{tar}}}{\lambda_0} \right) \delta(f \pm (f_{v_{\text{tar}}} - f_{v_{\text{radar}}}) \pm l f_{\text{tar}}) \forall l \in \{0, 1, \dots, L\}$ .

Detecting VRBC transponders then requires determining whether peaks in the slow-time spectrum have sidebands at  $\pm l f_{\text{tar}}$ , revealing that the target under consideration is vibrating at VRBC frequencies. The case of  $l = 0$ , however, is not a sideband. Instead it corresponds to the main peak, which exists for non-vibrating targets as well. For that reason, the Doppler sidebands associated with low, non-zero  $l$  values become the primary indicators of VRBC vibration. As an example, consider a VRBC system where vibrational frequencies are expected to be at [200, 400, 600]

Hz. Upon finding peaks in beam-range-Doppler space, including peaks on the clutter ridge, looking at  $\pm l[200, 400, 600]$  Hz in Doppler around those points will indicate whether a point of interest is likely to be a VRBC transponder.

Observing the power at these corresponding frequencies and using that for the power measurement of the range-angle intensity (RAI) plot, therefore results in a VRBC Doppler-constrained RAI plot. When VRBC is expected to consists of multiple tonal symbols, as was described in the example, then the maximum power from the set of harmonic Doppler sidebands of interest can be obtained and used as the intensity estimate of a given range-angle bin

$$\text{RAI}_{\text{VRBC}}(m, \theta) = 10 \log_{10} \left( \max_g \sum_{l=1}^L |Y(f_{g,l}, m, \theta)| \right) \text{ dB} \quad (4.14)$$

where  $f_{g,l} = (f_{v,\text{tar}} - f_{v,\text{radar}}) \pm l f_{\text{tar},g}$  and  $g$  is used to index one of potentially many system vibration tones.

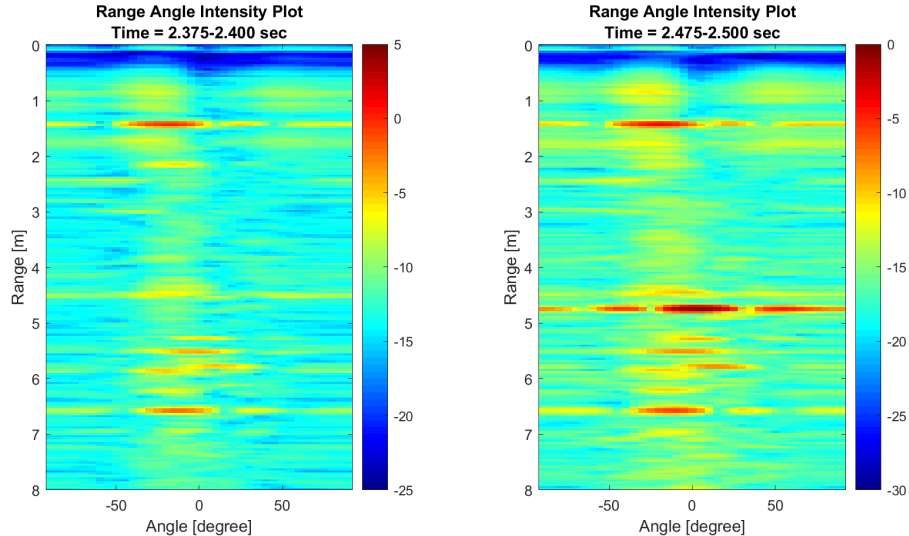


FIGURE 4.6: These plots are obtained from the setup described in 4.2 and power is in decibels.

An example of a VRBC Doppler-constrained RAI can be seen in Fig. 4.6. The left plot in the figure captures a time frame prior to the VRBC transponder vibrating,

while the right displays a time frame during VRBC sequence transmission. During the transmission, a significant peak at the transponder's range and angle appears. Though these parameters were roughly estimated prior to the experiment to be about 5 meters and at directly broadside, the data indicates that the transponder's true range and angle is closer to 4.7 meters and 5° off broadside.

Traditional CFAR detection and target tracking can then be used on VRBC Doppler-constrained RIA plots. The frame length for which RAI plots are generated does require considering how long VRBC symbols are expected to last. A frame length much longer than the symbol length could result in small VRBC-sourced sidebands when the number of symbol frequencies grows larger since the observation time will include moments of multiple symbol transmissions. Too small of frame times, however, could lead to lower SNR in the resulting Doppler-constrained RAI plots since longer observations of tones lead to sharper peaks in the frequency domain. In Fig. 4.6, the frame length used was 25 milliseconds, while the symbol length is 20 milliseconds.

#### 4.4.2 Target Isolation

The processing sub-chain labeled as target isolation in Fig. 4.5, takes as inputs both the original de-chirped data and the estimated trajectory of a given VRBC transponder,  $r_{\text{tar}}(t)$  and  $\theta(t)$ . Target isolation comprises of angular and range separation. Beamforming is conducted first using a conventional delay-and-sum beamformer assuming perfect knowledge of element spacing.

To then separate multiple users within a single beam, band-pass filtering is used to minimize the contribution of other transponders or objects contributing notable return. Signal visualizations such as the spectra shown in Fig. 4.7 can aid in deciding the appropriate bandwidth for such a filter. The filter must be designed such that it results in zero phase distortion as the vibrational displacement of VRBC appears as

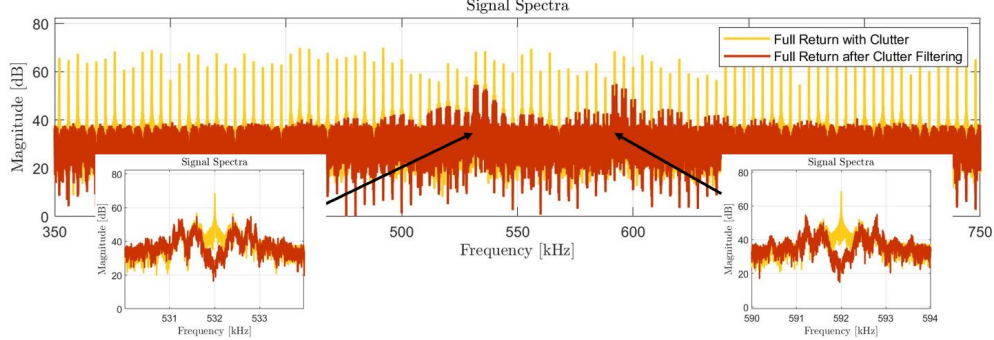


FIGURE 4.7: The spectra of a simulated VRBC beam return with two transponders at separate ranges.

a phase modulation. The filter's center frequency should be at the frequency related to the estimated range of the transponder, while the bandwidth should be an integer multiple of the PRF that is no more than the difference in frequency between that of the transponder of interest and the nearest transponder or interferer. In Fig. 4.7, for instance, the difference between two simulated transponders' peaks in frequency is 15(PRF) Hz. The bandwidth used for bandpass filtering a single transponder's response should consequently be no greater than 15(PRF) Hz and centered at the frequency associated with the transponder's estimate range. In utilizing bandpass range filtering, the AWGN assumed to be present in the full return also becomes band-limited. Band-limited noise is denoted as  $\tilde{\eta}(t)$  from here on.

$$\begin{aligned}
 y(t) = & \tilde{\alpha}_{\text{tar}} e^{j2\pi f_0 \tau_{\text{tar}}(t)} \sum_{g=0}^{G-1} z_{\text{tar}}(t - gT_{\text{PRI}}) \\
 & + \sum_{k=1}^{K_{r_{\text{BPF}}, \theta}(t)} \tilde{\alpha}_k e^{j2\pi f_0 \tau_k(t)} \sum_{g=0}^{G-1} z_k(t - gT_{\text{PRI}}) + \tilde{\eta}(t),
 \end{aligned} \tag{4.15}$$

where  $z_{\text{obj}}(t)$  was defined in 4.9 and  $K_{r_{\text{BPF}}, \theta}(t)$  describes the set of clutter points at ranges associated with frequencies passed through the bandpass filter and angle of the transponder.

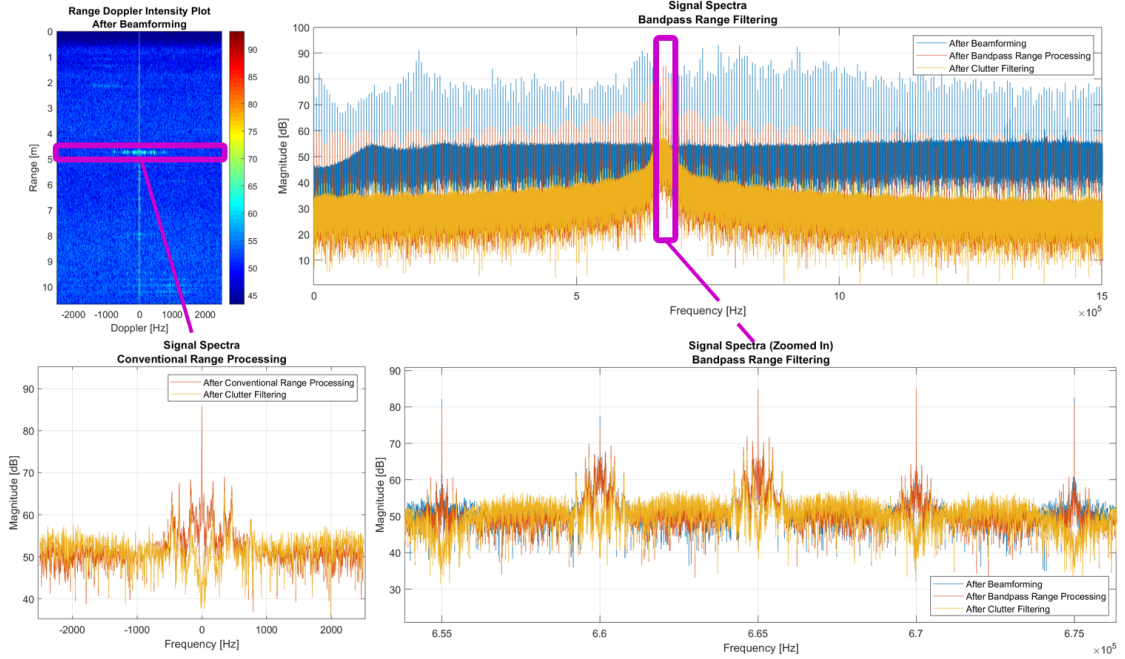


FIGURE 4.8: Symbol frequencies are 150, 350, 450, and 750, while the waveform PRF is 5 kHz and chirp bandwidth is 4 GHz.

It is important to distinguish that the presented VRBC range processing differs from traditional techniques. Traditional FMCW range processing consists of organizing the signal into a matrix of fast- and slow-time samples, or samples within a chirp versus samples across chirps, as described in Chapter 2. VRBC benefits from using the full fast-time signal in decoding due to the presence of quick phase changes caused by VRBC transponder vibrations. Here, the word ‘quick’ is relative to the duration of the waveform’s chirp.

To justify using the full de-chirped signal for detection consider both the conventional range processing method and the suggested full de-chirped bandpass range filtering method. The former produces a signal of the form shown in Equation 4.12. The latter follows Equation 4.8. Fig. 4.8 shows a real example of the two range processes’ resulting spectra. In conventional range processing the signal represented in the bottom left is used for detection following transponder isolation. In comparison,

the spectra shown on the top right is from the signal that results from range bandpass filtering the full fast-time input. The zoomed in version of the full de-chirped signal in the bottom right better highlights the vibrational power at sidebands  $\pm f_{g,l}$  that exist at multiple PRF carriers rather than just the carrier related most closely to the range of the transponder.

In Fig. 4.9, detection results for a simulation scenario in which an interfering transponder is shown to further justify the non-conventional method of range processing via a bandpass filter. In this simulation, the vibrational displacement of the transponders are assumed to be a sequence of two vibrational tonal symbols,  $d(t) = 0.75 \sin(2\pi[500, 1000]t)$  mm. For completeness, stationary clutter was also simulated. The scenario that plays out in viewing the figure from left to right is that a transponder of interest is moving closer to a VRBC-equipped radar (increasing in SNR), passes an in-beam interfering transponder (at the range corresponding to  $-34.75$  dB in SNR), and then continues toward the radar (further increasing in SNR). Both the interfering transponder and transponder of interest are similar in RCS and otherwise.

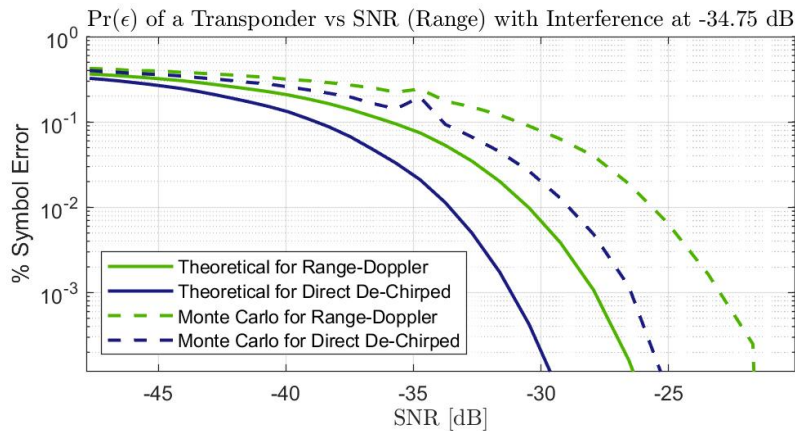


FIGURE 4.9: Probabilities of error when range-Doppler and direct de-chirped bandpass range processing are used.

These error results, found using maximum likelihood detection on the moving

transponder, show that using the direct de-chirped method that separates transponders in range via a bandpass filter provides better performance over the conventional range-Doppler processing method. The benefit of using the full de-chirped signal appears greatest at higher SNRs. This aligns well with the insight gained from Figs. 4.7 and 4.8, where it is clear that transponder power expands beyond a single PRF bandwidth. Both methods intuitively approach the scenario's expected random chance error as SNR drops.

One other perspective can prove useful in justifying the use of the full de-chirped signal for detection. When utilizing direct de-chirped range processing, the conventional issue of needing to mitigate for range migration is avoided. For the conventional range processing method, it can easily be understood that if the target is moving, the index  $m$  that contains the transponder will change across observation intervals. When this happens, typically range migration correction techniques are required, such as those in [68]. These methods help ensure that the migration across range bins minimally affects the return's micro-Doppler, which in this case equates to the vibrational content from the transponder. In using the full de-chirped signal for VRBC, this issue is eliminated as the bandpass filter can easily change its center frequency over time to following the target as it migrates from one range-associated PRF carrier to another.

#### *4.4.3 Clutter Filtering*

For each individual transponder detected and spatially isolated, clutter filtering is conducted. Typically, clutter filtering is done in the slow-time domain. For either of the range processing methods described, the clutter filtered signal can be modeled as an FIR filtered output

$$y(t) = \sum_{n=0}^N w_n y_{\text{method}}(t + nT_{\text{PRI}}) \quad (4.16)$$

where  $N$  is the order of the clutter filter and  $w_n$  is the filter coefficient for the  $n^{\text{th}}$  tap. For conventional range processing ('conv'), filter weights are applied to consecutive samples as the input signal is sampled at PRI time intervals

$$y_{\text{conv}}(t) = \tilde{\alpha}_{\text{tar}} e^{j \frac{4\pi}{\lambda_0} (r_{\text{tar}} + v_{\text{tar}} t - v_{\text{radar}} t + d(t))} + \sum_{k=1}^{K_{r_{\text{tar}}, \theta}(t)} \tilde{\alpha}_k e^{j \frac{4\pi}{\lambda_0} (r_{\text{tar}} - v_{\text{radar}} t)} + \tilde{n}(t) \quad (4.17)$$

for  $t = gT_{\text{PRI}}$ ,  $\forall g \in \mathbb{Z}$ . For the full de-chirped signal ('full'), filter weights are applied to samples spaced in time by the PRI since the input signal is sampled at the fast-time ADC rate  $f_s$ ,

$$\begin{aligned} y_{\text{full}}(t) &= \tilde{\alpha}_{\text{tar}} e^{j \frac{4\pi}{\lambda_0} (r_{\text{tar}} + v_{\text{tar}} t - v_{\text{radar}} t + d(t))} \sum_{g=0}^{G-1} z_{\text{tar}}(t - gT_{\text{PRI}}) \\ &+ \sum_{k=1}^{K_{r_{\text{tar}}, \theta}(t)} \tilde{\alpha}_k e^{j \frac{4\pi}{\lambda_0} (r_{\text{tar}} - v_{\text{radar}} t)} \sum_{g=0}^{G-1} z_k(t - gT_{\text{PRI}}) + \tilde{\eta}(t) \end{aligned} \quad (4.18)$$

for  $t = \frac{m}{f_s}$ ,  $\forall m \in \mathbb{Z}$ . When clutter is stationary relative to the radar, ie.  $v_{\text{radar}} = 0$ , one solution for clutter filtering is to have the only non-zero filter coefficients be  $w_0 = 1$  and  $w_1 = -1$ . In other words, because stationary clutter is consistent across chirps, clutter filtering results in subtracting off the previous chirp to mitigate the portion of the return that is consistent. The frequency response of such a filter would appear as a series of notches at multiples of the PRF for the full de-chirped signal. Figure 4.8 shows the spectra of VRBC return before (in red) and after (in yellow) clutter filtering in this manner. In practice, it is possible that clutter could be non-stationary. Take for example when  $v_{\text{radar}} \neq 0$  or clutter consists of leaves from a nearby tree moving in the wind. In these cases, filter weights will be less trivial and methods to estimate the filter weights such as using space-time adaptive processing techniques would be required [69].

It should be acknowledged that clutter filtering can greatly affect the transponder-derived return. As was done in Chapter 3 for larynx vibrations, consider a tonal

displacement. The DFT of  $e^{j\frac{4\pi}{\lambda_0}\gamma_{\text{tar}} \sin(2\pi f_{\text{tar}} t)}$  provides a DC, or 0 Hz Doppler, component of magnitude  $J_0(\frac{4\pi\gamma_{\text{tar}}}{\lambda_0})$ . When  $v_{\text{tar}} = v_{\text{radar}} = 0$ , this power primarily remains at 0 Hz Doppler in the context of the full signal. If  $v_{\text{tar}} \neq 0$  or  $v_{\text{radar}} \neq 0$ , this energy gets pushed to the primary target peak at the Doppler frequency of  $\frac{2}{\lambda_0}(v_{\text{tar}} - v_{\text{radar}})$ . Similarly, clutter exhibits a peak at the Doppler frequency  $-\frac{2}{\lambda_0}(v_{\text{radar}})$ . Often it is true that the transponder is not moving,  $v_{\text{tar}} = 0$ , or that the transponder is moving but on an object bigger than itself such that clutter from the same range and angle bin also has the additional,  $v_{\text{tar}}$ , velocity term. In these cases, clutter will appear at the same frequency as the tonal vibrational displacement power  $|J_0(\frac{4\pi\gamma_{\text{tar}}}{\lambda_0})|^2$ .

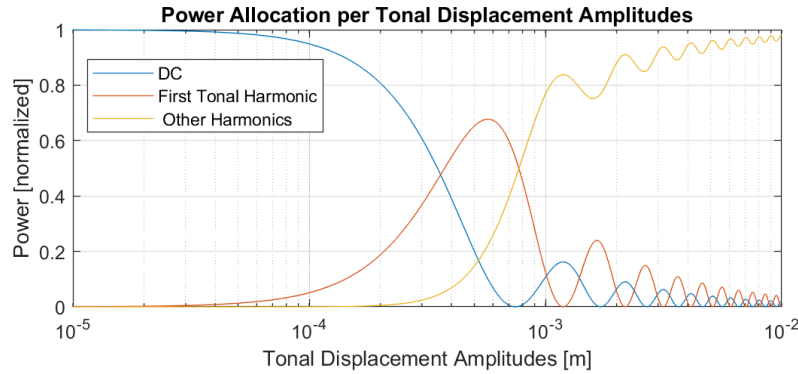


FIGURE 4.10: Tonal vibrational power allocation versus the tone's displacement amplitude assuming a 77 GHz operating frequency.

Filtering out signal content at this frequency, as a clutter filter is designed to do, will then alter the vibrational displacement-specific signal component. For a better understanding of the magnitude of this effect, consider Fig. 4.10. This plot shows that if the amplitude of the tonal displacement is less than about 50 micrometers, that nearly all the power of the associated return is at  $f_{g,0}$ , which equated to 0 Hz Doppler in the stationary case. Once that vibrational displacement amplitude grows to 100s of micrometers, a large portion of the vibration-induced power exists at the first tonal harmonic of  $f_{g,1}$ . This is ideal in VRBC as it means that primarily the first harmonic,  $l = 1$ , can be used for transponder detection and a larger portion of the

transponder's vibrational power will not be filtered out during conventional clutter filtering. The latter benefit remains true as amplitudes of millimeters or greater are achieved, however, the former benefit does not. At these greater displacement amplitudes, multiple harmonics are needed to capture the majority of the transponder's vibrational return power. As seen in Fig. 4.4, the first two decades of Fig. 4.10 are where the real data acquisition displacements are anticipated to reside at.

It is of course preferred to have a clutter filter that does not eliminate vibration-induced power while still minimizing the contribution of true clutter. In practice, this is not trivial. In Chapter 6, initial work towards a more ideal clutter filtering method is presented, but it has yet to provide robust results for use in practice. Through the remainder of this chapter, we assume that clutter filtering impacts the target return in a known way such that it can be accurately modeled and used in detection.

The output signal from clutter filtering that will be used in detection can therefore be written as

$$y(t) = \sum_{n=0}^N w_n \left( \tilde{\alpha}_{\text{tar}} e^{j \frac{4\pi}{\lambda_0} ((v_{\text{tar}} - v_{\text{radar}})(t + nT_{\text{PRI}}) + d(t + nT_{\text{PRI}}))} \sum_{g=0}^{G-1} z_{\text{tar}}(t - (g - n)T_{\text{PRI}}) \right) + \tilde{\eta}(t) \quad (4.19)$$

where clutter is assumed to have been perfectly eliminated. The right-most plot in Fig. 4.11 provides the range-Doppler intensity (RDI) plot for a real example using this processing. Fig. 4.11 also provides the RDI for the signal after beamforming and bandpass range processing to visualize the full transponder isolation and clutter filtering steps taken thus far.

#### 4.4.4 Synchronization

After clutter filtering, synchronization must occur to find the start of a VRBC message sequence. This is done for each transponder individually. To achieve synchro-

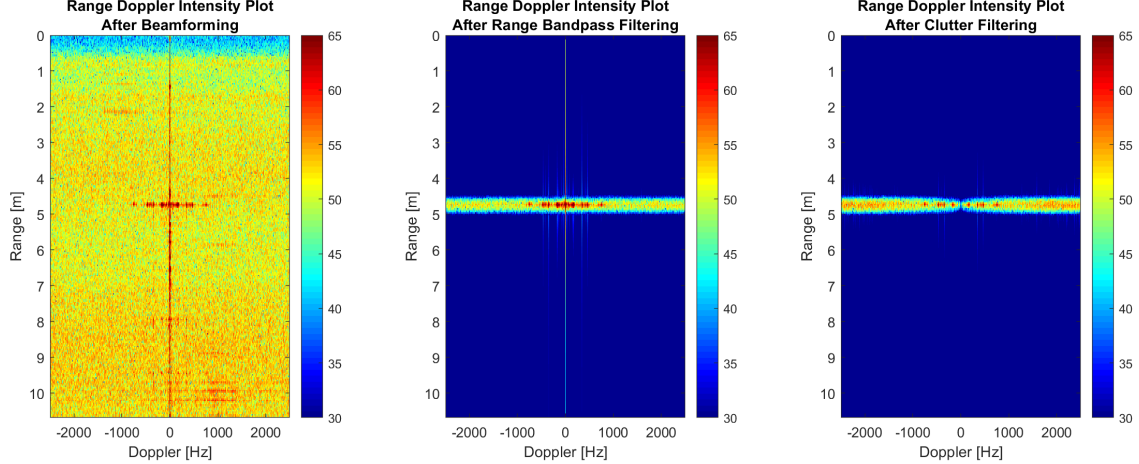


FIGURE 4.11: Range-Doppler intensity plots throughout target isolation and clutter filtering.

nization, a known preamble sequence with an autocorrelation function that results in a significantly sharp peak is used for all vibrational message sequences. The preamble signal discussed here is distinctly a displacement signal within the overall signal's phase. It is not the excitation signal that sources the vibrational movement of the transponder's surface.

The displacement signal modeled thus far,  $d(t)$ , is not expected to equivalently be the system excitation signal for real transponders. Rather, the displacement of a VRBC surface,  $d(t)$ , can be written as a function of the digital signal sent to the transponder's exciter,  $x(t)$ . It is assumed that  $d(t)$  can be modeled as the output to a linear time-invariant (LTI) system,

$$d(t) = x(t) \otimes h(t) \quad (4.20)$$

where  $\otimes$  is the symbol for the convolution operation and  $h(t)$  is the transponder's surface impulse response.

For synchronization, obtaining an estimate of the start time of a VRBC sequence requires an accurate estimate of the observed displacement signal which resides in the phase of the full return. Unfortunately, conventional clutter filtering not only

eliminates the clutter term but also often creates phase changes for the transponder term. Deep notch filters at clutter ridge Doppler frequencies, such as the clutter filter that consists of subtracting the previous chirp from the current, fall into this category of clutter filters that modify the transponder term's phase.

In this subsection, it is assumed that more ideal clutter filtering such as that described in Chapter 6 or otherwise are used. Alternatively, instances where there is minimal clutter at the range and Doppler bin of the transponder suffice too, as the full return can be initially modeled as containing minimal clutter to begin with. The VRBC acquisition setup used for the real data in this dissertation, follows this latter assumption approximately.

The phase estimate used in practice comes from looking at the phase of the slow-time signal at the transponder's range bin using conventional radar range-Doppler processing methods

$$\angle y_{\text{conv}}(t) \approx \frac{4\pi}{\lambda_0}(v_{\text{tar}}t - v_{\text{radar}}t + d(t)) + \Phi + n_{\Phi}(t) \quad (4.21)$$

where  $\Phi$  is a phase offset and  $n_{\Phi}(t)$  is additive phase noise caused by random fluctuations of the radar oscillator. It is assumed that  $\Phi$  is constant for a VRBC observation. This equates to assuming that no significant phase noise drift is observed and that the complex amplitude of the return remains constant.

Next, the estimated trajectory of the transponder from the target detection sub-chain is used to adjust for bulk velocity movements such that

$$\hat{d}(t) = \angle y_{\text{conv}}(t) - \frac{4\pi}{\lambda_0}(v_{\text{tar}}t - v_{\text{radar}}t) = \frac{4\pi}{\lambda_0}d(t) + \Phi + n_{\Phi}(t). \quad (4.22)$$

Here  $\hat{d}(t)$  indicates an estimate of the displacement. The scalar amplitude and offset do not affect the synchronization process, so they are left alone, though subtracting the average phase observed and scaling by  $\frac{\lambda_0}{4\pi}$  can easily be done if desired. Fig. 4.12 shows an example phase estimate using these steps from the VRBC data acquisition

setup described in this chapter.

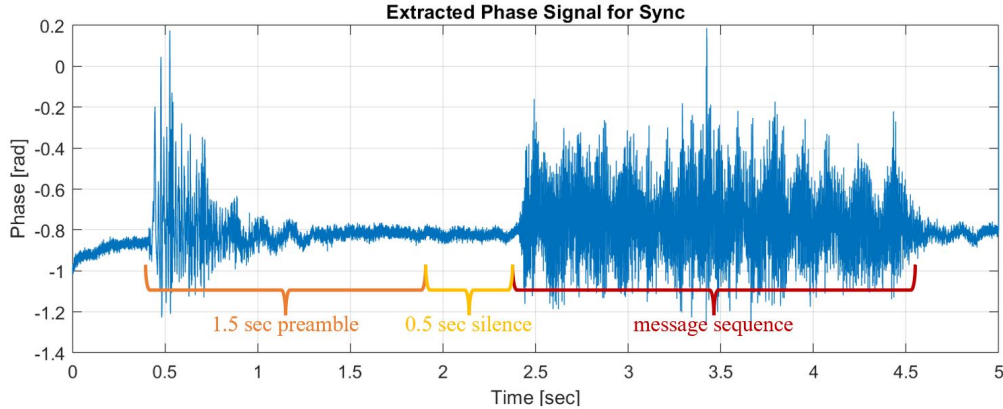


FIGURE 4.12: This example includes a chirp preamble followed by 0.5 seconds of silence and a VRBC sequence of 4 different tonal vibration symbols.

In the shown example, the displacement signal consists of an unknown duration of vibrational silence followed by a preamble, another period of short silence, and then the VRBC sequence. When the impulse response  $h(t)$  has yet to be estimated, which is expected for arbitrary transponders observed outside of a laboratory setup, an estimate of the displacement signal cannot be directly calculated from the phase estimate and a known excitation signal. Instead the assumption that the vibrational surface is an LTI system is used to find the start time.

The magnitude-squared coherence (MSC) between two signals is well known for providing a measure that estimates the extent to which one signal can be predicted from the other using a linear model. Let

$$C_{x_{\text{pre}d_i}}(f, t_i) = \frac{|S_{x_{\text{pre}d_i}}(f)|^2}{S_{x_{\text{pre}}}^*(f) S_{d_i d_i}(f)} \quad (4.23)$$

be the MSC between the preamble excitation signal  $x_{\text{pre}}(t)$  and a portion of the displacement signal  $d(t)$  where  $t_i < t \leq t_i + T_{\text{pre}}$ , which takes on values from 0 to 1.  $T_{\text{pre}}$  is used to describe the duration of the preamble, and  $t_i$  indicates a delay in the overall estimated displacement signal under consideration.  $S_{x_{\text{pre}d_i}}(f)$  is the cross spectral

density between the preamble excitation and displacement signal, while  $S_{x_{\text{pre}}x_{\text{pre}}}(f)$  and  $S_{d_i d_i}(f)$  are the auto spectral densities of the preamble excitation and displacement signals respectively. For a perfectly LTI system,  $S_{d_i d_i}(f) = |H(f)|^2 S_{x_{\text{pre}}x_{\text{pre}}}(f)$  and  $S_{x_{\text{pred}_i}}(f) = H(f) S_{x_{\text{pre}}x_{\text{pre}}}(f)$ , so

$$C_{x_{\text{pred}_i}}(f, t_i) = \frac{|H(f) S_{x_{\text{pre}}x_{\text{pre}}}(f)|^2}{S_{x_{\text{pre}}x_{\text{pre}}}(f) |H(f)|^2 S_{x_{\text{pre}}x_{\text{pre}}}(f)} = 1. \quad (4.24)$$

By observing the MSC over time using a sliding window the length of the preamble excitation signal, moments where the phase estimate most closely resembles the output of an LTI system in relation to the known excitation preamble can be found. Consider Fig. 4.13, which shows this exact method with the real data shown in Fig. 4.12.

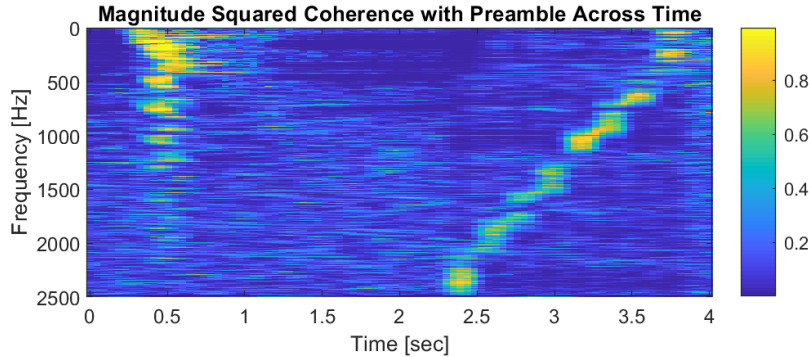


FIGURE 4.13: Magnitude squared coherence over time with a known 1.5 second long chirp whose instantaneous frequency swept from 0 Hz to PRF/2.

As the plot shows, multiple frequencies indicate a linear relationship between the preamble and displacement around 0.5 seconds. The large MSC measurements occurring later on in this figure result from the sudden impulse noise observed in the data at around 3.4 seconds. Because they do not align in time across multiple frequencies that are known to be present in the preamble, they can be discarded as indicators of a potential preamble start time.

This data collection demonstrates how strong peaks across multiple frequencies

are needed to estimate the start time for a preamble, thus justifying the need for the preamble excitation signal to be wide band, such as a chirp. Start time estimation can then simply consist of finding the time index when the maximum amount of frequencies from the preamble indicate an LTI system. Since the preamble in this example was a chirp whose instantaneous frequency swept from 0 Hz to PRF/2 Hz, the full Doppler bandwidth makes up the range of frequencies of interest.

$$\hat{t}_{\text{start}} = \operatorname{argmax}_{t_i} \sum_f C_{x_{\text{pred}_i}}(f, t_i) \quad (4.25)$$

For this collection,  $\hat{t}_{\text{start}}$  came to be 0.4025 seconds. By acknowledging the agreed upon protocol, which in this case was a 1.5 second preamble followed by 0.5 seconds of silence and then the beginning of the VRBC sequence, the sequence start can be found to be 2.4025 seconds. The clutter filtered signal in Equation 4.19 can then be delayed to provide synchronization going into the message detection sub-chain.

The sliding window MSC plot also provides key information about the decay time of certain resonant frequencies. Using the analysis shown in Section 4.2, this particular collection consists of a sequence of tonal symbols at frequencies [150, 350, 450, 750] Hz. Taking slices of Fig. 4.13 at these frequencies reveals anticipated decay durations of these tones.

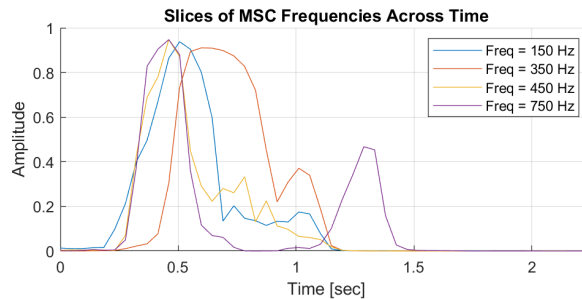


FIGURE 4.14: Slices of the sliding window MSC plot at frequencies of interest.

Fig. 4.14 shows that for the 450 and 750 Hz tones, a decay time of around 0.25 seconds may be required for the effects of those tones to decay out. On the other

hand, the 350 Hz tone has a relatively longer decay as indicated by the width of the tone's peak. In this case, a decay time of nearly a second may be needed. As will be seen later, long decay requirements will lead to inter symbol interference for sequences where shorter tonal symbols are used in a sequence with no spacing between their transmissions.

#### 4.4.5 Transponder Impulse Response Estimation

Before conducting detection, transponder impulse response estimation is required to allow for accurate symbol modeling. In practice, we used a chirp preamble not only because its bandwidth allows for synchronization but also because it allows for a good approximation in impulse response estimation. Consider the chirp preamble signal,  $x_{\text{pre}}(t)$  whose instantaneous frequency once again spans from 0 to PRF/2 Hz over the predetermined arbitrary duration of 1.5 seconds. The auto spectral density of this preamble is seen in Fig. 4.15.

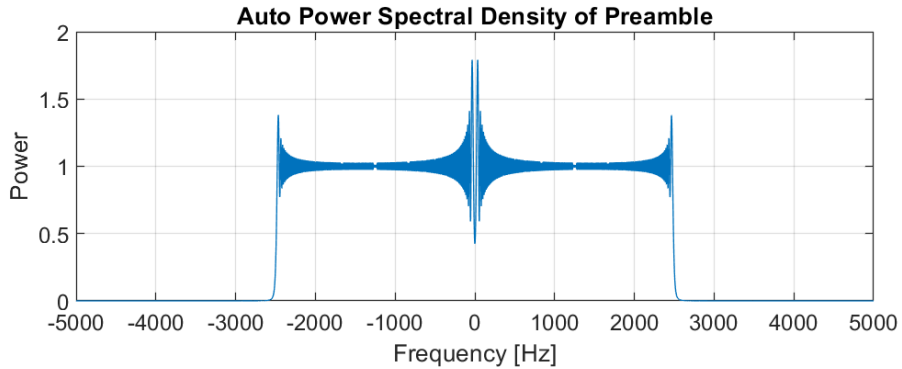


FIGURE 4.15: Auto spectral density for a chirp preamble.

Though the preamble's auto spectral density reveals that the preamble does not have a perfectly uniform spectra across its used bandwidth, it is true that the power is significantly comparable across frequency. Having an sufficiently uniform spectra is particularly useful in the conventional cross-spectral method for system identification. The cross-spectral method is the least-squared solution method for solving the

classic system identification problem where an input and output are known but the system response is not [70]. This method works by first calculating the frequency response using

$$H(f) = \frac{S_{xd}(f)}{S_{xx}(f)}. \quad (4.26)$$

By taking an inverse Fourier transform,

$$h(t) = \mathcal{F}^{-1}\{H(f)\} \quad (4.27)$$

then provides an estimate of the impulse response.

When the problem at hand assumes statistically independent additive zero-mean Gaussian noise, such as the phase noise present in this application, the estimate in 4.27 is asymptotically unbiased. In other words, the estimate for  $h(t)$  approaches its true value for largely sampled preambles. The performance, however, is limited by the variance of the phase noise, ie. the SNR. By plotting the short-time Fourier Transform of the preamble displacement estimate, as shown in Fig. 4.16, it can be seen that even the example shown has an SNR in phase ranging from less than 0 dB all the way to 20+ dB depending on the instantaneous frequency of the preamble chirp.

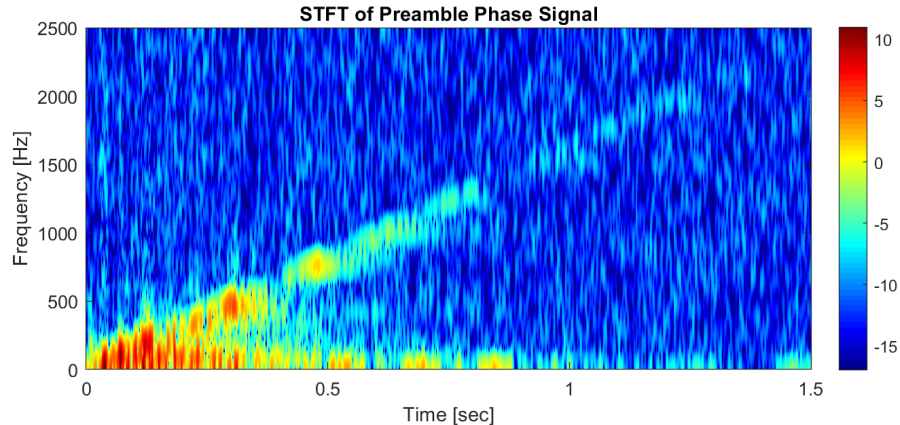


FIGURE 4.16: An STFT of the preamble phase signal.

Some researchers have used time-frequency filtering methods to minimize the phase noise, therefore raising the SNR [71]. In the case of VRBC, however, long resonant frequency decay times can make it difficult to avoid also filtering out system resonant affects. In reference to Fig. 4.16, these methods look like a time-varying bandpass filter that centers at the expected instantaneous frequency of the chirp. It is possible that a modified version of this processing method could be used to further increase SNR especially at high vibrational frequencies, but because sufficiently large SNRs are observed at the anticipated VRBC operating frequencies, we continue the system identification process without the additional noise reducing technique.

Using the cross-spectral method or estimating the system impulse response of the data collection described thus far in this chapter, we get Fig. 4.17. From the

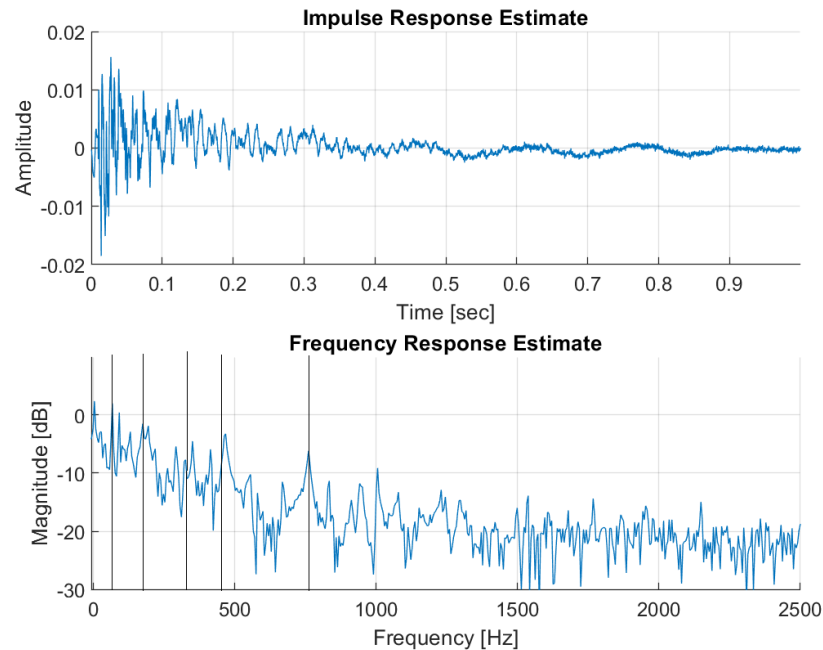


FIGURE 4.17: The vertical lines are located at the plate's expected natural frequencies.

figure, we can see that peaks at the expected natural frequencies of the aluminum plate according to Table 4.2 match well with what the natural frequencies have been

estimate to be using this method. Furthermore, Fig. 4.18 shows that when the known excitation signal is convolved with the estimated impulse response, the signal matches closely with the observed phase.

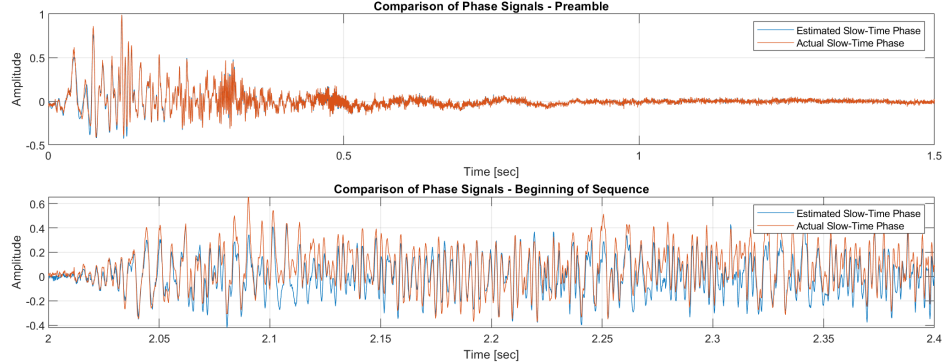


FIGURE 4.18: The estimate signal was found by convolving the known excitation with the estimated system impulse response.

The impulse response estimate is taken as an input to the processing sub-chain labeled as message detection in Fig. 4.5. Without an accurate impulse response estimation, over simplified assumptions must be made about what the displacement looks like for various communication symbols used within the VRBC sequence excitation.

#### 4.4.6 Message Detection

For VRBC sequences, consider excitation signals that consist of  $Q$  consecutive single symbol excitations,

$$x_{\text{seq}}(t) = \sum_{q=1}^Q x_q(t - (q-1)T_{\text{sym}}) \quad (4.28)$$

where each  $x_q(t) \in \mathcal{X}$ . The set  $\mathcal{X}$  contains  $M$  different symbol excitations that have non-zero values only from  $0 \leq t < T_{\text{sym}}$ ,  $\mathcal{X} = \{x^{(1)}(t), x^{(2)}(t), \dots, x^{(M)}(t)\}$ . The excitation length is the same for all  $M$  possible symbols and is notated as  $T_{\text{sym}}$  seconds or  $L_{\text{sym}}$  samples long, where  $L_{\text{sym}} = T_{\text{sym}}f_s$ . For simplicity, it is assumed

that the symbol length is a positive integer multiple of the pulse repetition interval (PRI). In the real data collection described within this chapter, four tonal symbols at frequencies [150, 350, 450, 750] were used to comprise the set  $\mathcal{X}$ .

Because the vibrating surface is modeled as a linear time-invariant system, the vibrational displacement of the sequences is estimated as

$$d(t) = \sum_{q=1}^Q d_q(t - (q-1)T_{\text{sym}}) \quad (4.29)$$

where

$$d_q(t) \approx x_q(t - qT_{\text{sym}}) \otimes h(t) \quad (4.30)$$

for  $0 \leq t < T_{\text{sym}}$  and 0 otherwise. It is apparent through Equation 4.30 that  $d_q(t)$  will be non-zero beyond its symbol interval duration when  $h(t)$  is not an ideal impulse or the possible symbol excitations do not allocate an adequate portion of their duration for allowing resonant displacements to decay to some negligible amount. Chapter 6 will provide details for handling such cases, as they are expected to be common and require a separate framework. For now, it is assumed that not modeling the described symbol interference will suffice for detection.

For the real data collection, this is quite obviously not an accurate assumption. For completeness, the rest of the processing chain is still carried out with the expectation that some amount of incorrect detections will occur due to this inaccuracy. Fig. 4.19 shows this truth, especially when viewing the symbol displacements and recognizing that this specific system leads to maximum symbol displacements well after the time interval specific to a single symbol duration. Also of note from Fig. 4.19 is how the symbol tones have different maximum displacements, the magnitude of which does not necessarily correlate to the symbol decay time observed from the MSC slices in Fig. 4.14. For instance, we saw that the 350 Hz tone takes nearly twice as long to decay out when compared to the other three tonal symbols in Fig. 4.14.

Fig. 4.19, however, shows that the 350 Hz tone is the excitation whose resulting maximum displacement is only third largest.

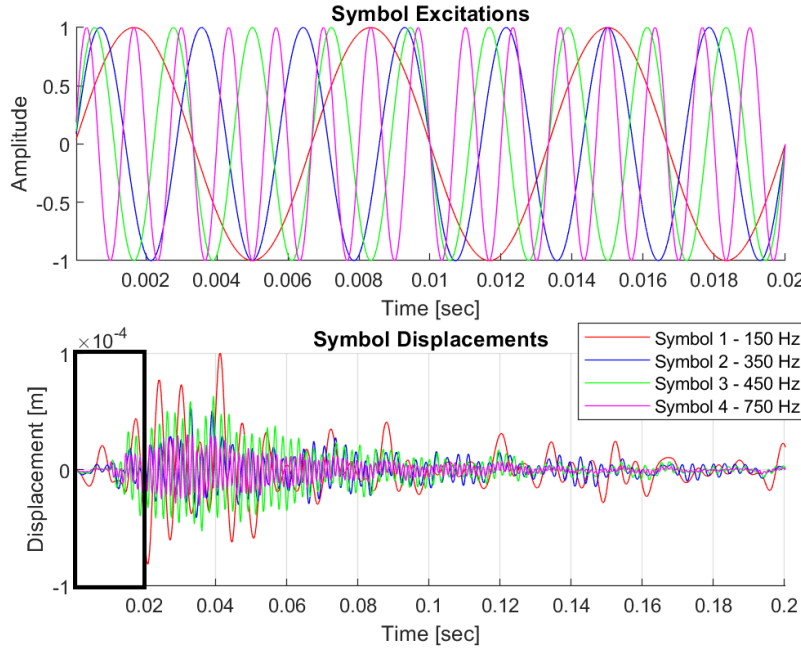


FIGURE 4.19: Symbol excitations and displacements for the real data collection.

Regardless, substituting the displacement signal from Equation 4.29 into the clutter filtered and synchronized return in Equation 4.19, the VRBC channel can be described by the excitation/message for a given transponder trajectory,

$$y(t) = \underbrace{\sum_{n=0}^N w_n \left( \tilde{a}_{\text{tar}} e^{j \frac{4\pi}{\lambda_0} ((v_{\text{tar}} - v_{\text{radar}})(t + nT_{\text{PRI}}) + d(t + nT_{\text{PRI}}))} \sum_{g=0}^{G-1} z_{\text{tar}}(t - (g-n)T_{\text{PRI}}) \right)}_{\text{target-derived return component, } y_{\text{tar}}} + \tilde{\eta}(t) \quad (4.31)$$

This signal can be written to highlight separate symbol intervals using

$$y(t) = \sum_{q=1}^Q y_q(t - (q-1)T_{\text{sym}}), \quad (4.32)$$

where

$$y_q(t) = y_{q,\text{tar}}(t) + \tilde{\eta}(t) \quad (4.33)$$

and  $y_{q,\text{tar}}(t) = y_{\text{tar}}(t)$  for  $(q-1)T_{\text{sym}} \leq t < qT_{\text{sym}}$  and 0 elsewhere. The target-derived component,  $y_{q,\text{tar}}(t)$  takes on a finite number of realizations described by the set  $\mathcal{Y}_q = \{y_{q,\text{tar}}^{(1)}(t), y_{q,\text{tar}}^{(2)}(t), \dots, y_{q,\text{tar}}^{(D)}(t)\}$ , which directly relate to the displacement of the VRBC transponder.  $D$  describes the number of possible symbol interval displacements, which for the no-ISI case is equivalently  $M$ . Leaving  $D$  defined separately from  $M$  allows for clearer notation in Chapter 6.

Mathematically,  $y_{q,\text{tar}}^{(d)}(t) = y_{\text{tar}}(t)$  given  $d(t) = d^{(D)}(t)$ . Because the return depends on the transponder's trajectory, ie.  $r_{\text{tar}}$ ,  $v_{\text{radar}}$ , and  $v_{\text{tar}}$ , the set  $\mathcal{Y}_q$  does differ per symbol interval  $q$  when the target is moving relative to the radar. The cardinality of this set for all  $q$  remains constant, however, due to the number of possible displacements being unaffected by relative transponder motion. If the transponder is not moving relative to the radar, then  $\mathcal{Y}_q$  is the same for all  $q$ .

Once all symbol displacements have been estimated, VRBC detection can be completed using either single symbol maximum likelihood methods. At a top level, VRBC has the following progression from symbol input to symbol prediction,

$$\text{Input Symbol } m_q \xrightarrow{\text{Channel}} \text{Output Signal } \mathbf{y}_q \xrightarrow{\text{Detection}} \text{Predicted Symbol } \hat{m}_q . \quad (4.34)$$

where predicted symbols are denoted as  $\hat{m}$ . At this point in detection, the symbol interval return signals  $y_q(t)$  are organized into vector form. We use  $\mathbf{y}_q$  to denote the full  $L_{\text{sym}} \times 1$  column vector of signal samples from the  $q^{\text{th}}$  symbol interval,  $\mathbf{a}_q$  to denote the target-derived component, and  $\boldsymbol{\eta}_q$  contains the band-limited AWGN samples,

$$\mathbf{y}_q = \mathbf{a}_q + \boldsymbol{\eta}_q . \quad (4.35)$$

Let the possible target-derived data vectors be specified using the notation  $\mathbf{a}^{(m)}$ , indicating it results from the current symbol displacement associated with the  $m^{\text{th}}$  symbol.

Single symbol maximum likelihood detection in additive noise is performed using

$$\hat{m}_q = \arg \max_m \Pr(m_q = m) e^{-\frac{1}{2}(\mathbf{y}_q - \mathbf{a}^{(m)})^H \Gamma^{-1} (\mathbf{y}_q - \mathbf{a}^{(m)})} \quad (4.36)$$

where  $\Gamma$  is the noise covariance matrix. The probability of a particular symbol interval being a given symbol,  $\Pr(m_q = m)$ , is simply  $\frac{1}{M}$  in the case where resonant effects have not been considered, no coding constraints have been utilized, and an equiprobable symbol distribution is assumed.

Once the predicted symbol sequence is found, an estimate of the achieved rate is calculable using the errors between the true and predicted symbol sequences,  $\mathbf{m} = [m_1, m_2, \dots, m_Q]^T$  and  $\hat{\mathbf{m}} = [\hat{m}_1, \hat{m}_2, \dots, \hat{m}_Q]^T$ . The observed mutual information rate is given by

$$R_{\text{obs}} = \frac{H(\hat{m}_q) - H(\hat{m}_q|m_q)}{T_{\text{sym}}}, \quad (4.37)$$

where  $H(\cdot)$  indicates entropy. Consider a confusion matrix,  $\mathbf{C}$ , describing the errors observed.  $C_{m,n}$  describes the number of times the  $m^{\text{th}}$  symbol was predicted to be the  $n^{\text{th}}$  symbol. Components of Equation 4.37 are then

$$H(\hat{m}_q) = - \sum_n \left( \frac{\sum_m C_{m,n}}{Q} \right) \log_2 \left( \frac{\sum_m C_{m,n}}{Q} \right) \quad (4.38)$$

and

$$H(\hat{m}_q|m_q) = \sum_m \left( \frac{\sum_n C_{m,n}}{Q} \right) H(\hat{m}_q|m_q = m), \quad (4.39)$$

where

$$H(\hat{m}_q|m_q = m) = - \sum_n \left( \frac{C_{m,n}}{\sum_n C_{m,n}} \right) \log_2 \left( \frac{C_{m,n}}{\sum_n C_{m,n}} \right). \quad (4.40)$$

In a laboratory experiment where the sequence transmitted is known, the achieved rate can be calculated in this manner.

Table 4.2: Confusion Matrix for Single Symbol ML on the Real Data Collection

True Symbol	Detected Symbol			
	150 Hz	350 Hz	450 Hz	750 Hz
150 Hz	24	1	0	0
350 Hz	1	10	1	20
450 Hz	1	0	21	6
750 Hz	2	0	3	14

For the real data collection in this chapter, the resulting detection confusion matrix was

Table 4.2 suggests exactly what was expected. System modifications, particularly intersymbol interference methods or better transponder design, are needed to achieve better performance, as the probability of detection was only about 66% in this example. The rate in this case calculates out to 48.7 bits per second. In Chapter 6, this rate will nearly double by simply accounting for some of the resonant effects.

# 5

## A VRBC Bound and Discussion of System Design Choices

### 5.1 An Upper Bound on VRBC Rate

The ultimate goal in communication systems is to have a system that can reliably transmit as much information as possible as quickly as possible with minimal errors. Developing an upper bound on a communication system's rate is therefore appealing as it can provide a quick way of quantifying the system's capabilities when a direct analytical expression for the system's performance is unable to be found or the time and effort needed to perform experiments and/or Monte Carlo simulations is too great.

A system's rate can be calculated using the concept of mutual information rate (MIR). In Chapter 4, the equation for MIR given a data collection's confusion matrix was presented. MIR in general is a powerful concept in probability theory and information theory that provides a measurement for the amount of information obtained about one random variable from observing another. In the case of VRBC, this describes how much information about the original message is present in the

detected message per unit of transmission time. When perfect detection is achieved, the MIR is naturally bounded by the rate demonstrated by the input coding scheme (symbol choices, symbol lengths, etc.). MIR is defined as

$$R = \frac{\mathcal{I}(m_q; \hat{m}_q)}{T_{\text{sym}}}, \quad (5.1)$$

where  $\mathcal{I}(\cdot; \cdot)$  is mutual information.

To declare an upper bound on the possible communication rate, the data processing inequality is first used on the mutual information that is used in defining the mutual information rate

$$\mathcal{I}(m_q; \hat{m}_q) \leq \mathcal{I}(m_q; \mathbf{y}_q). \quad (5.2)$$

Therefore,

$$R \leq \frac{\mathcal{I}(m_q; \mathbf{y}_q)}{T_{\text{sym}}} = \frac{h(\mathbf{y}_q) - h(\mathbf{y}_q | m_q)}{T_{\text{sym}}}, \quad (5.3)$$

where  $h(\cdot)$  now indicates differential entropy.

The differential entropy of the output signal data vector is

$$h(\mathbf{y}_q) = - \int f(\mathbf{y}_q) \log_2 f(\mathbf{y}_q) d\mathbf{y}_q. \quad (5.4)$$

Because VRBC models the return used for detection as a known transponder-derived data vector dependent on symbol displacement with band-limited AWGN, the distribution of the output data vector  $f(\mathbf{y}_q)$  can be written as the weighted sum of those displacement-conditioned densities,

$$f(\mathbf{y}_q) = \sum_{i=1}^D \Pr(d_q(t) = d^{(i)}(t)) f(\mathbf{y}_q | d_q(t) = d^{(i)}(t)). \quad (5.5)$$

Equation 5.5 shows that the distribution of the output data vector is a homoscedastic (same covariance) complex multivariate Gaussian mixture. Unfortunately, there is no analytical solution to the differential entropy of a complex mul-

tivariate Gaussian homoscedastic mixture. An upper bound on this differential entropy is found by using the lower bound for the expected value of log-sum [72]. The resultant differential entropy is

$$h(\mathbf{y}_q) \leq - \sum_{i=1}^D \Pr(d_q(t) = d^{(i)}(t)) \log_2(\zeta_i) + h(\mathbf{y}_q | d_q(t)) \quad (5.6)$$

where

$$\zeta_i = \sum_{i'=1}^D \Pr(d_q(t) = d^{(i')}(t)) 2^{-\beta_{i,i'}}$$

and

$$\beta_{i,i'} = (\mathbf{a}^{(i)} - \mathbf{a}^{(i')})^H \Gamma^{-1} (\mathbf{a}^{(i)} - \mathbf{a}^{(i')}).$$

Previously, the transponder-derived data vectors,  $\mathbf{a}^{(i)}$ , were limited by  $i \in \{1, 2, \dots, M\}$ . Now, let it be clear the index  $i \in \{1, 2, \dots, D\}$  where  $D$  may not be equal to  $M$  as it represents all possible symbol interval displacements which can grow larger than  $M$  when resonant effects are accounted for.

**Theorem 1.** The inequality used in proving this upper bound on differential entropy is the lower bound on the expected value of a log-sum,  $\mathbb{E}_g[\log_2 \sum_k f(x_k)] \geq \log_2 \sum_k 2^{\mathbb{E}_g[\log_2 f(x_k)]}$ . Because  $\log_2$  is a concave function, we know

$$\log_2 \left( \sum_k \pi_k x_k \right) \geq \sum_k \pi_k \log_2 x_k, \quad (5.7)$$

where  $\pi_k$  is shorthand for  $\Pr(k)$ . Further,  $\pi_k \geq 0$  for all  $k$ ,  $\sum_k \pi_k = 1$ , and  $x_k$  is an arbitrary random variable that takes on some distribution according to  $k$ . Specifically, we choose  $\pi_k = \frac{2^{\mathbb{E}_g[\log_2 f(x_k)]}}{\sum_l 2^{\mathbb{E}_g[\log_2 f(x_l)]}}$ . This choice in  $\pi_k$  is not arbitrary. To achieve a tight lower bound,  $\pi_k$  can be solved for using Lagrange multipliers to

maximize the lower bound while still requiring that they sum to 1. The expectation used in this proof is taken over a distribution notated  $g$ . Therefore,

$$\begin{aligned}
\mathbb{E}_g \left[ \log_2 \sum_k f(x_k) \right] &= \mathbb{E}_g \left[ \log_2 \sum_k \frac{\pi_k f(x_k)}{\pi_k} \right] \\
&\geq \mathbb{E}_g \left[ \sum_k \pi_k \log_2 \left( \frac{f(x_k)}{\pi_k} \right) \right] \\
&= \sum_k \pi_k \mathbb{E}_g \left[ \log_2 \left( \frac{f(x_k)}{\pi_k} \right) \right] \\
&= \sum_k \pi_k (\mathbb{E}_g [\log_2 f(x_k)] - \log_2 \pi_k) \\
&= \sum_k \pi_k (\log_2 2^{\mathbb{E}_g [\log_2 f(x_k)]} - \log_2 \pi_k) \\
&= \sum_k \pi_k \log_2 \frac{2^{\mathbb{E}_g [\log_2 f(x_k)]}}{\pi_k} \\
&= \sum_k \pi_k \log_2 \sum_l 2^{\mathbb{E}_g [\log_2 f(x_l)]} \\
&= \log_2 \sum_l 2^{\mathbb{E}_g [\log_2 f(x_l)]}.
\end{aligned} \tag{5.8}$$

To summarize, the lower bound on the expectation of a log-sum is

$$\mathbb{E}_g \left[ \log_2 \sum_k f(x_k) \right] \geq \log_2 \sum_k 2^{\mathbb{E}_g [\log_2 f(x_k)]}. \tag{5.9}$$

Next, consider the Kullback-Liebler (KL) distance between two homoscedastic complex multivariate Gaussian distributions,

$$\text{KL} \left( f(\mathbf{y}_q | d_q(t) = d^{(i)}(t)) || f(\mathbf{y}_q | d_q(t) = d^{(i')}(t)) \right) = \beta_{i,i'}. \tag{5.10}$$

Using shorthand for a conditional distribution  $f(\mathbf{y}_q | d_q(t) = d^{(i)}(t))$  as  $f_i$ , conditional differential entropy  $h(\mathbf{y}_q | d_q(t) = d^{(i)}(t))$  as  $h_i$ , the probability  $\Pr(d_q(t) = d^{(i)}(t))$

as  $\pi_i$  again, and the KL distance  $\text{KL} \left( f(\mathbf{y}_q | d_q(t) = d^{(i)}(t)) || f(\mathbf{y}_q | d_q(t) = d^{(i')}(t)) \right)$  as  $\text{KL}(i || i')$ ,

$$\begin{aligned}
h(\mathbf{y}_q) &= - \int \sum_{i=1}^D \pi_i f_i \log_2 \left( \sum_{i'=1}^D \pi_{i'} f_{i'} \right) d\mathbf{y}_q \\
&= - \sum_{i=1}^D \pi_i \mathbb{E}_{f_i} \left[ \log_2 \left( \sum_{i'=1}^D \pi_{i'} f_{i'} \right) \right] \\
&\leq - \sum_{i=1}^D \pi_i \log_2 \left( \sum_{i' \in D} 2^{\mathbb{E}_{f_i} [\log_2 \pi_{i'} f_{i'}]} \right) \\
&= - \sum_{i=1}^D \pi_i \log_2 \left( \sum_{i'=1}^D 2^{\int f_i \log_2 \frac{\pi_{i'} f_{i'} f_i}{f_i} d\mathbf{y}_q} \right) \\
&= - \sum_{i=1}^D \pi_i \log_2 \left( \sum_{i'=1}^D \pi_{i'} 2^{-h_i} 2^{-\text{KL}(i || i')} \right) \\
&= \sum_{i=1}^D \pi_i h_i - \sum_{i=1}^D \pi_i \log_2 \left( \sum_{i'=1}^D \pi_{i'} 2^{-\beta_{i,i'}} \right). \tag{5.11}
\end{aligned}$$

Rewriting Equation 5.11 without the shorthand notation gives Equation 5.6.

Because  $h(\mathbf{y}_q | m_q) \geq h(\mathbf{y}_q | d_q(t))$ , substituting the bound on  $h(\mathbf{y}_q)$  into the equation for rate provides the upper bound

$$R_{\text{KL UB}} = - \sum_{i=1}^D \frac{\Pr(d_q(t) = d^{(i)}(t))}{T_{\text{sym}}} \log_2(\zeta_i). \tag{5.12}$$

Alternatively, because the complex multivariate Gaussian mixture considered in bounding the differential entropy is homoscedastic, the basic upper bound used in [73] reduces to the simple bound provided by the entropy of  $M$ -ary communications,

$$R_{M\text{-ary UB}} = - \sum_{m=1}^M \frac{\Pr(m_q = m)}{T_{\text{sym}}} \log_2 \Pr(m_q = m). \tag{5.13}$$

As SNR increases, it can be seen that the exponential within  $\zeta_i$  in Equation 5.12 goes to 0 and the bound on the rate increases to equate to the  $M$ -ary communications

bound when the number of possible displacements is equivalently the number of symbols. When this is not true,  $D > M$ , the KL upper bound,  $R_{KL\text{ UB}}$ , will become less tight than  $R_{M\text{-ary UB}}$ . For this reason, the full upper bound is written as

$$R_{UB} = \min\{R_{KL\text{ UB}}, R_{M\text{-ary UB}}\}. \quad (5.14)$$

For all cases, higher SNR will lead to using the  $M$ -ary upper bound over the KL-derived bound, but at what SNR this occurs is entirely dependent on the excitations used and transponder's impulse response. Regardless, once this  $M$ -ary upper bound is reached in VRBC, the only ways that the rate can be increased is by increasing the number of symbols used, decreasing the symbol length, using a different transponder, or better balancing the probabilities of the different symbols if they are not already equiprobable which may require better choices in the symbol excitations such that the multiple symbol data vectors are more orthogonal.

The upper bound presented in this section was used in Chapter 4, Fig. 4.9 (though it appears as a lower bound on error) and in the simulation examples given in Chapter 6.

## 5.2 VRBC System Trade-offs and Considerations

VRBC transponders should be designed with characteristics in mind

Throughout this dissertation, system trade-offs have been alluded to, but not entirely detailed. For VRBC implementation, however, these trade-offs require a formal description. In this section, three primary categories of required design considerations are looked at including

1. FMCW radar parameter choices,
2. transponder design choice,
3. and messaging scheme choices.

### 5.2.1 Radar Parameter Choices

Ultimately, choices in VRBC FMCW radar parameters are expected to be constrained in many applications of interest including anything-to-vehicle (X2V) communications. This comes from one of the benefits of VRBC being its ability to serve as an add-on communication scheme in systems where sensing is already being conducted. It is therefore necessary that VRBC not require much or any modification on the waveform being used if possible. So instead of approaching VRBC radar parameter choice as entirely free, we opt to look at the waveform parameters typically used in the applications of interest already.

Because the primary application of VRBC proposed in this dissertation is X2V, consider common mmW automotive radar waveforms. The TI IWR1443 mmW radar used in this dissertation operates at 77 GHz with 4 GHz of bandwidth because that is the exact RF band of frequencies allocated by the Federal Communications Commission (FCC) for automotive radar sensing. Fig. 5.1 shows this spectrum allocation. Of note, there exists a band at 5.85 GHz that was previously allocated for intelligent transportation systems (ITS). ITS is the umbrella term for connected vehicle solutions like X2V [74]. As shown in the figure, this band was declared open to all Wi-Fi devices in August of 2022.

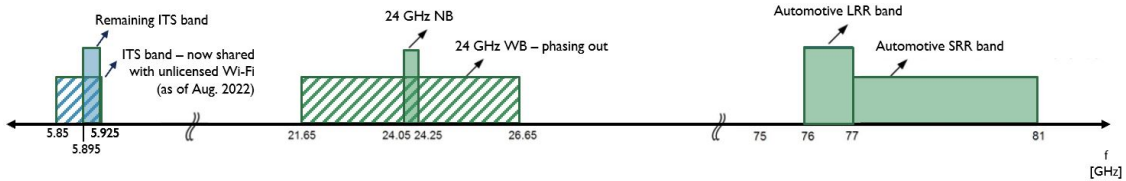


FIGURE 5.1: Millimeter-wave spectrum allocation in the U.S. as dictated by the FCC.

Because the operating frequency and bandwidth are regulated, it therefore makes sense to avoid analyzing whether 77–81 GHz is the ideal band of frequencies, though some of this was done in Chapter 2, and instead focus on the radar parameters that

can be modified to potentially aid in VRBC provided it allows the radar to sense as normal.

Fig. 5.2 shows an FMCW wave. From the diagram, it becomes clear that the variables to be considered are the chirp length,  $T$ , and pulse repetition interval (PRI),  $T_{\text{PRI}}$ .

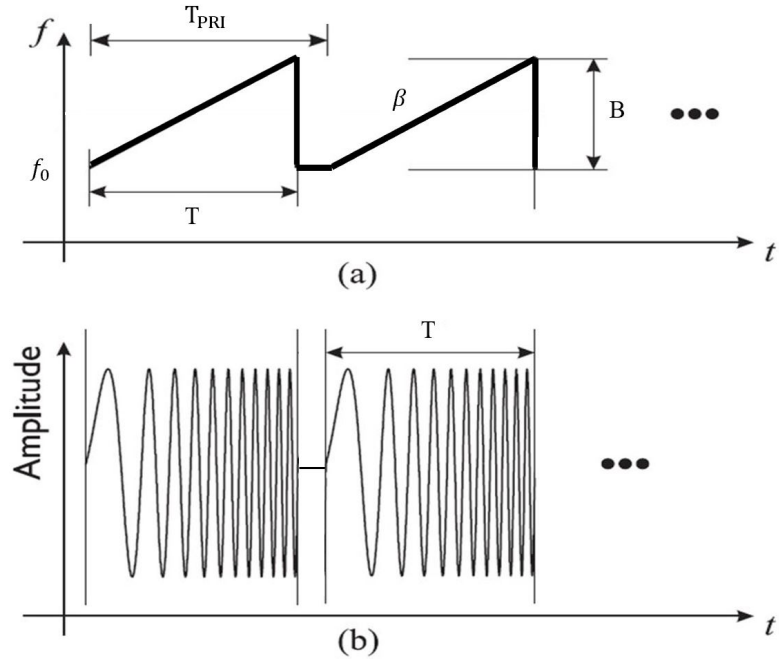


FIGURE 5.2: Illustration of FMCW waveform and its parameters.

The chirp length and PRI go hand in hand, as the radar hardware often comes with a limit for how close  $T$  and  $T_{\text{PRI}}$  can be. For the IWR1443, 7 microseconds is required between chirps when the full 4 GHz bandwidth is being utilized. Selecting a larger idle time, or duration between chirps, increases velocity resolution due to it consequently shortening the chirp length. However, this comes at the expense of the system's maximum velocity. For that reason, typically a short idle time is desired, while the the chirp length is decreased via shortening the full PRI.

Assuming the minimum idle time, the only parameter left to consider is the PRI. As already seen in following the VRBC processing chain in Chapter 4, a shorter

PRI, or higher pulse repetition frequency (PRF), leads to more samples for a given time. This means that for a given symbol duration in VRBC, a higher PRF will lead to more highly sampled data vectors for use in detection. Intuitively, this leads to a higher communication rate since more samples per symbol equates to more information relayed about the given symbol. The IWR1443 does limit the PRF to be  $< 10$  kHz when using the full 4 GHz bandwidth through its hardware limit on how steep the slope of the chirp can be.

Though the argument has been made that a higher PRF is desirable, more samples also results in longer processing times. For that reason, VRBC often does not aim to use the maximum PRF achievable. Rather, the choice in PRF is made by ensuring that all the vibrational frequencies of the system transponder can be distinctly recognized in Doppler. This means that the PRF must be greater than twice the maximum anticipated vibrational frequency per the Nyquist theorem. For the square foot aluminum plate in Chapter 4, Fig. 4.4 shows that a PRF of at least around 2 kHz is required. To improve detection with more samples, the choice in PRF in that collection was made to be 5 kHz.

### 5.2.2 Transponder Design Choices

A key element to developing a robust and desirable VRBC system is vibrational transponder design. Factors such as cost, size, power, reflectivity, noise pollution, and the ability to control the transponder's displacements directly all play a factor. If VRBC transponders are to appear on cars for X2V for instance, they need to be affordable, fit on a car, require minimal power for additional active components, provide adequate RF reflection at mmW such that they can be easily detected and decoded at potentially 100s of meters distance, cause minimal additional acoustic noise for the driver and nearby pedestrians, and be controllable so that VRBC symbols can be meaningfully designed and used.

Transponder size and reflectivity are directly related through the SNR of the VRBC signal via the radar range equation. Equation 2.4 shows that the variance of the transponder's gain/attenuation term is derived from the radar range equation. Because the signal model for the transponder return is the amplitude term multiplied by a complex exponential, Equation 2.4 can also be described as the transponder's return power. We can therefore write the return's signal-to-noise ratio (SNR) as the ratio of the variance of the target return gain/attenuation term,  $\tilde{\alpha}_{\text{tar}}$ , to the variance of the AWGN noise,

$$\text{SNR} = \frac{\mathbb{E}[|\tilde{\alpha}_{\text{tar}}|^2]}{\sigma_n^2}. \quad (5.15)$$

In the real data collection presented in Chapter 4, the TI IWR1443 radar has a peak receiver gain is  $\approx 48$  dB, transmit power is 12 dBm, system loss is 8 dB, and noise figure is  $\approx 15$  dB (resulting in thermal noise of about 0.65 pW). SNR can be calculated given this specific transponder. This calculation requires keeping in mind that atmospheric loss  $\approx 0.2$  dB/km. Because the transponder in this collection has a 12 in. (0.3 m)  $\times$  12 in. (0.3 m) aluminum plate surface, this scenario's return SNRs can be written in terms of range via

$$\text{SNR} \approx R \frac{(0.3^4)}{(4\pi r_{\text{obj}}^2)^2} 10^{(13.4 - 0.00002r_{\text{obj}})}. \quad (5.16)$$

This relationship was calculated using Equation 2.4 and recognizing that the surface RCS is  $\sigma_{\text{obj}} = 4\pi h^2 w^2 / \lambda^2$  for a fully reflective  $h \times w$  plate. The term  $R$  represents reflectivity, which for a polished aluminum surface can be as great as 0.98. In this radar/transponder scenario SNRs of  $[-10, -5, 0, 5, 10]$  dB end up corresponding to ranges of [335, 250, 188, 141, 106] meters. Naturally, these are maximum SNRs assuming the rectangular transponder's surface is perfectly perpendicular to the radar's main beam. If instead of a plate, a trihedral corner reflector were used to make the transponder's SNR less dependent on angular orientation, the same SNR

could be achieved when the corner reflector's edge length,  $l$ , is approximately 0.28 m,  $\sigma_{\text{obj}} = \frac{4\pi l^4}{3\lambda^2}$ .

To summarize, a good transponder design facilitates maximizing the RCS of the transponder surface while keeping its physical dimensions and weight practical for the application of interest, like a license plate on a vehicle for X2V. Making use of materials with high reflection coefficients also clearly helps. Though metal such as aluminum is highly reflective, allowing a metal plate transponder to be too thick can restrain vibrational displacement as it takes more power to displace anti-nodes on a thicker plate. As shown in Fig. 4.10 symbols consisting of primarily tones require at least around 100 micrometers for their vibrational displacement to have significant power at vibrational Doppler frequencies.

Optimal VRBC transponders require maximizing the number of symbols that can be used in the coding scheme. Because objects like the aluminum plate have distinct natural frequencies at which they resonant and produce larger displacements, we have limited ourselves to frequency shift keying (FSK). In the case of FSK, having multiple distinct and sufficient resonant frequencies would allow the system to increase the number of symbols it uses and therefore increase the communication rate. Having symbols at frequencies close to each other is also not desirable as it limits how short the symbol length can be since

$$\Delta f_D = \frac{1}{T_{\text{sym}}}. \quad (5.17)$$

where  $\Delta f_D$  is the frequency resolution in slow-time/Doppler.

With vibrations often comes sound. This is the fundamental idea behind loudspeakers where we purposefully displace a loudspeaker's diaphragm in hopes to produce certain acoustic waves. In VRBC, though, sound generation is not desirable. Towards achieving a quieter transponder, designs incorporating a vacuum seal of the vibrating surface in a radome through which the mmW can propagate become

attractive. When vacuum sealed system losses become limited to mainly material losses rather than acoustic radiation, allow the vibrational surface or even array of surface to conform to a variety of geometries while remaining virtually silent.

The final consideration of notable mention is the ability to control displacement. The data collection used in this dissertation has shown that though the displacement is linearly related to an excitation, extreme amounts of resonance are present. This comes from the fact that the surface of the aluminum plate transponder is free. It is not a piston-like movement where the instantaneous displacement is directly controllable. Certain sources of displacement, like piezoelectric actuator, could provide more control of the displacement signal, which in turn will lead to less intersymbol interference. Perfect control such that symbols like an ideal square wave can be achieved are not possible, but having more control over the transponder's displacement is nonetheless important.

### *5.2.3 Messaging Scheme Choices*

The design of the  $M$  vibrational displacement message signals used in VRBC is important to the system's performance. Priority considerations in symbol design include that

1. symbols be physically achievable by the transponder,
2. symbols result in minimal Doppler content at clutter-associated frequencies,
3. and symbol data vectors,  $\mathbf{a}^{(m)}$ , are as close to orthogonal as possible.

The first two of these considerations have been discussed in the previous section and Chapter 4-Section 4.4.3 respectively. The third point refers to minimizing errors caused from different symbol data vector,  $\mathbf{a}^{(m)}$ , being similar, or mathematically not orthogonal.

To justify the preference for symbols resulting in orthogonal clutter-free, noise-free data vectors, Fig. 5.3 shows simulation results for the probability of symbol classification error of two different  $M = 4$  symbol sets. One set corresponds to orthogonal data vectors and one not. Designing vibrational displacement message signals,  $d^{(i)}(t)$ 's, that result in orthogonal data vectors is difficult in practice. The most common way of creating orthogonal complex exponential data vectors is to choose linear message signals that create orthogonal complex frequencies. To approach orthogonality through linear message signals, first consider the data vectors assuming that no bulk motion without loss of generality,

$$\mathbf{a}^{(i)} = \tilde{\alpha}_{\text{tar}} e^{j \frac{4\pi}{\lambda_0} d(\mathbf{t})} \sum_{g=0}^{G-1} z_{\text{tar}}(\mathbf{t} - gT_{\text{PRI}}) \text{ for } \mathbf{t} = \left[ \frac{1}{f_s}, \frac{1}{f_s}, \dots, \frac{L_{\text{sym}}}{f_s} \right]^T \quad (5.18)$$

where

$$z_{\text{tar}}(t) = \begin{cases} e^{j4\pi\beta\left(\frac{(r+d(t))t}{c} - \frac{(r+d(t))^2}{c^2}\right)} & 0 \leq t < T \\ 0 & \text{otherwise} \end{cases}. \quad (5.19)$$

Assuming that the VRBC symbol length is an integer multiple of the PRI and that the portion of the signal specific to the chirp waveform is minimally affected by  $d(t)$ , only the slow-time signals across chirps need to be considered. In other words, using the fact the  $z_{\text{tar}}(t)$  is primarily a function of  $r$  rather than  $r + d(t)$ , we can assume that this component is the same for all possible data vectors. The task at hand then becomes making

$$\left\langle \tilde{\alpha}_{\text{tar}} e^{j \frac{4\pi}{\lambda_0} d^{(i)}(\mathbf{t})}, \tilde{\alpha}_{\text{tar}} e^{j \frac{4\pi}{\lambda_0} d^{(i')(\mathbf{t})}} \right\rangle = 0 \quad \forall i \text{ and } i' \neq i \in D. \quad (5.20)$$

Let  $\langle \cdot \rangle$  be the inner product operation. Because it is known that

$$\langle e^{j2\pi f_1 t}, e^{j2\pi f_2 t} \rangle = \int_0^{T_{\text{sym}}} e^{j2\pi f_1 t} e^{-j2\pi f_2 t} dt = 0 \quad \forall f_1 - f_2 = \frac{m}{T_{\text{sym}}} \text{ where } m \in \mathbb{Z}, \quad (5.21)$$

it can be seen that  $\frac{2d(t)}{\lambda_0}$  must equal  $\frac{m}{T_{\text{sym}}}$ , and therefore  $d(t) = \frac{\lambda_0 m}{2T_{\text{sym}}}$ . Achieving these desired slopes exactly in the message signal, unfortunately, requires precise transponder calibration in practice.

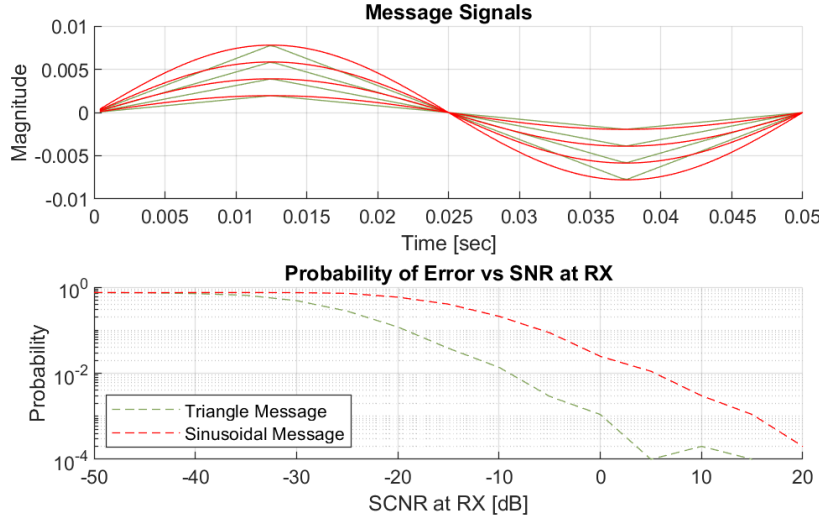


FIGURE 5.3: In one set the displacements,  $d_i(t)$ 's, are triangle wave symbols which provide orthogonal data vectors. In the other, they are sinusoidal symbols which do not provide orthogonal data vectors.

In addition to the amplitude precision needed for theoretical triangle wave vibrational displacement symbols, recall that these symbols must be physically achievable. Symbol signal choices such as triangle waves are not entirely achievable on a real vibrating surface as they have non-differentiable points. The aluminum plate transponder, for example, is unable to displace its surface suddenly in a different direction aside from its resonant effects. Sinusoidal vibrational displacement symbols are much easier to produce, and so they have been the symbol design of choice thus far.

As shown in both simulation and a real data collection, VRBC does not require symbol design to be perfect in order for it to operate successfully. Rather, it becomes an optimization problem where higher data rates at longer ranges can be achieved

when symbol design and transponder design are done in ways that better satisfies the criteria that has been outlined.

# 6

## Application-Motivated Methods for VRBC

Working with real data often brings up unforeseen challenges. Some of the challenges in implementing a VRBC system have already been presented within this dissertation, while others have gone undetected thus far. In this chapter, sections are designated to specifically addressing some of the challenges of implementing VRBC. These include accounting for significant resonance in the VRBC transponding surface, more optimally performing clutter filtering, and then mitigating both radar platform and target platform vibration noise.

### 6.1 VRBC Using Resonant Transponding Surfaces

As was done in Chapter 4, continue to assume  $M$  excitation symbols comprising a VRBC sequence of  $Q$  symbols long,

$$x_{\text{seq}}(t) = \sum_{q=1}^Q x_q(t - (q - 1)T_{\text{sym}}) \quad (6.1)$$

where each  $x_q(t) \in \mathcal{X}$  and  $\mathcal{X} = \{x^{(1)}(t), x^{(2)}(t), \dots, x^{(M)}(t)\}$ . Continue to assume that the excitation length for all  $M$  possible symbols is  $T_{\text{sym}}$  seconds. Once again, because

the vibrating surface is modeled as an LTI system, the vibrational displacement is

$$d(t) = \sum_{q=1}^Q d_q(t - (q-1)T_{\text{sym}}) \quad (6.2)$$

where

$$d_q(t) = \sum_{n=0}^{q-1} x_{q-n}(t - nT_{\text{sym}}) \otimes h(t). \quad (6.3)$$

Instead of ignoring the resonant effects of  $d_q(t)$ , we recognize now that  $d_q(t) \in \mathcal{D} = \{d_q^{(1)}(t), d_q^{(2)}(t), \dots, d_q^{(D)}(t)\}$  where  $D \neq M$ . The set of displacements is now specifically larger than the set of excitation because convolving the sequence excitation signal with the system's impulse response results in symbol interval displacements that are different even when the same excitation symbol is present with that interval.

By substituting this version of the displacement signal into the clutter filtered and synchronized return (4.19), the VRBC channel can still be described in the same way it was previously. Specifically,

$$y(t) = \sum_{q=1}^Q y_q(t - (q-1)T_{\text{sym}}), \quad (6.4)$$

where

$$y_q(t) = y_{q,\text{tar}}(t) + \tilde{\eta}(t). \quad (6.5)$$

and  $y_{q,\text{tar}}(t) \in \mathcal{Y}_q = \{y_{q,\text{tar}}^{(1)}(t), y_{q,\text{tar}}^{(2)}(t), \dots, y_{q,\text{tar}}^{(D)}(t)\}$ . Once again,  $y_{q,\text{tar}}^{(d)}(t) = y_{\text{tar}}(t)$  given  $d(t) = d^{(D)}(t)$ .

The set of displacements  $D$  and therefore cardinality of  $\mathcal{Y}_q$  is made larger than  $M$  by the presence of intersymbol interference (ISI), as mentioned. In mitigating ISI, it is also common to make use of line coding constraints that avoid error-prone patterns from occurring in a message sequence. To improve system performance when significant ISI or coding constraints are present, a VRBC sequence Markov model must

be derived. It is the Markov model that allows for sequence detection, rather than single symbol detection, to be conducted. Though resonant transponding surfaces result in ISI, it needs to be recognized that resonant surfaces can be favorable, as they often lead to larger maximum displacements, which puts more of the power due to vibrations existing at frequencies outside of clutter-specific Doppler frequencies, see Chapter 5.

In general, the observed vibrational displacement for the  $q^{\text{th}}$  symbol interval can be estimated using the interference from a finite number of previous symbols rather than all the previous symbols as described in Equation 6.3. Let

$$d_q(t) = \sum_{n=0}^{N_q} x_{q-n}(t - nT_{\text{sym}}) \otimes h(t) \quad (6.6)$$

for  $0 \leq t < T_{\text{sym}}$  and 0 otherwise. Here,  $N_q$  is the number of symbols previous whose vibrational transients interfere with the current symbol's vibrational displacement. This model assumes that for the  $q^{\text{th}}$  symbol interval that all vibrations due to symbols prior to the  $(q - N_q)^{\text{th}}$  symbol have decayed to a negligible amount.

Picking  $N_q$  is not required to be done in a particular way. For instance, visualizations like the slices of the sliding window MSC in Fig. 4.14 can be useful for understanding how long a particular vibrational frequency may require to decay out. Alternatively, it is often useful to instead approach choices in  $N_q$  by considering the full resonant displacements of each symbol excitation,  $x^{(m)}(t) \otimes h(t)$ , and implementing some constraint on what defines a negligible amount of displacement. In this dissertation, we define a negligible amount of interfering displacement as displacement with a magnitude less than a chosen ratio of the maximum absolute displacement provided by any of the  $M$  symbol excitations. This ratio is defined as  $\gamma_{\min}$ . Additionally in this dissertation,  $\gamma_{\min}$  is permitted to require a different number of symbol intervals for which it takes each of the  $M$  symbol excitations to decay out

to the defined negligible amount. The set  $\mathcal{N}$  is used to describe the system's symbol-specific resonances,  $\mathcal{N} = \{N^{(1)}, N^{(2)}, \dots, N^{(M)}\}$ , where element  $N^{(m)}$  describes the number of symbol intervals it takes the  $m^{\text{th}}$  symbol to decay to  $\gamma_{\min} \max_{t,m} d^{(m)}(t)$ .

The choice in  $\gamma_{\min}$  does affect detection performance. If  $\gamma_{\min}$  is too large, then detection performance degrades as the interference present becomes inaccurately represented. Alternatively, choosing a smaller  $\gamma_{\min}$  will create a more accurate representation but will also increase the model complexity and eventually provide no additional performance benefits in sequence detection over single symbol detection. If  $\gamma_{\min}$  is chosen such that symbols of similar transients are treated differently, like barely dictating that one symbol requires another interval of ISI to be modeled while another barely does not, can lead to unfavorable performance in final sequence detection. All of this is to say that choices in modeling ISI should be made mindfully.

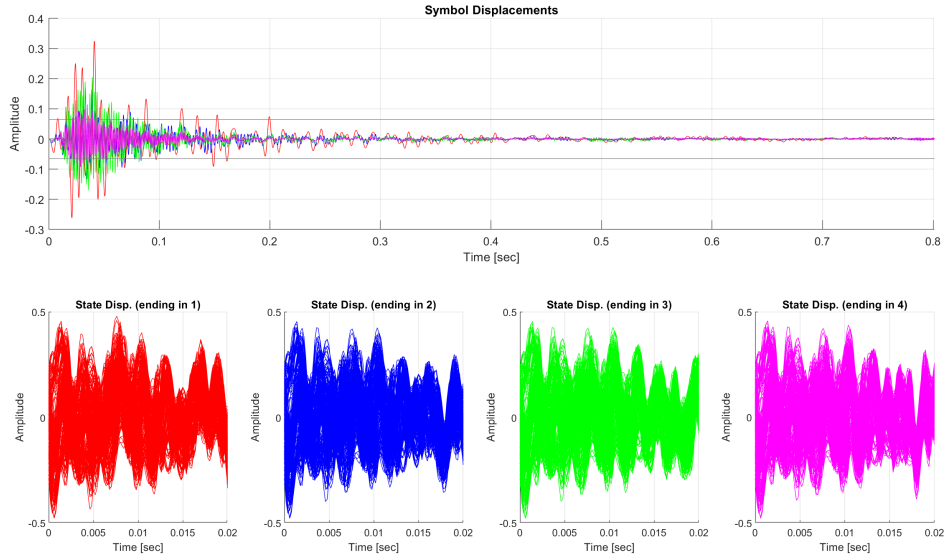


FIGURE 6.1: These were estimated using known excitation signals (tones at 150, 350, 450, and 750 Hz) and the transponder's impulse response estimate.

The top of Fig. 6.1 shows the full length displacement estimates for the symbol excitation set  $\mathcal{X}$  for the real data collection in this dissertation. In this case,

$\mathcal{X} = \{\sin(2\pi[150, 350, 450, 750]t)\}$  for a given symbol interval. Symbol length in this collection was 20 ms as shown by the x-axis on the bottom subplots. Additionally shown are boundaries for an arbitrarily chosen  $\gamma_{\min}$  of 0.2. Due to this surface's extreme resonance, a maximum  $N^{(m)}$  of 4 was set so that the number states did not grow too large. The resulting  $\mathcal{N}$  was then  $\{4, 4, 4, 2\}$ . The bottom subplots in Fig. 6.1 displays the set of possible symbol interval displacements  $\mathcal{D}$  that result from not only from accounting for the current symbol excitation but previous symbol's that interfere with the current interval.

Towards formally defining a VRBC sequence Markov model, states and transition events need defined. States and transition events are used to describe how an observation depends on previous observations. In VRBC, ISI and coding constraints dictate the possible observations a given symbol interval can have. Let

$$d_q(t) - (x_q(t) \otimes h(t)) \in \mathcal{D}_{\text{ISI}}. \quad (6.7)$$

define the ISI of the  $q^{\text{th}}$  symbol interval where  $\mathcal{D}_{\text{ISI}}$  is the set of possible ISI displacements and has a cardinality of  $S$  to stand for the number of VRBC states. The set of possible ISI conditions/states can be found by considering all symbol sequence permutations of the  $M$  symbols of length  $\max(\mathcal{N})$  or less. Coding constraints and a non-uniform  $\mathcal{N}$  can lead to certain permutations being unachievable or unnecessary to define distinctly.

Now,  $y_q(t)$  is independent of  $y_{q-i}(t)$  given  $y_{q-1}(t)$  for  $i > 1$  since no interval's displacement can be dependent on more than the previous when the previous is defined on ISI that is only further decaying out and remaining negligible in the current interval. Transition events for a VRBC Markov model are then described by the symbol excitation of the current interval as it is the new symbol that defines what the ISI will look like in the next symbol interval, ie. what state must be transitioned to.

It is insufficient to describe states and transition events alone. Their transition probabilities must also be fully described in order for detection to benefit from this model. Transition probabilities are found using knowledge of the state definitions and any line coding constraints. Examples will be shown to further demonstrate how this is done exactly, but once defined, the transition probabilities are put into a state transition matrix  $\mathbf{A}$ , within which element  $A_{i,j}$  describes the probability of transitioning from state  $i$  to state  $j$ .

Using the notation that  $m_q$  and  $s_q$  are the  $q^{\text{th}}$  symbol and state in a VRBC sequence where  $m_q \in 1, 2, \dots, M$  and  $s_q \in 1, 2, \dots, S$ , a summary of the Markov model description can be given as:

- states: defined by the ISI present within a symbol interval
- transition event: defined by any new symbol in a sequence
- Markov property:  $\Pr(s_q | s_1, s_2, \dots, s_{q-1}) = \Pr(s_q | s_{q-1})$
- transition matrix:  $A_{i,j} = \Pr(s_q = j | s_{q-1} = i)$

**Example 1.** Resonant Surface Case: Instead of considering the real data example because it leads to 261 distinct states and made use of no coding constraints, consider an alternative case. In this example,  $M = 3$  and we assume that all symbols produce non-negligible amounts of ISI for at least one symbol interval,  $\min(\mathcal{N}) \geq 1$ . Specifically, we use  $\mathcal{N} = \{2, 1, 1\}$ . Consequently, we also adopt a simple coding constraint in which consecutive symbols are not possible,  $m_q \neq m_{q-1}$ , as to attempt to mitigate the errors caused by previous symbol ISI. Furthermore, consider any symbol interval to have equally probable chances of being any of the  $M$  symbols besides for whatever the previous symbol was,  $\Pr(m_q = m) = \frac{1}{M-1}$  for all  $m \neq m_{q-1}$ .

When no coding scheme is invoked, the possible states are described by the full list of possible sequences of the  $M$  symbols that are of length  $\max(\mathcal{N})$  or less. These

Table 6.1: States for  $M = 3$  and  $\mathcal{N} = \{2, 1, 1\}$

State Index	Sequences
1	- -
2	- 1
3	- 2
4	- 3
	1 1
5	1 2
6	1 3
	2 1 → - 1
	2 2 → - 2
	2 3 → - 3
	3 1 → - 1
	3 2 → - 2
	3 3 → - 3

sequences are described in the rows of Table 6.1. The sequences in the table are formatted such that reading the symbol sequences left to right goes from the most previous contributing symbol interval's excitation to the most recent symbol interval's excitation, i.e. the  $(q - \max(\mathcal{N}))^{\text{th}}$  to the  $(q - 1)^{\text{th}}$  symbol interval.

After all possible states are generated, instances in which symbol excitations would no longer contribute ISI to the current symbol interval's displacement were replaced with the no-contribution symbol, often leading to duplicates of an existing state allowing for a state elimination. This replacement is shown via the “ $\rightarrow$ ” in Table 6.1. For example the sequences of “2 1” became “- 1” because  $N^{(2)} = 1$  and therefore would not contribute ISI in the  $q - 2^{\text{th}}$  position. Lastly, using our basic coding scheme of avoiding consecutive symbols requires that states violating this constraint be eliminated. The sequence of “1 1” exemplifies this. The states that remain in the  $M = 3$  and  $\mathcal{N} = \{2, 1, 1\}$  example are those indexed in Table 6.1.

For this example, the transition matrix is

$$\mathbf{A} = \begin{bmatrix} 0 & \frac{1}{3} & \frac{1}{3} & \frac{1}{3} & 0 & 0 \\ 0 & 0 & 0 & 0 & \frac{1}{2} & \frac{1}{2} \\ 0 & \frac{1}{2} & 0 & \frac{1}{2} & 0 & 0 \\ 0 & \frac{1}{2} & \frac{1}{2} & 0 & 0 & 0 \\ 0 & \frac{1}{2} & 0 & \frac{1}{2} & 0 & 0 \\ 0 & \frac{1}{2} & \frac{1}{2} & 0 & 0 & 0 \end{bmatrix} \quad (6.8)$$

when a coding scheme constraining consecutive symbols is implemented and all remaining symbols are equiprobable. As this matrix shows, the beginning state of no-ISI is unachievable at any point in the sequence besides for the start since this example assumed all symbols produce non-negligible amounts of ISI for at least one symbol interval. We also see that states 5 and 6 are the only two that require considering more than the previous symbol in the sequence and can only be reached via a state where ‘1’ was the previous symbol, ie. state 2.

The labor of finding the set of states and transition matrix can naturally be automated. This is naturally what was done for the real data.

Once put into a Markov model, VRBC detection can be completed using sequence maximum likelihood detection methods. Recall that VRBC follows

$$\text{Input Symbol } m_q \xrightarrow{\text{Channel}} \text{Output Signal } \mathbf{y}_q \xrightarrow{\text{Detection}} \text{Predicted Symbol } \hat{m}_q . \quad (6.9)$$

The symbol interval return signals  $y_q(t)$  comprise of the target-derived component,  $\mathbf{a}_q$ , and band-limited AWGN samples,  $\boldsymbol{\eta}_q$ . This can be written as

$$\mathbf{y}_q = \mathbf{a}_q + \boldsymbol{\eta}_q . \quad (6.10)$$

This now differs from the previous detection method in that the possible target-derived data vectors are denoted as  $\mathbf{a}^{(s,m)}$ , indicating it results from ISI displacement associated with state  $s$  and current symbol displacement associated with the  $m^{\text{th}}$  symbol.

To perform sequence estimation, which we do via the Viterbi algorithm, we define the posterior probabilities,  $\Pr(s_q = s | \mathbf{y}_q)$  using Bayes' theorem,

$$\begin{aligned}\Pr(s_q = s | \mathbf{y}_q) &= \frac{f(\mathbf{y}_q | s_q = s) \Pr(s_q = s)}{f(\mathbf{y}_q)} \\ &= \frac{l_s(\mathbf{y}_q)}{\sum_{t=1}^S l_t(\mathbf{y}_q)},\end{aligned}\tag{6.11}$$

where

$$l_s(\mathbf{y}_q) = \sum_{m \in \mathcal{M}^{(s)}} \frac{\Pr(s_q = s)}{|\mathcal{M}^{(s)}|} e^{-\frac{1}{2}(\mathbf{y}_q - \mathbf{a}^{(s,m)})^H \Gamma^{-1} (\mathbf{y}_q - \mathbf{a}^{(s,m)})},\tag{6.12}$$

and  $\mathcal{M}^{(s)}$  is the set of possible current symbols that can occur when in state  $s$ .

Equation 6.11 is found by acknowledging that given a particular state, the output vector has a complex multivariate Gaussian mixture probability density function of,

$$f(\mathbf{y}_q | s_q = s) = \sum_{m \in \mathcal{M}^{(s)}} \frac{1}{|\mathcal{M}^{(s)}|} \tilde{\mathcal{N}}(\mathbf{a}^{(s,m)}, \Gamma)\tag{6.13}$$

for a single channel use. If the input state is not known, the distribution of the output data vector is the weighted sum of those state-conditioned densities,

$$f(\mathbf{y}_q) = \sum_{s=1}^S \Pr(s_q = s) f(\mathbf{y}_q | s_q = s).\tag{6.14}$$

The probability of being in a state during a particular symbol interval,  $\Pr(s_q = s)$ , is found recursively using the state transition matrix,

$$\boldsymbol{\pi}_q = \boldsymbol{\pi}_{q-1} \mathbf{A},\tag{6.15}$$

where  $\boldsymbol{\pi}_q$  is the column vector describing the probabilities of each state occurring at the  $q^{\text{th}}$  symbol interval, ie.  $\boldsymbol{\pi}_q = [\Pr(s_q = 1), \Pr(s_q = 2), \dots, \Pr(s_q = S)]^T$ . Naturally,  $\boldsymbol{\pi}_0 = [1, 0, 0, \dots, 0]^T$  in all cases assuming the first state is always defined as the state where no previous or current symbol excitations contribute to displacement.

In carrying out the Viterbi algorithm, two matrices are calculated for each symbol interval and state combination. These calculations fully describe the standard Viterbi trellis. Define the  $S \times Q$  matrices

$$T_1[s, q] = \max_t (T_1[t, q-1] A_{t,s} \Pr(s_q = s | \mathbf{y}_q)) \quad (6.16)$$

and

$$T_2[s, q] = \arg \max_t (T_1[t, q-1] A_{t,s} \Pr(s_q = s | \mathbf{y}_q)). \quad (6.17)$$

$T_1$  tracks the probability associated with the most likely path leading to the current symbol interval's state being state  $s$ .  $T_2$  tracks the previous symbol interval's state prediction associated with the most likely path leading to the current symbol interval's state being state  $s$ .

To decide the final sequence observed, the last state detected is found by considering  $\arg \max_t (T_1[t, Q])$ . Once the sequence of states is found by recursively considering  $\hat{s}_q = T_2[\hat{s}_{q+1}, q+1]$ , the predicted symbol sequence can easily be found by considering what transition events led (or could have led) to the sequence of predicted states. The phrase “could have led” alludes to the case where  $\min(\mathcal{N}) < 1$ . In these cases, single symbol maximum likelihood detection is needed to decide between multiple potential transition events.

For the real data collection processed in this Chapter 4, a visual of the detection results using single symbol maximum likelihood detection, maximum likelihood detection on the various state definitions, and then full sequence detection using the Viterbi algorithm are shown in Fig. 6.2. The confusion matrix when using the Viterbi algorithm for sequence detection on the real data set is also provided in Table 6.2

Fig. 6.2 provides evidence as to how resonant transponding VRBC surfaces such as the square foot aluminum transponder benefit greatly from sequence detection versus single symbol detection even if all the ISI is not able to be accounted for (in

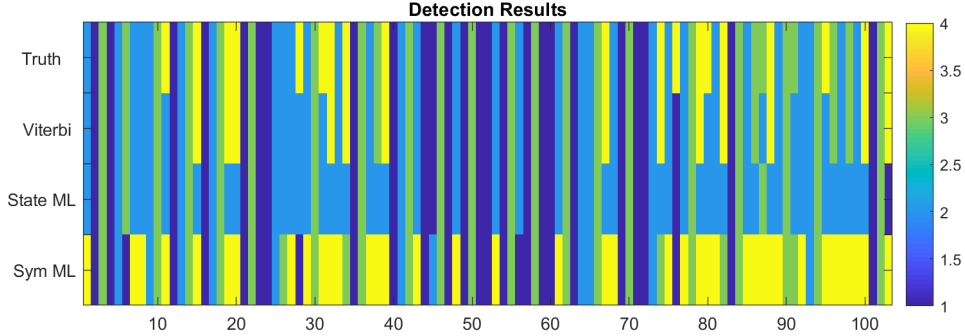


FIGURE 6.2: The detection results for the real data collection of the square foot aluminum transponder.

Table 6.2: Confusion Matrix for Viterbi Sequence Detection on the Real Data Collection

True Symbol	Detected Symbol			
	150 Hz	350 Hz	450 Hz	750 Hz
150 Hz	25	0	0	0
350 Hz	0	32	0	0
450 Hz	0	2	25	0
750 Hz	1	5	3	13

reference to setting a cap on  $N^{(m)}$  of 4). In this example, measured rate increased from 48.7 bits per second to 80.0 bits per second.

To build a stronger understanding of when sequence detection proves worthwhile, we now simulate a scenario in which  $M = 3$  to demonstrate key discussion points of VRBC operation. These simulations assume a PRF = 4 kHz, symbol length of  $T_{\text{sym}} = 5$  ms, ADC sampling frequency of 1 MHz, and therefore an  $L_{\text{sym}} = 5000$ . An arbitrary single set of  $M = 3$  frequency shift-keying symbol excitations are considered. They consist each of a tone at 800, 600, and 400 Hz respectively.

Signal to noise ratio (SNR) as was defined in Chapter 5 is used here to generate rate vs SNR plots. The simulation assumes a radar similar to the TI IWRR1443 where the peak receiver gain is  $\approx 48$  dB, transmit power is 12 dBm, system loss is 8 dB, and noise figure is  $\approx 15$  dB (resulting in thermal noise of about 0.65 pW). In opposition to the real data collection, the simulation considers a 6 in. (0.15 m)  $\times$  12

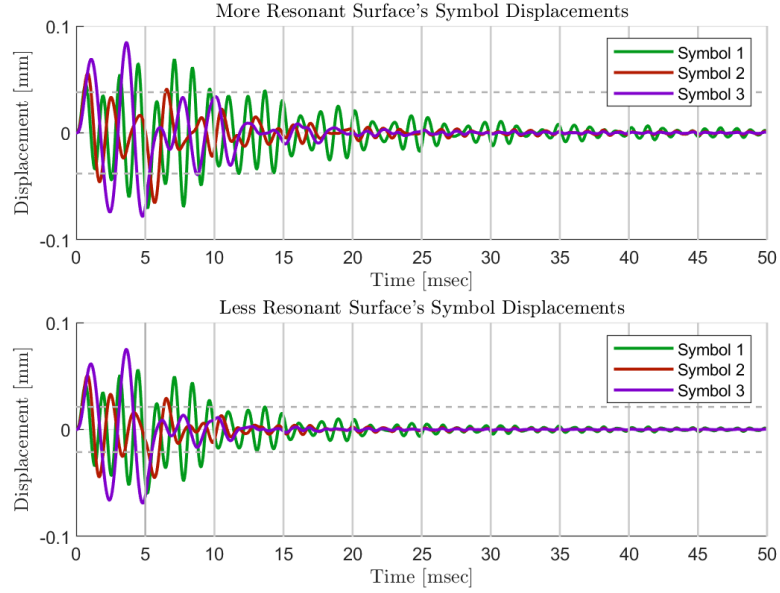


FIGURE 6.3: Solid gray vertical lines indicate symbol interval boundaries, while dashed gray horizontal lines indicate the transponder’s  $\gamma_{\min}$  boundaries.

in. (0.3 m) fully reflective license plate transponder surface due to VRBC’s potential in X2V.

Throughout these simulations Monte Carlo results for the communication rate are compared to the theoretical upper bound provided in Chapter 5 (blue). The simulated experimental results include when the detection methods used are symbol maximum likelihood detection (yellow), and the Viterbi algorithm on the states (teal). 100 iterations of 50-length sequences were used at each SNR for Monte Carlo results.

#### 6.1.1 Considering Varying Levels of Transponder Resonance

Consider two impulse responses consisting of a sum of decaying sinusoids at resonant frequencies measured from an aluminum plate. The impulse responses differ only in the decay factor of the various resonant frequencies to demonstrate the importance of recognizing the degree of resonance present in a VRBC surface of interest when

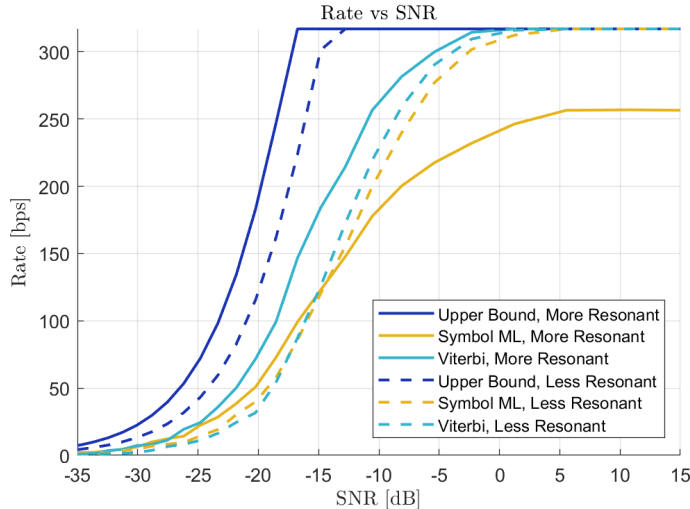


FIGURE 6.4: Both scenarios use the set  $\mathcal{N} = \{2, 1, 1\}$  to describe how many intervals each symbol requires to decay to a negligible amount and a no-consecutive symbols constraint.

choosing what detection method should be used. The first impulse response corresponds to the surface that is more resonant and therefore contains the most ISI. The second is less resonant. Fig. 6.3 shows the symbol displacements over multiple symbol intervals for the two scenarios. Due to the variation in resonances,  $\gamma_{\min}$  is adjusted such that system's symbol-specific resonances come out to  $\mathcal{N} = \{2, 1, 1\}$  for both cases. This allows the comparison between these two cases to highlight when sequence versus symbol detection is preferable.

For the more resonant surface, a  $\gamma_{\min} = 0.45$  is used (solid). In other words, the requirement for considering ISI negligible is relatively relaxed. For the second case,  $\gamma_{\min} = 0.25$  (dashed). A no-consecutive symbol coding constraint is used for both cases. Fig. 6.4 shows the surfaces' resultant communication rates.

These two examples demonstrate that the added complexity of implementing sequence detection does not always lead to a significant increase in performance. According to Fig. 6.4, when the transponder is more resonant, the Viterbi algorithm does prove to increase the rate achieved significantly. Fig. 6.4 also shows that se-

quence detection can provide a slight increase in performance for a less resonant transponder. As shown, sequence detection comes at the cost of additional modeling and computational power, which may in turn make sequence detection undesirable for less resonant surfaces. Though not shown, it is possible to inaccurately model ISI like setting  $\gamma_{\min}$  such that one symbol barely requires an additional interval to decay while the others barely do not. Doing so can lead to worse sequence detection performance as it results in invoking inaccurate symbol interval dependencies. For this reason, we focus on cases where ISI modeling utilizes a significant  $\gamma_{\min}$ , ie. greater than about 0.1, and we have checked that the symbol displacements do not appear to provide borderline ISI requirements.

One final observation from the results of transponders at different levels of resonance is that ISI can cause the  $M$ -ary upper bound to be unachievable by either detection methods. Though we only show a case for single symbol detection not achieving the upper bound the same reasoning could apply to sequence detection if ISI is inaccurately modeled. For the more resonant surface's single symbol detection results, ISI is so great that certain sequences will always result in incorrect detections even when there is no noise present, see the solid yellow line in Fig. 6.4. These cases can be understood by considering when a previous symbol provides larger enough interference that it will mask the current symbol. In trying to design VRBC systems that achieve the  $M$ -ary upper bound at high SNRs, symbol-specific data vectors must be made orthogonal and have similar decay rates.

### 6.1.2 Considering Various Communication Message Constraints

We now consider how coding constraints affect our choice in detection method. Thus far, we have adopted the no-consecutive symbol constraint. We now vary this and consider coding constraints that are based on the resonances of the VRBC transponder. In aiming to align a coding constraint with the characteristics of the system,

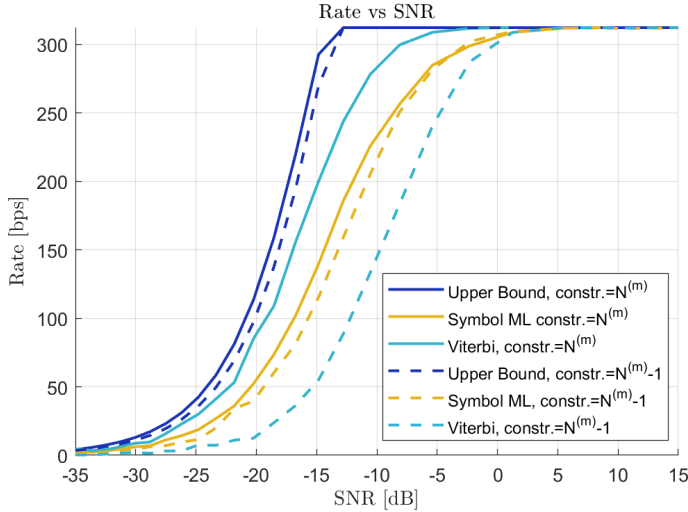


FIGURE 6.5: Specifically,  $\mathcal{N} = \{2, 1, 1\}$  and the coding constraint used requires either  $N^{(m)}$  intervals (solid) or  $N^{(m)} - 1$  intervals (dashed) between consecutive symbols.

begin by considering the less resonant surface we just presented where  $\mathcal{N} = \{2, 1, 1\}$ . Now, require symbols to be separated in accordance with  $\mathcal{N}$ . In other words, consecutive  $m$ -symbols must have at least  $N^{(m)}$  intervals between them (solid). We also consider if this was relaxed to  $N^{(m)} - 1$  intervals between consecutive symbols (dashed). Simulating a coding constraint that is more restrictive than  $\mathcal{N}$ , such as requiring  $N^{(m)} + 1$  intervals between consecutive symbols, is not possible in this case. It would lead to the set of available symbols at certain intervals being empty due to the need for previous symbols to decay further before reuse. Fig. 6.5 shows the results for the two coding constraints described.

Since the ultimate goal of communication systems is to achieve larger rates, we find that the best performance coincides with having coding constraints and ISI modeling align. This can be seen as when the  $N^{(m)}$  constraint is used in combination with sequence detection. Fig. 6.4 also shows that when modeling ISI to a larger degree than what the coding constraint is handling, like in the  $N^{(m)} - 1$  constraint, single symbol detection can become a better choice for detection. To achieve rates closer to

the upper bound in VRBC, we therefore recommend aligning line coding constraints with the resonances of the surface in order to benefit most from sequence detection.

## 6.2 Towards Ideal Clutter Filtering

In Chapter 4, it was revealed that traditional clutter filtering through the use of a notch filter in slow-time at the frequencies associated with the clutter ridge negatively affects the transponder-derived return. It was mentioned that one important concern was that the phase of the resulting signal can become distorted and therefore not usable for synchronization and impulse response estimation. To begin, recall the approximate slow-time signal prior to clutter filtering at the transponder's range bin

$$y(t, m, \theta) \approx \tilde{\alpha}_{\text{tar}} e^{j2\pi f_0 \tau_{\text{tar}}(t, m)} + \sum_{k=1}^{K_{r_m, \theta}(t)} \tilde{\alpha}_k e^{j2\pi f_0 \tau_k(t, m)} + \tilde{n}(t). \quad (6.18)$$

Without loss of generality, assume that bulk radar platform movement has been accounted for and the clutter is therefore stationary and exists at 0 Hz Doppler,

$$y(t, m, \theta) = \underbrace{\tilde{\alpha}_{\text{tar}} e^{j\frac{4\pi}{\lambda_0} (v_{\text{tar}} t + d(t))}}_{\substack{\text{Target-Derived Component} \\ \cdot \text{constant amplitude} \\ \cdot \text{time-varying phase}}} + \underbrace{\tilde{\alpha}_{\text{clt}}}_{\substack{\text{Clutter} \\ \cdot \text{constant amplitude} \\ \cdot \text{constant phase}}} + \underbrace{\tilde{n}(t)}_{\substack{\text{AWGN} \\ \cdot \text{time-varying amplitude} \\ \cdot \text{time-varying phase}}}. \quad (6.19)$$

Bulk radar platform movement can easily be adjusted for by multiplying Equation 6.18 by  $e^{j\frac{4\pi}{\lambda_0} v_{\text{radar}}}$ .

Now consider the phasor diagrams in Fig. 6.6. Subfigure (a) shows Equation 6.19 when  $\frac{4\pi}{\lambda_0} d(t)$  has a range of at least  $2\pi$ . This phasor description is similar to the traditional frequency modulation (FM) phasor diagram. The clutter-derived component takes the form of an FM signal's carrier signal, while the transponder-derived component corresponds closely to the conventional modulation signal. For that reason, we adopt similar terminology in describing these phasor diagrams. The plot (a) relates to when  $\frac{4\pi}{\lambda_0} \max |d(t)| > 2\pi$ , while (b) in Fig. 6.6 equates to its "narrowband"

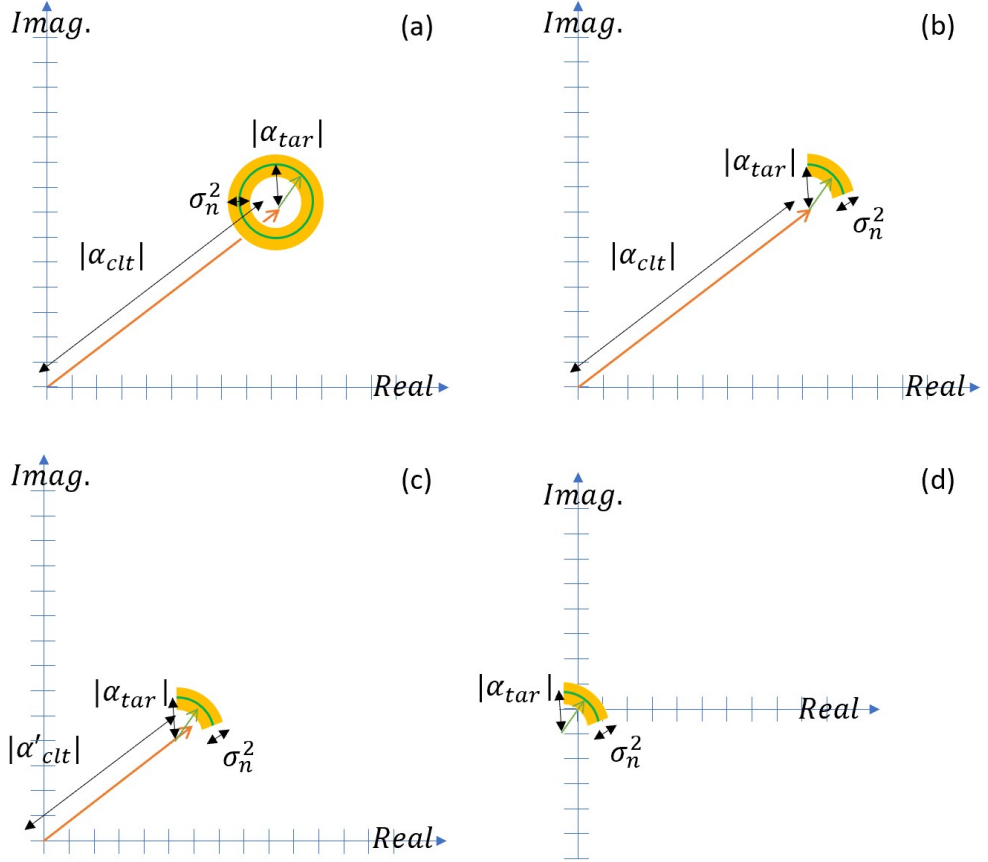


FIGURE 6.6: Phasor diagrams in consideration for clutter filtering.

counterpart, ie  $\frac{4\pi}{\lambda_0} \max |d(t)| < 2\pi$ . In the case of mmW vibrometry, narrowband behavior in this sense is expected because the span of  $\frac{4\pi}{\lambda_0} d(t)$  is often much less than  $2\pi$ . This equates to  $d(t) < 2$  mm. One unique feature to the phasor diagram for mmW vibrometry is that the transponder platform velocity,  $v_{tar}$ , would appear as an additional rotation of the arc around the end of the clutter phasor at a rate of  $\frac{4\pi}{\lambda_0} v_{tar}$  radians per second.

Conventional clutter notch filters work by minimizing the offset seen in the phasor diagram. Subfigures (c) and (d) demonstrate the progression from using a shallow notch clutter filter to a deep notch clutter filter. There exists an amount of clutter filtering between (c) and (d) for which the offset equates to the magnitude of the

target-derived component. This would be the ideal clutter filter because even though it would still affect the target-derived term, the remaining DC component can be considered the DC component for the target-derived component. Whether the offset originates from the target or clutter is not important. If the resulting phasor resemble that of the target signal, we can claim that the clutter filter did not modify the target-derived component.

Naturally, if the AWGN noise variance,  $\sigma_n^2$ , is larger than the magnitude of the transponder, performance will not be ideal when the ideal clutter filter is used. This implication is conventionally known as a benefit of narrowband phase modulated signals. This is because when the target-derived phasor is kept off center, or not clutter filtered, noise does not alias with respect to the transponder-derived phasor. In other words, no two transponder phasor angles will appear as the same phase in the full signal. In the wideband case, the same cannot be true as all phases of the transponder derived phasor in Fig. 6.6 would clearly appear between approximately  $40^\circ - 50^\circ$  and there exists multiple instances where two transponder phasor angles result in the same overall signal phase.

An additional concern arises when the average phase of the transponder-derived component is not similar to that of the clutter as was shown in Fig. 6.6. A real data collection where the vibrating message was a single continuous 200 Hz tone is used to exemplify this case in Fig. 6.7. Though there is clearly some amount of clutter as indicated by the arc center's offset in orange, the data arc's average phase appears to be significantly different than that of the visually estimated constant clutter phasor. With regard to Fig. 6.7, the blue is the real IQ data for a signal assuming to have the form of Equation 6.19. The orange is a manual approximation of the transponder phasor arc and the orange is the manual approximation of the clutter phasor.

To achieve clutter filter, the properties of the resulting phasor were considered. Ideally, the resulting phasor has a near constant amplitude, where the only compo-

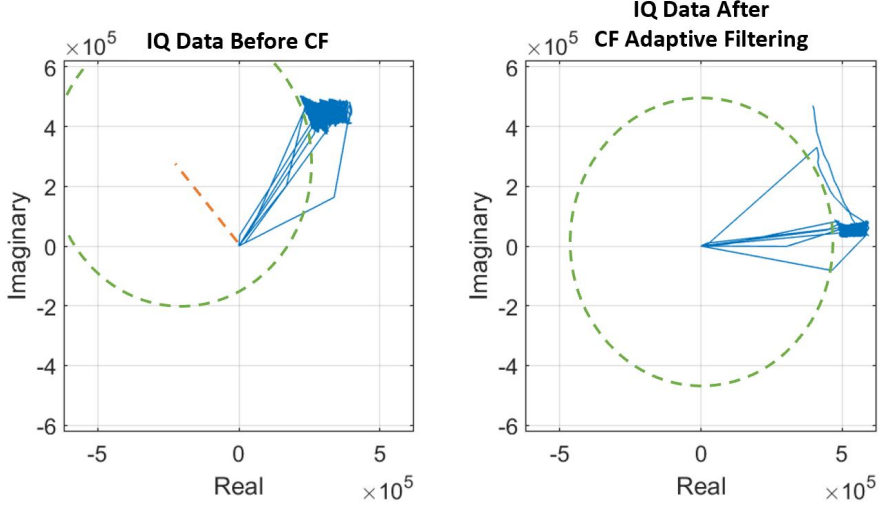


FIGURE 6.7: Vibrometry data of a 200 Hz vibrational displacement before and after adaptive clutter filtering.

ment causing amplitude variations is the AWGN. Using the constant modulus algorithm (CMA) then became a natural choice [75, 76]. CMA traditionally requires the radius of the modulus to be known, ie. the target's power must be known. Though this can potentially be estimated, we consider a different approach as the use of CMA in this application proved to be quite reliant on both the estimated target power but also the initial weight vector. Often, we found that the data would fall into local minima that did not result in an output that more closely resembles the the transponder phasor. This can be visualized by acknowledging that the raw IQ data before clutter filtering in Fig. 6.7 primarily appears to fall on a circle centered at the origin (not drawn) with approximately the same radius as the target phasor. Rather than adaptively adjusting to mitigate the bulk offset induced by the clutter phasor, the algorithm would get stuck at the original bulk offset when the weight vector was initialized to be the common all-pass weight vector.

From another lens, the goal of a constant modulus algorithm in this problem is to minimize the variance of the magnitude of the signal. This is because we inevitably want the data to reflect the target phasor centered at the origin. To minimize the

variance of the signal's magnitude, we describe the variance of the output signal as performance function,

$$J = \frac{1}{2} \mathbb{E}[(|y_{\text{out}}[k]| - \mathbb{E}[|y_{\text{out}}[k]|])^2]. \quad (6.20)$$

This differs slightly from the original CMA performance function as the amplitude terms are not squared and the desired radius term is now the expected value of the output amplitude. The reason we do not square the amplitudes is because not knowing the radius of the constant modulus signal ahead of time requires gradient descent on the inner expected value term. The gradient of that term leads to the multiplication of an averaging sum with another averaging sum. This is computationally more expensive than if only the amplitudes are used, so we resort to only using the amplitudes. It should be recognized that using either the amplitudes or amplitudes squared accomplishes the same thing here since squaring is a monotonically increasing for positive value inputs, which the absolute value operation satisfies. As previously mentioned, we purposefully also do not assume a good estimate of the desired radius term in our modified CMA performance function because we want the algorithm to adapt and learn that.

Within Equation 6.20,  $y_{\text{out}}[k]$  simply refers to the discretely sampled version of Equation 6.19 after it goes through our CMA-inspired adaptive filter. The input is likewise denoted as  $y_{\text{in}}[k]$ . The variable  $k$  is simply a discrete sample index in time such that  $t_k = k \text{PRI}$  since these signals are slow-time signals.

We use an averaging sum for expected value calculations such that the performance function becomes

$$J = \frac{1}{2N} \sum_{n=0}^{N-1} (|y_{\text{out}}[k-n]| - B[k-n])^2 \quad (6.21)$$

where

$$B[k] = \mathbb{E}[|y_{\text{out}}[k]|] = \frac{1}{N} \sum_{p=0}^{N-1} |y_{\text{out}}[k-p]|. \quad (6.22)$$

Furthermore,

$$y_{\text{out}}[k] = y_{\text{in}}[k] + A[k]((\cos \theta_k - \cos \phi[k]) + j(\sin \theta_k - \sin \phi[k])). \quad (6.23)$$

Equation 6.23 shows that the output of the adaptive filter is simply a translated version of the input. The space of translations in the complex plane are limited to positions on a circle whose center is the origin and radius is  $A[k]$ . This expression essentially requires a data point as seen in the first plot of Fig. 6.7, to only be transformed by the filter via rotating the data point around the origin with a scaling described by  $A[k]$ .

The term  $A[k]$  is the amplitude of the input data plus some adaptively optimized additive magnitude that allows the data arc's radius to vary from its original magnitude,

$$A[k] = |y_{\text{in}}[k]| + \gamma_k. \quad (6.24)$$

Equation 6.23 shows how the transformation of the input data in the complex plane depends on both the adaptively determined signal phase,  $\theta_k$  as well as the expected initial phase of the input data,  $\phi[k]$ . The initial phase of the input data is given by

$$\phi[k] = \mathbb{E}[\angle y_{\text{in}}[k]] = \frac{1}{N} \sum_{p=0}^{N-1} \tan^{-1} \left( \frac{\text{Im}(y_{\text{in}}[k-p])}{\text{Re}(y_{\text{in}}[k-p])} \right). \quad (6.25)$$

Performing gradient descent on the performance function with respect to the optimization variable  $\theta$ , we see that

$$\nabla_{\theta} J = \frac{1}{N} \sum_{n=0}^{N-1} (|y_{\text{out}}[k-n]| - B[k-n]) \left( \frac{y_{\text{out}}[k-n]}{|y_{\text{out}}[k-n]|} \nabla_{\theta} y_{\text{out}}[k-n] - \nabla_{\theta} B[k-n] \right), \quad (6.26)$$

where  $\nabla_{\theta}$  denotes the derivative with respect to  $\theta_k$ . Within that expression,

$$\nabla_{\theta} y_{\text{out}}[k-n] = -A[k-n](\sin \theta_k - j \cos \theta_k) \quad (6.27)$$

and

$$\nabla_{\theta} B[k - n] = \frac{1}{N} \sum_{p=0}^{N-1} \frac{y_{\text{out}}[k - n - p]}{|y_{\text{out}}[k - n - p]|} \nabla_{\theta} y_{\text{out}}[k - n - p]. \quad (6.28)$$

For every  $k$ , the next estimate of  $\theta$  is then derived using

$$\theta_{k+1} = \theta_k - \mu_{\theta} \nabla_{\theta} J, \quad (6.29)$$

where  $\mu_{\theta}$  is a positive step-size term for gradient descent on the performance function with respect to  $\theta_k$ .

Gradient descent is similarly used to update the additive magnitude variable  $\gamma$ ,

$$\nabla_{\gamma} J = \frac{1}{N} \sum_{n=0}^{N-1} (|y_{\text{out}}[k - n]| - B[k - n]) \left( \frac{y_{\text{out}}[k - n]}{|y_{\text{out}}[k - n]|} \nabla_{\gamma} y_{\text{out}}[k - n] - \nabla_{\gamma} B[k - n] \right). \quad (6.30)$$

Within that expression,

$$\nabla_{\gamma} y_{\text{out}}[k - n] = ((\cos \theta_k - \cos \phi[k - n]) + j(\sin \theta_k - \sin \phi[k - n])) \quad (6.31)$$

and

$$\nabla_{\gamma} B[k - n] = \frac{1}{N} \sum_{p=0}^{N-1} \frac{y_{\text{out}}[k - n - p]}{|y_{\text{out}}[k - n - p]|} \nabla_{\gamma} y_{\text{out}}[k - n - p]. \quad (6.32)$$

For every  $k$ , the next estimate of  $\gamma$  is then derived using

$$\gamma_{k+1} = \gamma_k - \mu_{\gamma} \nabla_{\gamma} J. \quad (6.33)$$

The term  $\mu_{\gamma}$  is once again a positive step size.

Upon using this adaptive algorithm to minimize the variance of output's magnitude the second plot in Fig. 6.7 is achieved. This method for clutter filtering works fairly well when signal power to clutter power ratio is greater than 1. Consider the real data given previously. Fig. 6.8 shows that through this adaptive algorithm, the phase signal much more closely resembles the expected 200 Hz tone.

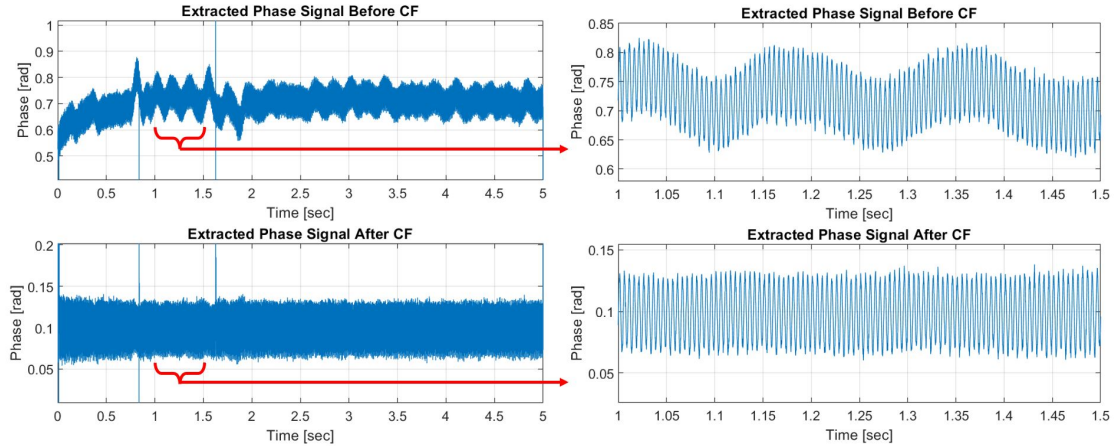


FIGURE 6.8: Phase signal estimations for vibrometry data of a 200 Hz vibrational displacement before and after clutter filtering.

The primary benefit of this clutter filtering method is that if it used prior to the synchronization and impulse response estimation processing steps, a better phase signal estimate should be provided leading to a more accurate start time and transponder impulse response estimation. Improvements in this space should allow for better performance in detection because of this and not necessarily because this clutter filtering method results in substantially better data vectors. This may come as a surprise, so consider the expected data vectors for various tonal symbols as was used in our real data collection.

All arbitrary tonal symbols are expected to contain some 0 Hz Doppler content, as has been shown via the Bessel function result of an expected VRBC tonal symbol in Chapters 4 and 5. The amount of power these tonal symbols has at 0 Hz Doppler does not depend on the tone's frequency but rather its amplitude. Accordingly, if all the tone's have similar amplitudes, they will have similar amounts of power at 0 Hz Doppler. If our new clutter filtering method manages to allow the 0 Hz content related to the transponder to be accurately passed as opposed to being filtered out, then it is true that more information regarding the symbols in a sequence are indeed

kept. However, if that 0 Hz content is of similar magnitude between all the symbols, then that additional information is not unique to a given symbol.

This is why using conventional clutter filtering methods provides decent results. Because all tonal symbols used in that collection had similar 0 Hz power content, the consequence of filtering out the 0 Hz content of each symbol was minimal. Naturally, if the sequence symbols had distinctly different levels of 0 Hz power content due to having displacement amplitudes that differed substantially, this would not be the case. Because it is hard to predict ahead of time whether this condition is held, as it depends on the transponder's impulse response, we recommend using this clutter filtering method regardless.

When implementing this clutter filtering method on the real data collecting in Chapter 4. It was found the improvements in synchronization and impulse response estimation led to a symbol detection improvement of only one more correct detection. This indicates that the signal characteristic most limiting to detection performance in this case is most likely the under-modeled ISI as was previously discussed. Despite the theoretical justification provided and initial success as seen by the 200 Hz tone example, more rigorous testing is still needed on this clutter filtering method to ensure its robustness in a multitude of possible scenarios.

### 6.3 Vibrational Noise Mitigation

In applications such as anything-to-vehicle (X2V) communications, it is expected that the system radar will be fixed onto a vibrating object or surface. In the X2V case, that object is a vehicle, and anyone who has been in a vehicle knows that vibrations, bumps, and sometimes sudden jolts are expected to occur. In X2V, VRBC transponders may also be located on vibrating surfaces like a vehicle. For that reason, methods for mitigating vibrational noise at both the radar and target have been developed.

### 6.3.1 Vehicle Vibrational Noise Characterization

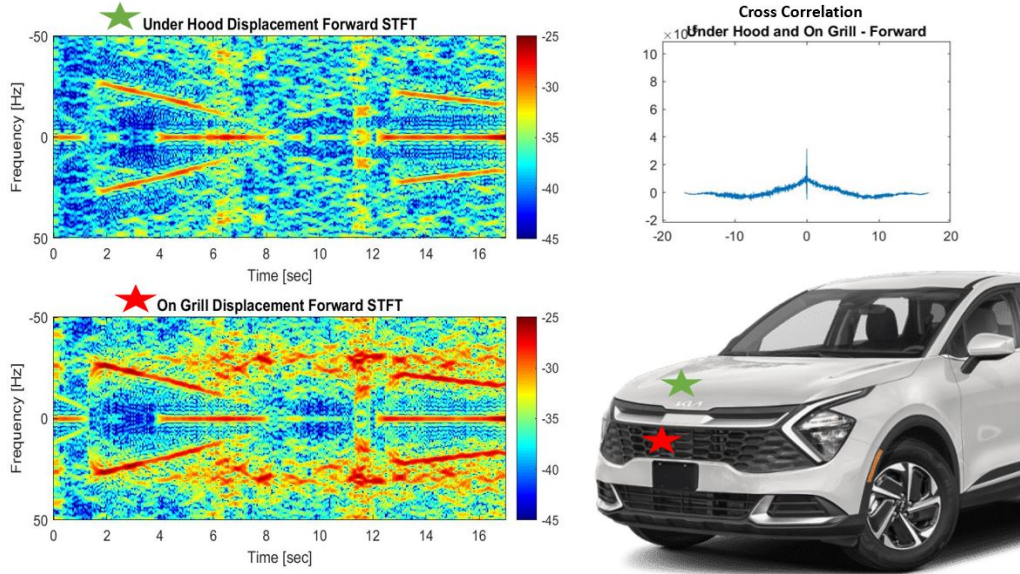


FIGURE 6.9: During this collection, the vehicle is accelerating from 40 – 60 mph on a relatively smooth highway.

To mitigate vehicle vibrational noise that acts on either the radar or a target, we first conducted a data collection to characterize the expected noise. Fig. 6.9 shows the short-time Fourier transform (STFT) of an accelerometer data collection on a 2023 hybrid Kia Sportage. The accelerometers used in this collection were the MTw Awinda accelerometers by Xsens. They have a sample rate of 100 Hz, and are three axes. In this collection, accelerometers were placed in five places, but for conciseness only two are shown in Fig. 6.9. Similarly, only the forward-direction vibrations are shown here, as that is the direction most likely to affect mmW radar vibrometry measurements for an automotive radar. Fig. 6.10 provides the raw displacement time-series and the associated spectra for all three axes of the same two accelerometers in addition to one placed near the visor on the inside ceiling next to the front window. From Figs. 6.9 and 6.10, there are three main takeaways related to mitigating vehicular vibrational noise in automotive radars.

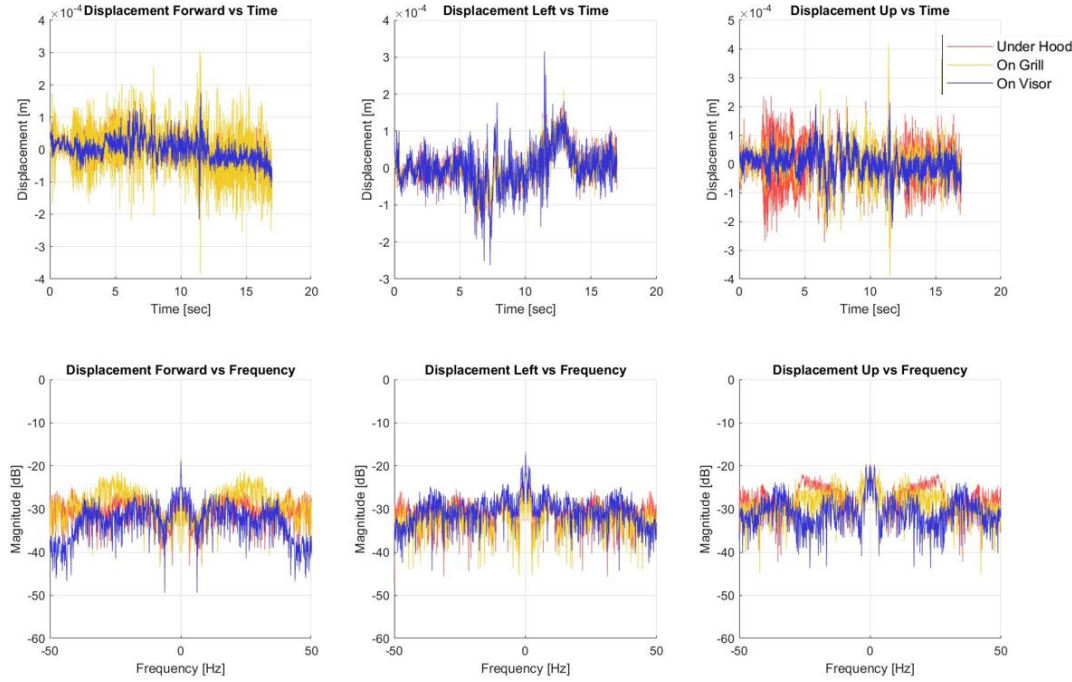


FIGURE 6.10: During this collection, the vehicle is accelerating from 40 – 60 mph on a relatively smooth highway.

First, most of the vehicle’s vibrational noise seems to be at about 40 Hz or less. Though we are unable to measure higher than 50 Hz frequency vibrations due to the accelerometers sampling frequency, the academic literature seems to support the idea that most road, wind, or operational noise exists at lower frequencies. For instance, [77]’s collections show bumper vibrations due to airflow and rough road surfaces remain below 40 Hz. Additionally, [78]’s measurements revealed that oscillations at frequencies below 100 Hz with amplitudes of 1 mm or less occur on an automotive radar sensor. Because most driving noise exists at lower frequencies, VRBC in X2V could all together avoid having symbols at lower than 100 Hz frequencies such that even if noise mitigation is imperfect, detection can remain robust. This is a fine solution, though not ideal.

Consider the bandwidth of vibrating frequencies available to a VRBC system.

They relate to the radar waveform's PRF. Specifically, the range of frequencies available is  $[0, \text{PRF}/2]$ . Since automotive PRFs tend to be between 1 – 10 kHz, avoiding frequencies less than 100 Hz proves fairly easy to do. A frequency in that lower range, however may be a natural frequency of the transponder, making it a desirable symbol tone. Upon some analysis, it may be found that the benefits of operating at that frequency outweigh the concerns. If no efforts are inevitably made to avoid operating at these frequencies where vehicle noise tends to exist, a robust noise mitigation method is needed that will not simultaneously suppress a VRBC transponder's message-bearing vibrations. In Subsection 6.3.2, a method towards this goal is presented.

The second point to take from Fig. 6.9 is that the noise between multiple points on the vehicle are correlated. This can be seen by the distinct spike at 0 in the cross correlation plot shown. This remained true for all 5 points observed in our data collection, which included under the hood, on the grill, behind the grill, on the floorboard inside the vehicle, and on the inside ceiling right next to the front window. Some points were more correlated than others, but all cross-correlation plots contained a spike at 0 indicating correlation nonetheless. This is particularly important in efforts of mitigating target vibrational noise because it shows that the vibrational noise of a transponder located at one position on a vehicle can be estimated and subtracted off using an estimate of the noise from another location on the vehicle.

The third key observation from Fig. 6.9 is less obvious. The Kia Sportage in this collection is a hybrid vehicle. It just so happens, that this vehicle uses its gas engine during acceleration. Between shifting gears, though, it switches to electric. Fig. 6.9 captures a time frame in which the vehicle switches from electric mode to gas mode for acceleration (at around 1.8 sec.). Then, the vehicle switches to electric mode to automatically shift gears (at around 8 sec.). Upon having shifted gears, the vehicle

returns to gas mode and continues to accelerate. By viewing the collection's STFT plots, strong tonal frequencies appear which seem to inversely relate to the speed of the car adjusted for a given gear level. As vehicles trend toward being electric, this observation indicates that less vibrational noise is expected to be present, which only further encourages mmW radar vibrometry-based capabilities like VRBC to be used in vehicles. For now though, vibrational noise mitigation remains all the more vital.

### 6.3.2 Mitigation of Radar Platform Vibrations

In [79], a method for estimating and then mitigating any automotive vibrations acting on a radar was presented. It is this method that VRBC in X2V would make use of to avoid having substantial additional errors in message detection. Such errors result from the fact that vibrational noise causes phase variations that create an undesired energy spread across adjacent Doppler bins. This inevitably means that the energy from a given object at its anticipated Doppler-bin is reduced. Effects like these not only cause errors in vibrometry measurements but can also lead to an increase in detection errors before even attempting to decode a VRBC message [77, 80].

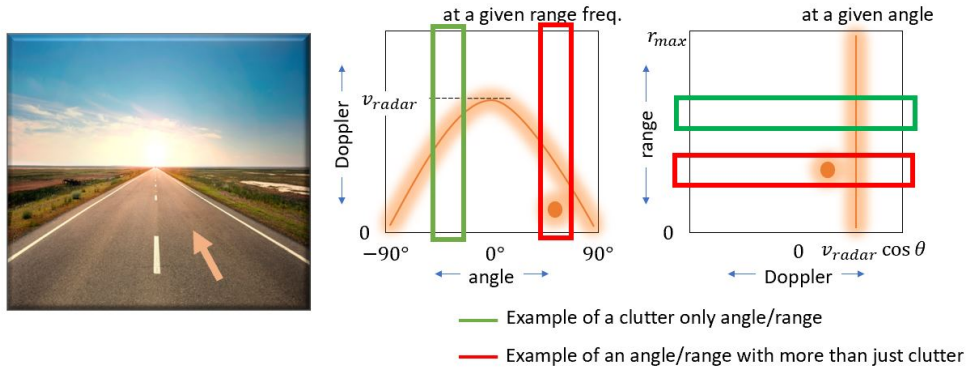


FIGURE 6.11: Depicted are a few non-stationary objects appearing outside of the clutter ridge.

The method for mitigating automotive noise according to [79] first looks to estimate the platform vibration using range-angle points of assumed clutter. It is

important that this clutter appears to have minimal movements aside from that caused by the platform moving at some constant velocity, ie. the clutter is stationary. These range-angle combinations can be found in range-angle-Doppler space by ensuring that only the clutter ridge is present. For a given angle, this will look like a line in range-Doppler space. For a given range, the clutter ridge will look like an arc in Doppler-angle space. Fig. 6.11 depicts the basic form of the clutter ridge in Doppler-angle space and range-Doppler space. An angle bin given a particular range that contains only clutter as well as one that does not are shown in the Doppler-angle plot. The same is then shown for range bins in range-Doppler space.

Once range and angle combinations where only clutter is present have been identified, the slow-time signal at each combination's given range,  $r_m$ , and angle,  $\theta_m$ , is used

$$y(t, r_m, \theta_m) = \sum_k \tilde{\alpha}_k e^{j \frac{4\pi}{\lambda_0} (r_m - d_n(t) - v_{\text{radar}} t)} + \tilde{n}(t). \quad (6.34)$$

Let  $m$  index a clutter range-angle combination. Here,  $d_n(t)$  is a radial vibrational noise displacement caused by the radar platform. Though there is a Doppler spread due to the radar platform's motion, as shown in Equation 4.7 and depicted in Fig. 6.11 by the width of the clutter ridge, we now approximate 6.34 assuming the spread is minimal

$$y(t, r_m, \theta_m) \approx \tilde{\alpha}_{\text{clt}} e^{j \frac{4\pi}{\lambda_0} (r_m - d_n(t) - v_{\text{radar}} t)} + \tilde{n}(t). \quad (6.35)$$

Now, we take the phase of this signal, assume that the AWGN variance is much smaller than the power of the clutter, and compensate for any known vehicle movement

$$s_{r_m, \theta_m}(t) = -\angle y(t, r_m, \theta_m) + \frac{4\pi}{\lambda_0} (r_m - v_{\text{radar}} t) \approx \frac{4\pi}{\lambda_0} d_n(t) + \Phi_m \quad (6.36)$$

where  $\Phi_m$  is the uniformly random phase offset caused by the complex amplitude  $\tilde{\alpha}_{\text{clt}}$ .  $\Phi_m$  can be estimated by eliminating any observed constant offset, or 0 Hz

component, of  $s_{r_m, \theta_m}(t)$  to get

$$s_{r_m, \theta_m}(t) \approx \frac{4\pi}{\lambda_0} d_n(t). \quad (6.37)$$

If this process is completed for  $M$  different clutter points, a global vibration estimate can be found as the average of the multiple estimates after accounting for angle

$$\hat{d}_n(t) = \frac{\lambda_0}{4\pi} \frac{1}{M} \sum_{m=1}^M \frac{s_{r_m, \theta_m}(t)}{\cos \theta_m} \quad (6.38)$$

To use the estimated platform vibration signal to mitigate the noise and avoid the consequences of its presence, the vibrational influence at a given angle,  $\theta_p$ , can be found using

$$\hat{d}_{n, \theta_p}(t) = \hat{d}_n(t) \cos \theta_p \quad (6.39)$$

and the full range vs angle vs slow-time map can be corrected using

$$\hat{y}(t, r_m, \theta_p) = y(t, r_m, \theta_p) e^{j\hat{d}_{n, \theta_p}(t)} \quad (6.40)$$

for all  $m$  and  $p$  that span the desired ranges and look angles under consideration.

If the radar being used has angular resolution in both azimuth and elevation, all equations presented remain accurate but require all instances of  $\cos \theta$  to become  $\cos \theta_{\text{azimuth}} \cos \theta_{\text{elevation}}$ . Upon acquiring the noise canceled signal for all range-angle combinations of interest, mmW radar signal processing techniques including those used in VRBC can be used as normal.

### 6.3.3 Mitigation of Target Vibrational Noise

Previously, a method was considered to minimize the negative effects of radar platform noise. In the application of X2V, however, statistically similar vibrational noise is anticipated to be present at the target's platform. Take for example the case where the vibrating transponder is a license plate attached to a vehicle for instance. In such

circumstances, assume that radar platform noise has been mitigated and only the vibrational noise of the transponder's platform is causing errors in detection and message decoding.

The signal of interest is now the slow-time signal at range and angle combinations indexed by  $m$  that the target and target platform occupy,  $m \in \mathcal{M}_{\text{tar}}$ . The set  $\mathcal{M}_{\text{tar}}$  describes the points which are fully described by their individual ranges,  $r_m$ , and angles,  $\theta_m$ , that encompass the target platform, like a vehicle that a VRBC transponder is located on. We let  $\mathcal{M}_{\text{VRBC}}$  describe the subset of range and angle combinations within  $\mathcal{M}_{\text{tar}}$  where the VRBC transponder is located. We assume here that  $|\mathcal{M}_{\text{tar}}| > |\mathcal{M}_{\text{VRBC}}|$ . In other words, the target platform occupies multiple location bins from the perspective of the radar and that the transponder occupies a fraction of those, ie.  $\mathcal{M}_{\text{VRBC}} \subset \mathcal{M}_{\text{tar}}$ .

Once again, assume that the Doppler spread of the clutter is minimal,

$$y(t, r_m, \theta_m) = \begin{cases} \tilde{\alpha}_{r_m, \theta_m} e^{j \frac{4\pi}{\lambda_0} (d_n(t) + d(t) - v_{\text{radar}}t + v_{\text{tar}}t)} + \tilde{n}(t) & m \in \mathcal{M}_{\text{tar}} \setminus \mathcal{M}_{\text{VRBC}} \\ \tilde{\alpha}_{r_m, \theta_m} e^{j \frac{4\pi}{\lambda_0} (d_n(t) - v_{\text{radar}}t + v_{\text{tar}}t)} + \tilde{n}(t) & m \in \mathcal{M}_{\text{VRBC}} \end{cases} \quad (6.41)$$

with  $\mathcal{M}_{\text{tar}} \setminus \mathcal{M}_{\text{VRBC}}$  indicating the set difference between the range-angle combinations encompassing the full target platform and that which only describe where the VRBC transponder is. Here,  $d_n(t)$  is now the transponder's platform vibrational noise displacement, while  $d(t)$  is the VRBC surface vibrational displacement. Note that for different range-angle points indexed by  $m$ , the complex amplitude  $\tilde{\alpha}_{r_m, \theta_m}$  differs and contributes a uniformly random phase offset. This was seen in modeling the radar platform vibrations as well.

As was done before, take the phase of this signal, assume that the noise variance is much smaller than the power of the clutter, and compensate for any known radar platform movement

$$s_{r_m, \theta_m}(t) \approx \begin{cases} \frac{4\pi}{\lambda_0} (d_n(t) + d(t) + v_{\text{tar}}t) + \Phi_m & m \in \mathcal{M}_{\text{tar}} \setminus \mathcal{M}_{\text{VRBC}} \\ \frac{4\pi}{\lambda_0} (d_n(t) + v_{\text{tar}}t) + \Phi_m & m \in \mathcal{M}_{\text{VRBC}} \end{cases} \quad (6.42)$$

where  $\Phi_m$  is again the uniformly random phase offset caused by the complex amplitude  $\tilde{\alpha}_{\text{clt}}$ .  $\Phi_m$  terms can be estimated and subtracted out by finding the constant offset, or 0 Hz component, of  $s_{r_m, \theta_m}(t)$

$$s_{r_m, \theta_m}(t) \approx \begin{cases} \frac{4\pi}{\lambda_0}(d_n(t) + d(t) + v_{\text{tar}}t) & m \in \mathcal{M}_{\text{tar}} \setminus \mathcal{M}_{\text{VRBC}} \\ \frac{4\pi}{\lambda_0}(d_n(t) + v_{\text{tar}}t) & m \in \mathcal{M}_{\text{VRBC}} \end{cases}. \quad (6.43)$$

Following Equations 6.38, the transponder's vibrational platform noise displacement with the transponder's platform bulk movement can be estimated using the set  $\mathcal{M}_{\text{tar}} \setminus \mathcal{M}_{\text{VRBC}}$ . Mathematically,

$$\hat{d}_n(t) + \hat{v}_{\text{tar}}t = \frac{\lambda_0}{4\pi} \frac{1}{M} \sum_m^M \frac{s_{r_m, \theta_m}(t)}{\cos \theta_m} \quad (6.44)$$

for  $m \in \mathcal{M}_{\text{tar}} \setminus \mathcal{M}_{\text{VRBC}}$ .

In opposition to mitigating radar platform vibrational noise, we can no longer cancel transponder platform vibrational noise by simply canceling its effect at all ranges and angles. This is because not all range and angle bins contain the transponder platform. This does not mean that the slow-time signals for the transponder range and angle bins in Equation 6.41 cannot easily have the vibrational noise and target bulk movement mitigated by multiplying by  $e^{-j2\pi f_0 \hat{\tau}_{\text{tar}}(t)}$ . They still can. Though this is theoretically easy, it must be recognized that continuously and accurately modeling all of the points  $m \in \mathcal{M}_{\text{tar}}$  can be difficult to do exactly. Let it be recognized that the process described for estimating the global transponder platform vibration and bulk movement does not require the use of all points  $m \in \mathcal{M}_{\text{tar}}$  but rather only  $M$  of those points, see Equation 6.44. Therefore, inaccuracies in accounting for all points  $m \in \mathcal{M}_{\text{tar}}$  do not affect the vibrational noise estimation. Actual noise cancellation, however, does require knowing all points within  $\mathcal{M}_{\text{tar}}$ .

Certainly, operating in the slow-time domain by choosing a point in  $\mathcal{M}_{\text{VRBC}}$ , canceling the effects of the estimated transponder platform noise and bulk movement,

and then resorting to maximum likelihood detection using data vectors derived from the slow-time signal can be completed. In [81, 82], we performed detection in this exact way. As shown in [83] and Chapter 4 of this dissertation, the full de-chirped signal can prove advantageous in VRBC detection though. At the most simple level, using the full fast-time sampled signal allows for more energy of the signal to be captured and used in detection. For that reason, we recommend accounting for the phase contribution of vibrational noise and transponder bulk movement rather than trying to truly cancel it. Accounting for the vibrational noise simply means that the estimate of the noise must be used in detection through more accurately modeling symbol data vectors. Just as we looked to model error-causing intersymbol interference in this chapter rather than canceling it, a similar approach is taken here.

To begin, recall that the synchronization and impulse response estimation steps in VRBC signal processing take place in the slow-time domain. The estimate of the transponder's platform vibrational noise and bulk target movement should then be removed from the slow-time signal using Equations 6.39 and 6.40. This allows both synchronization and impulse response estimation to be completed prior to message decoding without being significantly affected by the vibrational noise.

When returning to the fast-time signal for message decoding, we see that the signal assuming good clutter filtering is

$$y(t) = \tilde{\alpha}_{\text{tar}} e^{j2\pi f_0 \tau_{\text{tar}}} \sum_{g=0}^{G-1} z_{\text{tar}}(t - gT_{\text{PRI}}) + \tilde{\eta}(t) \quad (6.45)$$

where

$$z_{\text{tar}}(t) = \begin{cases} e^{j\pi\beta(2\tau_{\text{tar}}(t) - \tau_{\text{tar}}^2(t))} & \tau_{\text{tar}}(t) \leq t < T \\ 0 & \text{otherwise} \end{cases} \quad (6.46)$$

and  $\tau_{\text{tar}}(t) = \frac{2}{c}(r_{\text{tar}} + d(t) + d_n(t) - v_{\text{radar}}t + v_{\text{tar}}t)$ .

At this point, target detection has provided an estimate of  $r_{\text{tar}} - v_{\text{radar}}t$  in addition to  $\theta_{\text{tar}}(t)$ . Impulse response estimation and prior knowledge of excitation signals also

allow for  $d(t)$  to be well estimated. Through the methods shown in this section, we also have an estimate of  $d_n(t) + v_{\text{tar}}t$ . This means all of the components in  $\tau_{\text{tar}}(t)$  are estimated. This knowledge allows the noise-free data vectors  $\mathbf{a}^{(m,s)}$  to be accurately generated and used in detection.

In summary, though the vibrational platform noise of the transponder may not have been entirely mitigated for detection, its ability to cancel the noise in its corresponding slow-time signal which is used for synchronization and impulse response estimation allows for the full de-chirped signal to be more accurately modeled for detection. More accurate modeling then minimizes errors caused by the transponder's platform noise.

In a system where both radar platform and transponder platform vibrational noise is present, the previously presented processing chain would be modified to what is presented in Fig. 6.12.

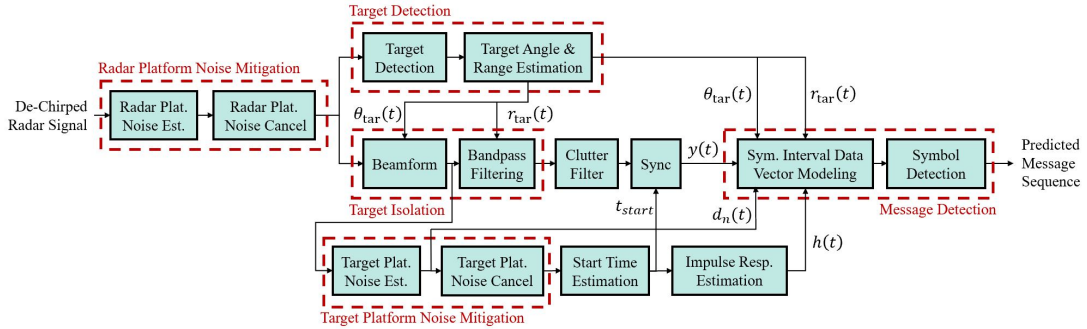


FIGURE 6.12: The full processing chain used to decode a VRBC message when both radar and transponder platforms have vibrational noise.

## Conclusion

In this dissertation, applied millimeter wave radar vibrometry was investigated. Models for how various objects' vibrational displacements impact a common FMCW mmW radar's return were provided, and signal processing methods were developed such that these vibrations could be used in applications. Applications such as non-acoustic speaker identification and anything-to-vehicle communications were highlighted as spaces where mmW radar vibrometry has significant potential.

Results demonstrated that larynx mmW radar vibrometry was comparable to vibrometry completed with an expensive LDV. Additionally, we showed that mmW radar vibrometry in non-acoustic human speech could lead to a solution in the space of content-blind speaker identification as its return contains much of the low-frequency content that its corresponding acoustic data has. We found that this frequency selectivity of mmW radar vibrometry could serve as a feature to allow data used in speaker identification systems to provide contextual privacy with respect to what was said since it allowed preliminary speaker identification performance to remain above 50% while speech recognition performance dropped to 11%.

We also presented a novel wireless communication system known as vibrational

radar backscatter communication (VRBC). VRBC serves as a backscatter communication solution at mmW with atypical advantages when compared to competing solutions. These advantages include that the message source requires no RF transmission, communication channels are scalable and avoid mutual interference, and mmW sensing is able to continue undisturbed using the system’s radar. In introducing this system, VRBC transponder detection, isolation, and maximum likelihood detection methods were detailed to clearly show how a vibrating surface’s message can be received by a mmW radar both in theory and in practice. Methods for clutter filtering, synchronizing, and estimating system parameters like a transponder’s impulse response were provided, as these steps prove vital in demonstrating a VRBC system’s practicality.

Work providing a theoretical upper bound on a VRBC system’s data rate was detailed in addition to a discussion on multiple system trade-offs and design choices. This bound was compared to multiple simulation scenarios to provide insight as to when this bound is tight. This bound was fundamentally shown to be restricted in first and foremost by the system’s radar parameter choices and the transponder’s design.

A chapter was also provided to discuss observed challenges for VRBC in practice. These challenges included modeling resonant transponding surfaces, minimizing the consequences of conventional clutter filters, and mitigating both radar and transponder platform vibrational noise. Initial solutions for all of these were provided to demonstrate how VRBC could be practically implemented in the specific application of anything-to-vehicle (X2v) communications.

## 7.1 Future Work

Towards advances in mmW radar vibrometry for human speech analysis, work was concluded without having trained and tested speaker identification and speech recog-

nition on true larynx mmW radar vibrometry data sets. Though loudspeaker vibrometry data similar to larynx vibrometry data was used, there is room for speculation as to how true larynx vibrometry data would perform. In fully arguing that larynx mmW radar vibrometry could provide a content-blind speaker identification solution, both a full mmW radar vibrometry data set of human larynx vibrations during speech generation needs acquired and a re-trainable speech recognition system is needed such that it cannot be argued that the speech recognition performance is merely a lower bound.

For vibrational radar backscatter communications, the true feasibility of VRBC in applications like X2V needs to be proven through system implementation using a desirable transponder and optimized messaging scheme. Within this dissertation, favorable choices were made with respect to both of these areas, but an iterative system design and optimization process would provide the necessary proof to strengthen the argument for VRBC in application. This process should include optimization of parameters pertaining to the messaging scheme and symbols as well as transponder design. Transponder design should explore different geometries, actuators, and mechanical designs. Actuator arrays should also be looked into, as they may provide the opportunity for a more controllable yet higher RCS responding surface. Additionally, exploring retro-directive transponder solutions should be considered so that VRBC can be shown to be robust to dynamically changing scenario geometries. It is also recommended that the methods provided for suppressing expected system noise like platform vibrations be further vetted by fully implementing and testing them in different settings. These areas of research are vital in proving the practicality of a VRBC system, as the primarily theoretical framework provided in this dissertation may encounter more practical issues than even those already outlined.

# Bibliography

- [1] V. C. Chen, F. Li, S.-S. Ho, and H. Wechsler, “Micro-doppler effect in radar: Phenomenon, model, and simulation study,” *IEEE Transactions on Aerospace and Electronic Systems*, vol. 42, no. 1, pp. 2–21, 2006.
- [2] B. Wang, Z. Zheng, and Y.-X. Guo, “Millimeter-wave frequency modulated continuous wave radar-based soft fall detection using pattern contour-confined doppler-time maps,” *IEEE Sensors Journal*, vol. 22, no. 10, pp. 9824–9831, 2022.
- [3] M. Martinez, “Uas detection, classification, and tracking in urban terrain,” in *2019 IEEE Radar Conference (RadarConf)*, pp. 1–6, 2019.
- [4] L. O. Fhager, S. Heunisch, H. Dahlberg, A. Evertsson, and L.-E. Wernersson, “Pulsed millimeter wave radar for hand gesture sensing and classification,” *IEEE Sensors Letters*, vol. 3, no. 12, pp. 1–4, 2019.
- [5] L. Piotrowsky and N. Pohl, “Spatially resolved fast-time vibrometry using ultrawideband fmcw radar systems,” *IEEE Transactions on Microwave Theory and Techniques*, vol. 69, no. 1, pp. 1082–1095, 2021.
- [6] G. Ramachandran and M. Singh, “Three-dimensional reconstruction of cardiac displacement patterns on the chest wall during the p, qrs and t-segments of the ecg by laser speckle interferometry,” *Med Biol Eng Comput.*, vol. 27, p. 525–530, 1989.
- [7] Y. Zhang, S. Mayer, J. T. Gonzalez, and C. Harrison, “Vibrosight++: City-scale sensing using existing retroreflective signs and markers,” in *CHI Conference on Human Factors in Computing Systems (CHI '21)*, 2021.
- [8] S. Rothberg, “An international review of laser doppler vibrometry: Making light work of vibration measurement,” *Optics and Lasers in Engineering*, vol. 99, 2017.
- [9] Q. Davis and W. Kulczyk, “Vibrations of turbine blades measured by means of a laser,” *Nature*, vol. 222, pp. 475–476, 1969.

- [10] G. Bank and G. T. Hathaway, “A revolutionary 3-d interferometric vibrational mode display,” *Journal of the Audio Engineering Society*, 1980.
- [11] M. Batel, “Deploying successfully laser doppler vibrometry techniques within the automotive nvh process,” *Journal of the Acoustical Society of America*, vol. 123, no. 5, p. 3868, 2008.
- [12] T. M. Huber, “Measurement of mode shapes of musical instruments using a scanning laser doppler vibrometer,” *The Journal of the Acoustical Society of America*, vol. 129, p. 2615, 2011.
- [13] M. Klun, D. Zupan, J. Lopatič, and A. Kryžanowski, “On the application of laser vibrometry to perform structural health monitoring in non-stationary conditions of a hydropower dam,” *Sensors*, vol. 19, no. 17, p. 3811, 2019.
- [14] B. Aicher, H. Markl, W. M. Masters, and H. L. Kirschenlohr, “Vibration transmission through the walking legs of the fiddler crab, uca pugilator (brachyura, ocypodidae) as measured by laser doppler vibrometry,” *Journal of Comparative Physiology*, vol. 150, no. 4, pp. 483–491, 1983.
- [15] M. J. M. Martens, “Laser-doppler vibrometer measurements of leaves,” in *Physical Methods in Plant Sciences. Modern Methods of Plant Analysis* (H. F. Linskens and J. F. Jackson, eds.), vol. 11, Springer, 1990.
- [16] G. Ciattaglia, S. Spinsante, and E. Gambi, “Slow-time mmwave radar vibrometry for drowsiness detection,” in *2021 IEEE International Workshop on Metrolology for Automotive (MetroAutomotive)*, pp. 141–146, 2021.
- [17] S. Agarwal, D. Singh, and N. P. Pathak, “Active millimeter wave radar system for non-destructive, non-invasive underline fault detection and multilayer material analysis,” in *2014 IEEE International Microwave and RF Conference (IMaRC)*, pp. 369–372, 2014.
- [18] J. Moll, K. Bechtel, B. Hils, and V. Krozer, “Vibration sensing for structural health monitoring using a millimeter-wave doppler radar sensor,” in *EWSHM - 7th European Workshop on Structural Health Monitoring*, 2014.
- [19] O. Postolache, P. S. Girão, R. N. Madeira, and G. Postolache, “Microwave fmcw doppler radar implementation for in-house pervasive health care system,” in *2010 IEEE International Workshop on Medical Measurements and Applications*, pp. 47–52, 2010.
- [20] European Parliament and Council of the European Union, “Article 5.1 – 2,” 2016.

- [21] J. Harding, G. R. Powell, R. Yoon, J. Fikentscher, C. Doyle, D. Sade, M. Lukuc, J. Simons, and J. Wang, “Vehicle-to-vehicle communications: Readiness of v2v technology for application.,” *National Highway Traffic Safety Administration*, 2014.
- [22] S. E. Shladover, “Connected and automated vehicle systems: Introduction and overview,” no. 3, pp. 190–200, 2018.
- [23] Texas Instruments, *IWR1443 Single-Chip 76- to 81-GHz mmWave Sensor*, October 2018.
- [24] E. B. Kamel, A. Peden, and P. Pajusco, “Rcs modeling and measurements for automotive radar application in the w band,” in *11th European Conference on Antennas and Propogation*, pp. 2445–2449, IEEE, 2017.
- [25] O. Schumann, J. Lombacher, M. Hahn, C. Wöhler, and J. Dickman, “Scene understanding with automotive radar,” *IEEE Transactions on Intelligent Vehicles*, vol. 5, no. 2, pp. 188–203, 2020.
- [26] X. Cai, M. Giallorenzo, and K. Sarabandi, “Machine learning-based target classification for mmw radar in autonomous driving,” *IEEE Transactions on Intelligent Vehicles*, vol. 6, no. 4, pp. 678–689, 2021.
- [27] P. K. M. Nkwari, S. Sinha, and H. C. Ferreira, “Through-the-wall radar imaging: A review,” *IETE Technical Review*, vol. 35, no. 6, pp. 631–639, 2018.
- [28] J. A. Nanzer, *Microwave and Millimeter-Wave Remote Sensing for Security Applications*. 2012.
- [29] C. Kumar, H. U. R. Mohammed, and G. Peake, *Application Report mmWave Radar Radome Design Guide*. Texas Instruments, 2021.
- [30] W. Menzel, T. Walter, M. Köhler, J. Hasch, H. L. Blöcher, and L.-P. Schmidt, “Feasibility of automotive radar at frequencies beyond 100 ghz,” *International Journal of Microwave and Wireless Technologies*, vol. 5, no. 1, pp. 49–54, 2013.
- [31] G. Buccheri, E. De Lauro, S. De Martino, and M. Falanga, “Power spectra of constrained codes with level-based signaling: Overcoming finite-length challenges,” *Biomedical Physics and Engineering Express*, vol. 2, no. 5, p. 055009, 2016.
- [32] Texas Instruments, *TI mmWave Labs - Vital Signs Measurement*, 2017.
- [33] A. Ahmad, J. C. Roh, D. Wang, and A. Dubey, “Vital signs monitoring of multiple people using a fmcw millimeter-wave sensor,” in *IEEE Radar Conference (RadarConf18)*, pp. 1450–1455, IEEE, 2018.

- [34] S. M. M. Islam, N. Motoyama, S. Pacheco, and V. M. Lubecke, “Non-contact vital signs monitoring for multiple subjects using a millimeter wave fmcw automotive radar,” in *IEEE/MTT-S International Microwave Symposium (IMS)*, pp. 783–786, IEEE, 2020.
- [35] G. Wang, J.-M. Muñoz-Ferreras, C. Gu, C. Li, and R. Gómez-García, “Application of linear-frequency-modulated continuous-wave (lfmcw) radars for tracking of vital signs,” *IEEE Transactions on Microwave Theory and Techniques*, vol. 62, no. 6, pp. 1387–1399, 2014.
- [36] K. Delac and M. Grgic, “A survey of biometric recognition methods,” in *46th International Symposium on Electronics in Marine*, pp. 184–193, IEEE, 2004.
- [37] R. Tognoni and D. Pullella, “An overview of speaker identification: Accuracy an robustness issues,” *IEEE Circuits and Systems Magazine*, vol. 11, no. 2, pp. 23–61, 2011.
- [38] C. Glackin, G. Chollet, N. Dugan, N. Cannings, J. Wall, S. Tahir, I. G. Ray, and M. Rajarajan, “Privacy preserving encrypted phonetic search of speech data,” in *2017 IEEE International Conference on Acoustics, Speech and Signal Processing (ICASSP)*, pp. 6414–6418, IEEE, 2017.
- [39] S. Ahmed, A. R. Chowdhury, K. Fawaz, and P. Ramanathan, “Preech: A system for privacy-preserving speech transcription,” in *29th USENIX Conference on Security Symposium*, pp. 2703–2720, 2020.
- [40] T. D. Rossing, *The Handbook of Acoustics 2nd Edition*. Springer, 2014.
- [41] M. Nolan, B. Madden, and E. Burke, “Accelerator based measurement for the mapping of neck surface vibration during vocalized speech,” in *2009 Annual International Conference of the IEEE Engineering in Medicine and Biology Society*, pp. 4453–4456, IEEE, 2009.
- [42] J. S. Garofolo, L. F. Lamel, W. M. Fisher, J. G. Fiscus, D. S. Pallett, N. L. Dahlgren, and V. Zue, *TIMIT Acoustic-Phonetic Continuous Speech Corpus*. Philadelphia: Linguistic Data Consortium, 1993.
- [43] Y. Lukic, C. Vogt, O. Dürr, and T. Stadelmann, “Speaker identification and clustering using convolutional neural networks,” in *2016 IEEE 26th International Workshop on Machine Learning for Signal Processing (MLSP)*, pp. 1–6, IEEE, 2016.
- [44] H. Muckenhirn, M. M. Doss, and S. Marcell, “Towards directly modeling raw speech signal for speaker verification using cnns,” in *2018 IEEE International Conference on Acoustics, Speech and Signal Processing (ICASSP)*, p. 4884–4888, IEEE, 2018.

- [45] C. Li, X. Ma, B. Jiang, X. Li, X. Zhang, X. Liu, Y. Cao, A. Kannan, and Z. Zhu, “Deep speaker: An end-to-end neural speaker embedding system,” IEEE, 2017.
- [46] A. Argyriou, T. Evgeniou, and M. Pontil, “Multitask feature learning,” in *Advances in Neural Information Processing Systems*, p. 41–48, MIT Press, 2007.
- [47] Google, *Speech-to-Text*.
- [48] F. Guidi, N. Decarli, F. Dardari, Davide Mani, and R. D’Errico, “Passive millimeter-wave rfid using backscattered signals,” in *IEEE Globecom Workshops (GC Wkshps)*, pp. 1–6, IEEE, 2016.
- [49] F. Boccardi, R. W. Heath, A. Lozano, T. L. Marzetta, and P. Popovski, “Five disruptive technology directions for 5g,” *IEEE Communications Magazine*, vol. 52, no. 2, pp. 74–80, 2014.
- [50] M. Alhassoun, *Theory and Design of Next-Generation Retrodirective Tags and Their Channels*. PhD thesis, Georgia Institute of Technology, 2019.
- [51] E. Soltanaghaei, A. Prabhakara, A. Balanuta, A. Anderson, M. Anderson, J. M. Rabaey, S. Kumar, and A. Rowe, “Millimetro: mmwave retro-reflective tags for accurate, long range localization,” in *27th Annual International Conference on Mobile Computing and Networking (MobiCom ’21)*, pp. 69–82, ACM, 2021.
- [52] I. Cnaan-On, S. J. Thomas, J. L. Krolik, and M. S. Reynolds, “Multichannel backscatter communication and ranging for distributed sensing with an fmcw radar,” *IEEE Transactions on Microwave Theory and Techniques*, vol. 63, no. 7, pp. 2375–2383, 2015.
- [53] S. Bakhtiari, N. Gopalsami, T. Elmer, and A. C. Raptis, “Millimeter wave sensor for far-field standoff vibrometry,” *AIP Conference Proceedings*, vol. 1096, no. 1, pp. 1641–1648, 2009.
- [54] C. T. Rodenbeck, J. B. Beun, R. G. Raj, and R. D. Lipps, “Vibrometry and sound reproduction of acoustic sources on moving platforms using millimeter wave pulse-doppler radar,” *IEEE Access*, vol. 8, pp. 27676–27686, 2020.
- [55] F. Tonolini and F. Adib, “Multitask feature learning,” in *ACM SIGCOMM*, ACM, 2018.
- [56] N. T. P. Van, L. Tang, V. Demir, S. F. Hasan, N. D. Minh, and S. Mukhopadhyay, “Review-microwave radar sensing systems for search and rescue purposes,” *Sensors*, vol. 19, no. 13, p. 2879, 2019.
- [57] T. Yucek and H. Arslan, “A survey of spectrum sensing algorithms for cognitive radio applications,” *IEEE Communications Surveys and Tutorials*, vol. 11, no. 1, pp. 116–130, 2009.

- [58] N. C. Luong, X. Lu, D. T. Hoang, D. Niyato, and D. I. Kim, “Radio resource management in joint radar and communication: A comprehensive survey,” *IEEE Communications Surveys and Tutorials*, vol. 23, no. 2, pp. 780–814, 2021.
- [59] M. Labib, V. Marojevic, A. F. Martone, J. H. Reed, and A. I. Zaghloui, “Co-existence between communications and radar systems: A survey,” *URSI Radio Science Bulletin*, vol. 2017, no. 362, pp. 74–82, 2017.
- [60] A. R. Chiriyath, B. Paul, G. M. Jacyna, and D. W. Bliss, “Inner bounds on performance of radar and communications co-existence,” *IEEE Transactions on Signal Processing*, vol. 64, no. 2, pp. 464–474, 2016.
- [61] J. Jakabosky, B. Ravenscroft, S. D. Blunt, and A. Martone, “Gapped spectrum shaping for tandem-hopped radar/communications and cognitive sensing,” in *2016 IEEE Radar Conference (RadarConf)*, pp. 1–6, IEEE, 2016.
- [62] N. Cao, Y. Chen, X. Gu, and W. Feng, “Joint radar-communication waveform designs using signals from multiplexed users,” *IEEE Transactions on Communications*, vol. 68, no. 8, pp. 5216–5227, 2020.
- [63] M. Roberton and E. Brown, “Integrated radar and communications based on chirped spread-spectrum techniques,” in *IEEE MTT-S International Microwave Symposium Digest, 2003*, vol. 1, pp. 611–614, IEEE, 2003.
- [64] C. Sahin, J. Jakabosky, P. M. McCormick, J. G. Metcalf, and S. D. Blunt, “A novel approach for embedding communication symbols into physical radar waveforms,” in *2017 IEEE Radar Conference (RadarConf)*, pp. 1498–1503, IEEE, 2017.
- [65] R. Molina-Masegosa, J. Gozalvez, and M. Sepulcre, “Comparison of ieee 802.11p and lte-v2x: An evaluation with periodic and aperiodic messages of constant and variable size,” *IEEE Access*, vol. 8, pp. 121526–121548, 2020.
- [66] I. Senjanović, M. Tomić, N. Vladimir, and N. Hadžić, “An approximate analytical procedure for natural vibration analysis of free rectangular plates,” *Thin-Walled Structures*, vol. 95, pp. 101–114, 2015.
- [67] M. A. Richards, *Fundamentals of Radar Signal Processing*. McGraw-Hill Companies, Inc., 2005.
- [68] Z. Xu, C. J. Baker, and S. Pooni, “Range and doppler cell migration in wideband automotive radar,” *IEEE Transactions on Vehicular Technology*, vol. 68, no. 6, pp. 5527–5536, 2019.
- [69] J. Yu and J. Krolik, “Mimo multipath clutter mitigation for gmti automotive radar in urban environments,” in *IET International Conference on Radar Systems (Radar 2012)*, pp. 1–5, IEEE, 2012.

- [70] L. Ljung, *System Identification: Theory for the User, Second Edition*. Prentice-Hall PTR, 1999.
- [71] X.-g. Xia, “System identification using chirp signals and time-variant filters in the joint time-frequency domain,” *IEEE Transactions on Signal Processing*, vol. 45, no. 8, pp. 2072–2084, 1997.
- [72] A. Kolchinsky and B. D. Tracey, “Estimating mixture entropy with pairwise distances,” *MDPI Entropy Journal*, vol. 19, no. 361, 2017.
- [73] M. F. Huber, T. Bailey, H. Durrant-Whyte, and U. D. Hanebeck, “On entropy approximation for gaussian mixture random vectors,” in *2008 IEEE International Conference on Multisensor Fusion and Integration for Intelligent Systems*, pp. 181–188, 2008.
- [74] U. S. C. of Appeals for the District of Columbia Circuit, “Document 1959069,” no. 21-1130, 2022.
- [75] J. Treichler and B. Agee, “A new approach to multipath correction of constant modulus signals,” *IEEE Transactions on Acoustics, Speech, and Signal Processing*, vol. 31, no. 2, pp. 459–472, 1983.
- [76] Y. Ogawa, N. Honma, K. Murata, M. Iwai, and K. Kobayashi, “Vital sign tracking using modified constant modulus algorithm adaptive array,” *IEEE Sensors Letters*, vol. 7, no. 2, pp. 1–4, 2023.
- [77] M. Harter and J. Hildebrandt, “Vibrations in automotive radar systems,” in *2016 IEEE MTT-S International Conference on Microwaves for Intelligent Mobility (ICMIM)*, pp. 1–4, 2016.
- [78] F. Hau, F. Baumgärtner, and M. Vossiek, “The degradation of automotive radar sensor signals caused by vehicle vibrations and other nonlinear movements,” vol. 20, p. 6195, 2020.
- [79] O. Longman, I. Bilik, S. Villeval, and S. Shayovitz, “Mitigation of vehicle vibration effect on automotive radar,” in *2019 IEEE Radar Conference (RadarConf)*, pp. 1–6, 2019.
- [80] F. Hau, F. Baumgärtner, and M. Vossiek, “Influence of vibrations on the signals of automotive integrated radar sensors,” in *2017 IEEE MTT-S International Conference on Microwaves for Intelligent Mobility (ICMIM)*, pp. 159–162, 2017.
- [81] J. Centers and J. Krolik, “Vibrational radar backscatter communications,” in *2021 55th Asilomar Conference on Signals, Systems, and Computers*, pp. 1086–1090, 2021.

- [82] J. Centers and J. Krolik, “Vibrational radar backscatter communication using resonant transponding surfaces,” in *2022 IEEE 12th Sensor Array and Multi-channel Signal Processing Workshop (SAM)*, pp. 71–75, 2022.
- [83] J. Centers and J. Krolik, “Multi-user methods for vibrational radar backscatter communications,” in *2023 IEEE International Conference on Acoustics, Speech and Signal Processing*, [ACCEPTED] 2023.
- [84] J. Centers, X. Tan, A. Hareedy, and R. Calderbank, “Power spectra of constrained codes with level-based signaling: Overcoming finite-length challenges,” *IEEE Transactions on Communications*, vol. 69, no. 8, pp. 4971–4986, 2021.
- [85] J. Centers and J. Krolik, “Vibrational radar backscatter communications theory and bound,” *IEEE Transactions on Radar Systems*, [PENDING REVIEW] 2023.

# Biography

Jessica Centers is originally from Evansville, Indiana, US. She earned her B.S. in Electrical Engineering from Milwaukee School of Engineering with a minor in German Studies in May 2018. Following her undergraduate career, Jessica began her graduate studies at Duke University in the Department of Electrical and Computer Engineering (ECE) working for Dr. Jeffrey Krolik. She earned her M.S. degree in ECE from Duke University in the summer of 2021, and defended this dissertation for her Ph.D. in the same department in the spring of 2023. While at Duke, Jessica was a 2021–2022 Bass Digital Education Fellow and spring 2022 Teaching with Purpose Fellow. In the summer of 2022, she taught a Duke Pre-College course to high school students called Applied Digital Signal Processing. Her current research interests include signal processing, communication systems, radar systems, physics-motivated machine learning, engineering education, and technology ethics and policy. She also expects to be completing an M.A. in Technology Ethics and Science Policy from Duke University in the summer of 2023. Following her graduate career, she will begin a full-time role at MITRE Corporation in McLean, Virginia as a Communications Engineer with their Communications, SIGINT, and PNT team.

In her graduate career, Jessica has been a first author on three conference papers [81–83], and two journal papers [84, 85].